ENERGY RESEARCH CENTER

LEHIGH UNIVERSITY

BETHLEHEM, PA

Cermet Composite Thermal Spray Coatings for Erosion and Corrosion Protection in Combustion Environments of Advanced Coal-Fired Boilers

Semiannual Technical Report Prepared for U.S. Department of Energy

Project Period: 1/14/97-8/14/97

by

B. S. Schorr, B. F. Levin, J.N. DuPont and A.R. Marder

August 31, 1997

Grant No. DE-FG22-95PC95211

Energy Research Center
117 ATLSS Drive
Lehigh University
Bethlehem, PA 18015

DOE Project Officer: Sean I. Plasynski
Administered by: Cynthia Y. Mitchell

Disclaimer

DISCLAIMER

Portions of this document may be illegible electronic image products. Images are produced from the best available original document.

EXECUTIVE SUMMARY

Research is presently being conducted to determine the optimum ceramic/metal combination in thermally sprayed metal matrix composite coatings for erosion and corrosion resistance in new coal-fired boilers. The research will be accomplished by producing model cermet composites using *powder metallurgy and electrodeposition methods* in which the effect of ceramic/metal combination for the erosion and corrosion resistance will be determined. These results will provide the basis for determining the optimum hard phase constituent size and volume percent in thermal spray coatings. Thermal spray coatings will be applied by our industrial sponsor and tested in our erosion and corrosion laboratories.

Bulk powder processed Ni-Al_2O_3 composites were produced at Idaho National Engineering Laboratory. The composite samples contained 0, 21, 27, 37, and 45 volume percent Al_2O_3 with an average particle size of 12 um. Also, to deposit model Ni-Al_2O_3 coatings, an electrodeposition technique was developed and *coatings* with various volume fractions (0-35%) of Al_2O_3 were produced. The powder and electrodeposition processing of Ni-Al_2O_3 composites provide the ability to produce two phase microstructure without changing the microstructure of the matrix material. Therefore, the effect of hard second phase particles size and volume fraction on erosion resistance could be analyzed.

To determine the effect of second phase particles on erosion resistance, powder processed and electrodeposited composites were tested in the erosion simulator (Al_2O_3 erodent, 40 m/s velocity, and 90^0 impact angle). It was found that electrodeposited Ni-Al_2O_3 composites containing small Al_2O_3 particles ($\approx$ 1um) showed better erosion resistance than powder processed Ni-Al_2O_3 composites containing large Al_2O_3 particles ($\approx$12 um). Also, an increase

in the volume fraction of Al_2O_3 particles in powder processed alloys led to a decrease in erosion resistance. For both powder processed and electrodeposited Ni-Al_2O_3 composites, addition of hard Al_2O_3 particles did not improve erosion resistance compared with pure nickel. The experimental procedure, results, and discussion of the erosion tests were presented in the previous progress reports.

During the last six months, the erosion resistance of thermal spray coatings with various volume fractions of the hard second phases were investigated. Because of the good reported corrosion properties, FeAl alloy-Al_2O_3 and FeCrAlY-Cr_2O_3 coating systems were chosen for erosion studies and hard phase content (Al_2O_3 and Cr_2O_3 particles) was systematically varied from 0 to 80 vol.%. High Velocity Oxygen Fuel (HVOF) and Vacuum Plasma Spray (VPS) processes were used for coatings deposition. It was found that erosion resistance of thermal spray coatings deceased with an increase in volume fraction of hard phase. These findings are in agreement with erosion results for electrodeposited and powder processed model Ni-Al_2O_3 alloys reported earlier in the program.

A possible critical level of approximately 50 vol.% oxide content and 5 vol.% of porosity that lead to substantially higher erosion rates was noticed for the FeAl plasma coatings. This result suggests a fundamental change in a dominant material removal mechanism. It was proposed that above 50 vol.% the oxide phase becomes interconnected and therefore, provides a network of brittle material that accelerates erosion damage. The experimental procedure, microstructural characterization, and erosion test results for thermal spray coatings are presented in this progress report.

I. Introduction

Solid particle erosion (SPE) has garnered a great deal of interest over the last 20 years due to the tremendous costs associated with repair of the damage it causes. It has been estimated that SPE costs the utility industry alone $150 million a year in reduced efficiency, lost power generation, and maintenance of damaged components (**1**). Over the years several methods have been implemented to try and prevent SPE with varying degrees of success. By far the most prevalent method of SPE prevention, is erosion resistant coatings; with cermets, metal matrix ceramic composites, gaining widespread industrial acceptance. Processing of cermet materials for SPE is often difficult due to large density and melting temperature differences between the ceramic and metallic constituents and the requirement that the coatings often need to be applied in the field. With their tremendous operating temperatures and particle velocities, thermal spray processes (e.g. plasma and high velocity oxy-fuel) have been able to overcome these challenges and provide superior erosion resistant coatings for a large number of industrial applications.

Although a great deal of research has been conducted in an attempt understand the erosion mechanisms of bulk metals, ceramics, and cermets in addition to thermal spray coatings, there is still much debate over the optimum microstructural composition needed to maximize erosion resistance. In the mid to late 80's, in an EPRI sponsored project, Wlodek discovered that a plasma coating comprised of 85% Cr_3C_2 and 15% FeCrAlY binder provided the best erosion resistance for steam turbine applications (**2,3**). Wlodek's coating was soon patented and became the mainstay of the thermal spray industry for SPE resistance. Erosion in steam turbine situations usually involves the high velocity low angle impingement of soft small particles (iron oxides) on turbine components. Recently it has become apparent that Wlodek's coating, although excellent under these specific conditions, is inadequate for general SPE prevention. Specifically the conditions that boiler tubes are subjected to in fossil fired plants are much different from steam turbines, consequently

Wlodek's optimized microstructure is not as effective in these situations. Further Scholl and Clayton found that no one coating performs best under all wear conditions (**4**), therefore coating selection must take environmental affects into account. Consequently the only way for efficient coating selection to occur is to have a basic understanding of the failure mechanisms present during erosion.

The objective of this research was to examine the erosion performance of several thermal spray coatings with specific regard to microstructure development for use in low NOx boiler applications. Plasma and HVOF processes were used to fabricate Fe/Al alloy-Al_2O_3 and FeCrAlY-Cr_3C_2 cermet coatings, where the hard second phase was varied from 0-80% (by volume) in the pre-sprayed powders. In addition several wrought alloys were also included as base line and reference materials. By thorough microstructural examination before and after testing, trends regarding hard phase editions and possible damage mechanisms for both coating systems and processes were determined.

II. Background

II.1. Thermal Spray

A schematic overview of the thermal spray process can be found in figure II.1 The basic premise behind thermal spray technology is to melt wire or particulate feed stock and accelerate the material towards a substrate upon where impact, the particles rapidly solidify to form a coating. As can be seen in figure II.2, thermal spray coatings typically contain splats (rapidly solidified molten particles), unmelted particles and porosity. The primary difference between the various thermal spray processes stems from the method they employ to generate the heat needed to melt the injected material. Among the more well established thermal spray techniques are plasma spray and HVOF, each of which was used in this study and will be discussed in further detail in the following sections.

II.1.1. Plasma Spray

A schematic of a typical plasma spray gun can be found in figure II.3, which consists of a tungsten cathode and water cooled copper anode. An inert gas, such as argon or helium, if feed between the anode and cathode where it is ionized, forming the high temperature plasma used to melt the feed material. Gas temperatures can exceed 15000K for a typical 40KW DC torch (**5**) with velocities in the 100-300 m/s range. The exact temperature of the plasma is controlled by the ionization potential of the gas being used. Once the particles impact the substrate surface they fan out forming splats, shown in figure II.2, and are rapidly quenched at rates approaching 10^6 °C/s (**5,6**). The further benefit of plasma spraying in a vacuum (VPS) eliminates any ambient oxygen that may react with the molten particles, providing cleaner denser coatings.

Due to the intense heat associated with plasma spraying and the exposure of the flame and substrate to oxygen (air), several reactions in the particles can occur during spraying. To illustrate some of the possible chemical changes occurring during spraying, a

proposed reaction for a NiCr - Cr_3C_2 cermet is listed below (**7**):

$$Cr_3C_2 + NiCr \;\; \text{--> } Cr_3C_2 + Cr_7C_3 + NiCr \; + NiO_2 + Cr_2O_3$$

Typically decarburization, leading to metal rich carbides, and oxidation are the principle reactions and can lead to drastic hardness reductions in the as-sprayed coatings. To compensate for the hardness loss, researchers have shown that the hardness of carbide coatings can be significantly increased upon post spraying heat treatment. The increase in hardness can be partially attributed to the elimination of several weaker carbides, Cr_7C_3 and $Cr_{23}C_6$,that are produced during spraying (**7,8,9**). Often heat treatment of the coatings is done in an ambient atmosphere (as shown above) causing oxygen to diffuse into the coatings forming oxides at the splat boundaries, which can also attribute to the increased hardness of the coatings (**10,11**). A proposed heat treatment reaction for the same NiCr - Cr_3C_2 cermet is shown below:

$$Cr_3C_2 + Cr_7C_3 + NiCr \; + NiO_2 + Cr_2O_3 \text{ ---> } Cr_3C_2 + NiCr \; + NiO_2 + Cr_2O_3$$

Additionally reduced porosity and lamellar structure changes, such as the precipitation of a fine Laves phase in a CoMoSi coating, can increase hardness as well (**12,13**). Although many researchers claim very specific reactions occur during spraying, as mentioned above, their is no definitive test methodology (i.e. x-ray diffraction is negated due to peak overlap) to verify the complex microstructure they claim to have observed. Consequently it is safe to assume both decarburization and oxidation are probably occurring, but any conclusions regarding the exact changes taking place is purely speculation.

II.1.2. High Velocity Oxy Fuel (HVOF) Spray

Figure II.4 contains a schematic of a HVOF gun. HVOF is a continuous

combustion process, where oxygen and fuel are mixed together and ignited under pressure in the combustion chamber to produce the tremendous temperatures and velocities associated with the process. After combustion the powder is injected into the high temperature gas and accelerated out the barrel of the gun. After exiting the gun barrel the molten or partially molten particles become entrained in a super sonic jet and eventually impact the substrate. Due to un-reacted oxygen in the combustion chamber, turbulent mixing of the jet and the surrounding atmosphere (figure II.5), and oxygen entrapment on the substrate surface, caused by boundary layer formation (figure II.6), complex particles reactions often occur during spraying. Similar reactions mentioned for plasma spraying can also occur with HVOF, forming various oxides and metal rich carbides.

Almost any volatile substance can be used as fuel in the HVOF process, though it is generally limited to propane, propylene, acetylene, hydrogen, and methane. The maximum temperature the flame can achieve is dependent upon the disassociation energy of the fuel gas, which is shown in figure II.7 for several typical HVOF gasses (**16**). The velocity of the gas in an HVOF system can routinely reach Mach 4 and beyond, i.e. 4 times the speed of sound or around 1200 m/s (**17**). The velocity of the particles is directly controlled by the combustion chamber pressure. The relationship between chamber pressure and velocity is illustrated in figure II.8, whereas the chamber pressure is increased the velocity increases at a parabolic rate. The increased particle velocities provide coatings with reduced porosity, higher cohesion, and increased compressive stresses (**5,17,18**).

II.2. Erosion

The basic concepts of erosion will first be discussed and related to ideal systems, such as pure bulk metals and ceramics. Eventually more complex real world materials, such as alloys and cermets, will be reviewed. Finally the erosion of thermal spray coatings, concentrating on plasma and HVOF, will be analyzed with regard to microstructure development and erosion testing conditions.

Erosion is generally defined as the gradual loss of material from a surface due to the impact of either a liquid or solid particle. The way in which the material is removed from the surface depends upon the size, shape, composition, density, velocity, and angle of impact of the eroding particle in addition to the composition, microstructure, and temperature of the eroded surface. Although the variables affecting erosion are numerous, researchers have found that the majority of damage mechanisms can be categorized as either ductile or brittle.

2.1. Ductile Erosion

Hutchings and Levy (**19**) found that most ductile materials exhibit similar erosive features, regardless of alloy composition. The erosion mechanism for ductile materials can be broken down into a three distinct phases. Initially it is found that the impacting particles plastically deform the surface, forming raised lipped craters or ripples (figure II.9a). Next additional particles impact the plastically deformed region further straining the area (figure II.9b & II.9.c). Finally the local plastic strain becomes critical thereby causing a portion of the surface to fracture (figure II.9.d). For an ideal material, ductile erosion is most prevalent when the impacting particles arrive at less than a 30° angle relative to the specimen surface (see figure II.10). At shallow impact angles the erodent particles are able to plough into the material creating long erosion trails, which increase the amount of plastic deformation per particle relative to the isolated seen at higher angles. A general expression for erosion rate versus velocity for most bulk materials is given by:

$$ER = K\,V^{n} \qquad (1)$$

where K is a constant and n is a material dependent variable (**21**). Typically velocity exponent values of n, for ductile materials, range from 2 to 4 (**22**). Many researchers link the variations in n values to the ability of the materials to absorb impact energy, which is

often manifest in toughness and strain hardening differences (**23**). Additionally some of the variations stem from testing differences (such as erodent and sample size) which will be further discussed in section II.2.5. Although some correlations have been found (i.e. toughness), there is still no complete predictive model for ductile erosion, and some of the observed phenomenon can still not be explained.

2.2. Brittle Erosion

Brittle materials typically have low fracture toughness and little ductility. Consequently these materials can not plastically deform to absorb the impact energy of the incident particles as do ductile materials (see previous section). Therefore erosion of brittle materials is found to occur primarily by chipping and cracking of the substrate material due to particle impact (**24**). Taylor and Murphy (**25**), further explained that radial cracks are formed perpendicular to the surface upon particle impact (loading) and spread laterally on rebounding (unloading), causing the heavy damage associated with erosion of brittle materials. Failure for brittle materials is maximized when the impacting particles arrive normal to the specimen surface (again see figure II.10), where the majority of the particles energy is transferred to the substrate. As noted above for ductile materials brittle velocity exponent values (n) for equation 1 generally fall in the 1.4 to 5.1 range (**25**). The wide range of n values for ceramic materials, as compared to ductile, stems from the large swing in both hardness, toughness, and testing techniques. Although not explicitly stated, ceramic or brittle materials appear very susceptible to erosion test conditions, consequently the large scatter in n values is most likely a direct result of non-uniform test methodologies. To compensate for various impact angles equation 1 can be modified by the sine of the impact angle for brittle materials to obtain (**21**):

$$ER = K\, V^{n} \sin\alpha$$

The reduction in transferred energy at lower impact angles (<90°) is represented by the sine function.

Additionally it is interesting to note that the reported n values for brittle and ductile materials overlap. It appears that for similar erosion conditions comparable erosion rates may be expected for both material types, even though entirely different material removal mechanisms are occurring. Recently Lindsley (**26**) found that plain carbon steels, when eroded in as quenched (martensite) and spheroidized conditions had identical n values, where it was observed that the quenched steel failed by chipping and cracking while the spheroidized steel exhibited large amounts of plastic deformation.

2.3. Cermet Erosion

Very few materials behave in either an ideal ductile or brittle manner when it pertains to erosion, making erosion analysis of even simple coatings difficult. But the complex microstructure present in cermet coatings makes the problem even more prevalent, with the presence of both ductile and brittle substances. Although the role of the ductile matrix and hard phase constituents in the prevention of erosion is unclear, the hard phase volume % (HPVP), size of the hard phase or mean free path, and chemical composition of the hard phase are general microstructure criteria that are important for cermet erosion resistance.

2.3.1 Hard Phase Volume Percent (HPVP)

Some research points to a large HPVP (>80%) to obtain optimal erosion resistance. As noted earlier, Wlodek (**2,3**) was one of the first to provide evidence that large HPVP provide superior erosion performance. Wlodek discovered that a 85% carbide-15%

FeCrAlY plasma sprayed cermet optimized erosion resistance for steam turbine applications (figure II.11). Wlodek went on to further state that the optimized erosion properties of the 85% carbide alloy stemmed from the breakdown of some of the carbides during spraying which provided small, well dispersed regions of chromium rich carbides which lead to precipitation strengthening. But, because Wlodek only tested for specific erosion conditions (steam turbines) and did not verify his final coating microstructures or second phase content, his results have been seriously questioned (**4**). Ninham and Levy (**27**) also reported that at around 80 volume % control of erosion in transferred from the binder to the carbide skeleton as shown in figure II.12. They concluded that the 80% level provides an interconnected three dimensional support structure preventing the grain by grain removal of carbides, which occurs with lower hard phase levels. Although Levy's results appear accurate, the overall conclusion that a large HPVP is beneficial is weak, since he did not systematically vary the hard phase content of his materials. Levy used several different matrices, reinforcement particles, and processing techniques to obtain a wide variety of cermets as can be seen in figure II.12. Consequently it is difficult to determine if the benefit of higher HPVP is caused by individual material properties, processing, or the interconnected hard phase network. Additionally an interconnected second phase network can be achieved at concentrations much lower than 80%, which again leads to questions regarding the accuracy of the conclusion that 80% hard phase provides optimum erosion resistance. Kosel and Aptekar (**28**) reported that for mild erosion conditions (35 m/s and 30μm crushed quartz) higher measured HPVPs resulted in lower overall erosion rates for Cu-WC cermets at both 30° and 90° impact as seen in figure II.13. Their conclusion regarding the benefit of higher HPVP is somewhat suspect due to their lack of data, they only tested four different materials with a very limited HPVP range (0-45%). Ramm and Clyne (**29**) found that at low impact angles (30°) increasing the HPVP also decreased the erosion rate for plasma aluminum-alumina composites as can be seen in figure II.14. Unlike Levy (**27**), Ramm and Clyne did systematically vary their cermet compositions,

while using one processing technique (plasma spray) however they failed to confirm the actual hard phase content of their as-sprayed coatings. Since it is well known that thermal spray processes can produce changes in both the chemical composition and volume percentage of the pre-sprayed powder, Ramm and Clyne's results could possibly have been attributed to some other microstructure feature beside the HPVP.

Other researchers claim a low HPVP, somewhere on the order of 40% or less, is needed to achieve optimum erosion resistance. Kosel and Aptekar (**28**) reported that the low toughness of most hard constituents resulted in a loss of erosion resistance as illustrated for Cu-Al_2O_3 and Cu-WC(W_2C) cermets shown in figure II.15. The Al_2O_3 reinforced alloys always performed worse as the HPVP was increased while the WC cermets seem to show a maximum erosion rate at about 15% hard phase when eroded with 180-300 μm crushed quartz at 90°. The ability of the cermets, specifically the reinforcement, to absorb impact was paramount for good erosion resistance which explained the poor performance of the brittle Al_2O_3 and the possible benefit of the tougher WC. Interestingly, comparison of Figure II.13 and II.15 seems to show the opposite trend with the only difference being mild versus aggressive erosion conditions (30μm and 35m/s versus 180-300μm and 108m/s), indicating the importance of erosion test conditions. Kosel and Aptekar's trends appear legitimate, but again the lack of tested samples (only tested 5-45% hard phase) limits the effectiveness of their conclusions. Referring to figure II.14 again, Ramm and Clyne (**29**) concluded that as the HPVP was increased the erosion rate went up for 90° impact with limited microstructure data. Tu et. al. (**30**) found that erosion resistance was optimized at 35% WC-65% NiCr as shown in figure II.16, due to the interplay of porosity and the hard WC particles. Again similar to Ramm and Clyne little work was done to verify the as-sprayed WC content of the tested coatings and no mention was made of the exact thermal spray process used to manufacture the coatings, making this study extremely suspect.

Much of the HPVP results are somewhat obscured by poor coating or material

characterization, which can often lead to misleading conclusions. Putting the absence of complete microstructural data aside, it appears that the use of both high and low HPVPs has a legitimate argument depending on the erosion conditions used. When mild erosion conditions are employed, such as those used by Wlodek (**2,3**) or Kosel and Aptekar (**28**), more hard reinforcements in the coating may be able to help deflect impact and prevent serious plastic deformation of the ductile matrix. On the other hand, harsher erosion conditions tend to crack the hard second phase particles and require fewer smaller particles to help toughen the ductile matrix to provide superior erosion performance. Consequently it appears that a change in erosion mechanism may be observed when the erosion conditions are varied, which helps explain the many advantages and disadvantages, of adding a hard second phase, that researchers have reported in the literature.

2.3.2. Size of Hard Phase (mean free path)

Additional work has showed that it is not the absolute HPVP that is important, but the binder mean free path (MFP) that controls erosion. Wayne and Sampath (**12**) found that differences in the erosion resistance of a 12% Co and 17% Co thermal sprayed WC-Co cermet could better be explained by differences in their respective MFPs then by HPVP alone. They proposed a predictive erosion model based on a combination of common mechanical properties, such as hardness(H) and fracture toughness (K_{IC}):

$$ER \; a \; (K_{IC}{}^{3/8} H^{1/2})(V_f^{Co}/1- V_f^{Co})$$

where V_f^{Co} is the volume fraction of cobalt. When they plotted the erosion resistance versus the above equation they found a fairly good correlation as shown in figure II.17, although the sintered 12% Co cermet could not be explained. Wayne and Sampath

speculated that the anomalous behavior of the 12% Co sintered sample was due to its smaller mean free path. Additionally, they determined that although the MFP is applicable to thermal spray coatings as well, cohesive strength and porosity of thermal spray coatings override this affect. But because Wayne and Sampath did not actually measure the MFP of any of the materials in their study nor verify the final microstructure content of their tested coatings , more work would be required to validate their conclusions.

The MFP relates not only the volume % of second phase but also the size of the reinforcement as well. Kosel and Aptekar (**28**) concluded that under conditions where the matrix will preferentially erode, leaving exposed second phase particles, an increased material removal rate occurs at the edges of large reinforcement particles due to enhanced micro-fracture of the poorly supported edges. Kosel and Aptekar's discussion was mainly qualitative, but their conclusion again reinforces the poor performance of the Cu-Al_2O_3 and Cu-WC alloys shown in figure II.8.15, which both contained large (>100μm) second phase particles that would be susceptible to this mechanism. Schmid (**31**) found similar results (larger particles are more prone to erosion damage) for 88% WC- 12% Co cermets with course, medium, and fine reinforcements as shown in figure II.18. Again larger reinforcement particles were found to crack at their edges, enhancing material removal. Finally, Lindsley (**26**) also found cracking of second phase particles to be more prevalent when larger carbides were eroded in spheroidized plain carbon steels. Lindsley discovered that 2.4μm Fe_3C carbides were often cracked after erosion while the 1.6μm and 0.8μm particles were not.

Anand and Conrad (**32**) defined both a brittle and ductile regime, depending on the the erodent particle-hard phase grain ratio (E/HP), shown schematically in figure II.19. When this ratio is large ductile failure was said to dominate and impact was absorbed by many particles. Anand and Conrad surmised that smaller reinforcement particles would resist cracking, resulting in a dominant erosion mechanism of plastic deformation of the ductile matrix with erosion rates that were roughly proportional to the square root of the

binder mean free path (figure II.20a). It was thought that the small particles tend to reduce the overall plastic deformation of the matrix by toughening the material. Conversely when the particle/hard phase ratio is small brittle failure (chipping and cracking) was observed. The larger reinforcement particles absorb all of the impact (figure II.8.5), and usually respond by chipping and cracking due to their brittle nature. In this regime the erosion rate was found to increase as the size of the hard phase was increased up to a point, after which damage leveled off (figure II.20b). A more recent study of spheroidized carbon steels conducted by Lindsley (**26**) also found erosion to be controlled directly by the MFP. Lindsley found that as the microstructural spacing (MS), the distance between carbides and or grain boundaries, was reduced so was the erosion rate of the tested material. In addition, a linear relationship between the erosion rate and $1/(MS)^{-1/2}$ was also found to persist as shown in figure II.21, again suggesting precipitation toughening. To lend credence to the smaller reinforcement particles toughening the overall structure, Liu et. al. (**33**) related the size of the second phase to the toughness values of WC-Co cermet materials, figure II.22. Liu concluded that by reducing the size of the WC particles the reinforcements could begin to impede dislocation motion, which lead to higher toughness values. Additional (**22,34**) studies also mention the size of the reinforcement as important for erosion control, where smaller more evenly distributed reinforcements enhance erosion resistance, though none of them extensively studied the effect and provide little data to back up their claims.

Research has shown that smaller particles lead to overall higher toughness values for cermet materials (**33**), in addition to reducing second phase cracking (**32,26**) and possibly deflecting impact (**32**). Consequently there is little doubt that small well distributed second phase particles are beneficial for improved erosion resistance. Also the MFP research reinforces the concept that toughness is a critical parameter for erosion performance to allow materials the ability to absorb impact energy prior to failure.

2.3.3. Chemical Composition of Hard Phase and Matrix

Careful selection of the metallic binder in conjunction with a particular reinforcement particle has been shown to provide enhanced erosion protection. Wang et. al. (**35**) found that NbCs work better with CoCr binders than either TiC, Cr_3C_2, or WC as shown in figure II.23. The higher ductility of NbC allows for more deformation to occur in the hard reinforcement, which is closer to that of the metallic binder. It is thought that the closer volume changes of the two constituents should allow the bond between the reinforcement and matrix to remain strong, helping to minimize particle pullout (**35**). The relatively small difference in ductility of the various carbides (less 20% difference) makes this conclusion somewhat dubious and the fact that no error is reported or mentioned may negate any observed differences.

The relative hardness of the erodent and reinforcement phase have also been reported to play an integral role in determining the dominant erosion mechanism. Kosel and Aptekar (**36**) tested various white cast irons and Stellite alloys with both alumina and crushed quartz particles whose erosion results are summarized in figure II.24. They stated that in cases where the erodent particles' hardness exceeded that of the hard phase, plastic deformation and lateral cracking resulted in increased erosion rates. Additional environmental factors, such as temperature and corrosion, also play an important role in determining the best material for a particular application and will be touched upon in section II.5 but is really beyond the scope of this paper.

The hardness and ductility of the matrix and reinforcement appear to be important criteria for material selection in erosion applications. Although Wang's results (**35**) are questionable, he brings up a valid point that may be more critical for reinforcement particles with low ductility (such as alumina). Meanwhile Kosel and Aptekar's results (**36**) are very important, and hint at the critical role environmental factors can have on materials' erosion resistance. If testing does not reflect actual application conditions, erroneous trends can lead to faulty conclusions and poor material performance.

2.4 Thermal Spray Coating Erosion

Thermal spray coatings are generated by melting powders and accelerating them towards a substrate where upon impact the particles build upon one another to form a coating. Coatings typically contain the following microstructural features: splats, unmelted particles, porosity, and cracks. Splats and unmelted particles comprise the majority of the coatings are considered discrete regions comprised of a single powder particle (**6**), that have been rapidly solidified and often contain dendritic and even amorphous structures (**6,13**). Rapid cooling, 10^6 C°/s (**5,6**), and oxidation of the powder during flight prevents diffusion during spraying (**37**), generally producing weak bonds between splats (**7,37,38,39**). It is the splat morphology that makes thermal spray coatings different from bulk materials and other coatings which typically contain a high degree of strong chemical bonding.

The unique structure of thermal spray coatings leads to three dominant failure mechanisms: splat debonding, splat fracture (porosity related), and splat deformation (**6,13,21**) which are schematically illustrated in figure II.25. Splat debonding is associated with failure at the splat interface and results in the removal of an entire splat. Whole spat delamination results in massive material removal, with little energy absorption, resulting in high erosion rates. Splat fracture stems from large plastic deformation induced in unsupported splats (splats over top of pores). Since their is no resistance to the impacting particle, unsupported splats will deform until the they contact another splat. This large deformation often exceeds the local strain limit of the material and causes the deformed portion of the splat to break off, resulting in moderate erosion rates. Finally splat deformation occurs if the previous two mechanisms are not operational, and is controlled by the ductile and brittle mechanisms mentioned earlier. Splat deformation is the most desirable of the three failure methods and leads to the lowest overall erosion rates.

Most researchers cite three additional factors, beyond what has been previously

been discussed in section II.2.3, that effect the erosion resistance of thermal spray coatings: porosity, cohesive strength, and residual stress (**12,21,35,40,41**). Porosity and the residual stress state in the final coating are fairly self explanatory, while the cohesive strength refers to the bonding between the individual splats or unmelted particles that comprise the final as-sprayed coating.

II.2.4.1 Porosity

It has been almost universally determined that porosity is not a desirable microstructural feature for optimal erosion resistance (**12,20,30,35,40,41**). Wang (**41**) discovered that for identical coatings, the higher porosity content coating eroded significantly faster at both 30° and 90°, figure II.26. Since Wang did not verify the hard phase content of the as-sprayed coatings he tested, his claim regarding higher porosity is not conclusive. Wayne and Sampath (**12**) found that porosity lowers the cohesion strength of thermal spray coatings, which leads to inter-granular cracking and eventual spallation as is illustrated in figure II.25 and further explained in figure II.27. Tu et. al. (**30**) concluded that larger pores more easily nucleate and propagate cracks causing increased erosion rates. Finally Kingswell et. al. (**21**) stated that low porosity enhances the ability of the coating to support itself and also removes potential crack sources. Additionally many studies have concluded that the superior erosion resistance of HVOF coatings stems from their low porosity levels in addition to high cohesive strength and residual compressive stresses (**35,40,41**). Except for Wang's (**41**) study, all of the other researchers base their conclusions on observed microstructural features and fracture theory, providing no concrete data to back up their hypotheses.

From the proposed mechanisms it can be seen that porosity may enhance both splat debonding and splat fracture leading to potentially very poor coating performance. At this time no study has been able to entirely separate the affects of porosity from other microstructure variables (such as HPVP) on the erosion resistance of thermal spray

coatings. Consequently it is impossible to definitively state that porosity is responsible for the increased erosion seen in many studies. Although no definitive statement can be made, enough evidence suggests that porosity may lead to higher erosion rates, that warrants exploring this issue further.

II.2.4.2. Cohesive Strength

Cohesive strength refers to the bonding present between the splats, unmelted particles, and retained carbides of a thermal spray coating. The bonding in thermal spray coatings has often been attributed to mechanical interlocking (**7,37,38,39**) due to the observation that greater surface roughness improves the adhesion of the coatings. Although mechanical bonding may be present in thermal spray coatings, it does not explain the great discrepancy of adhesion values reported for various spray processes, figure II.28. Consequently other bonding mechanisms must be involved as well, including physical and chemical (**42**). Physical bonds are based upon Van der Waals type interactions, where slight electrostatic charges induce opposite charges in neighboring atoms to form a relatively weak bond. Chemical bonds are based upon the classical sharing of electrons (i.e. ionic, covalent, or metallurgical) and need close proximity and the necessary activation energy to form. All of the above bonding mechanisms could and probably are present in thermal spray coatings, and as of this time it would be impossible to speculate further on which mechanisms are more prevalent without additional research.

All researchers agree that strong splat bonding is important for good erosion control. Failure at the splat interface, where cracks are thought to initiate (**41**), would allow the carbides or matrix to be pulled out in whole, greatly increasing the erosion damage. Figure II.10 shows splat debonding, which has been reported as a dominant erosion failure mechanism for thermal spray coatings by a number of researchers (**6,31,43,44**). As shown if figure II.29 Kim et. al (**6**) recently discovered that as the

cohesive strength of HVOF coatings was increased so was the resistance of the coating to SPE. Also the superior erosion resistance of high velocity coatings, such as HVOF and D-gun, is often attributed to the higher cohesive strength brought about by the tremendous kinetic energies associated with theses processes (**37,45,46**). All of the researchers mentioned above determined the cohesive strength of their coatings via tensile measurements. In order to hold the sample a grip must be affixed to the surface of the coating with epoxy. Due to penetration of the epoxy into the coating variable readings can be obtained. Consequently although Kim and the other researchers show nice trends, the method they employed to measure the cohesive strength of their coatings is notoriously unreliable and can yield misleading data.

Additionally some researchers feel that the increased erosion resistance reported from post heat treatment of thermal spray coatings may be due to inter diffusion of splats, which results in a stronger metallurgical bond instead of a mechanical one, thereby increasing the cohesive strength of the coating (**38,47**). Diffusion is unlikely since the driving force (chemical inhomogeneity) would be small and splats are often rimmed with oxides which would effectively block atom movement. Any benefit in erosion performance due to heat treatment, as is indicated in figure II.30, is most likely due to microstructural changes mentioned earlier in section II.1.

It is difficult to draw any specific conclusions regarding coating cohesion due to he poor test methodology that pervades most cohesion data currently available. Despite the lack of usable data, the importance of cohesive strength is not diminished, and strong particle bonding should always be paramount in any erosion resistant coating to prevent splat or particle debonding.

II.2.4.3. Residual Stress

Residual stresses in thermal spray coatings stem from thermal expansion mismatches between the coating and substrate and plastic deformation due to impact of

unmelted particles (**18,21**). Shrinkage of the splats will be restricted by the already solid substrate, resulting in the generation of residual tensile stresses. Residual tensile stresses tend to open cracks and thereby enhancing erosion rates. This type of stress state is dependent upon a large degree of melting of the injected powder and is therefore usually associated with plasma spraying. On the other hand if little melting occurs, and more solid particles impact the surface, residual compressive stresses due to plastic deformation are found (similar to shot peening). It was also found that the greater the velocity the larger the compressive stress, since more plastic deformation would occur (**18**). Residual compressive stresses tend to close cracks, which should help reduce crack propagation and hence material wastage (**21,47**). The majority of the residual stress research is qualitative and phenomonological in nature, with limited data to back up the above theories. Although not a great deal of hard data exists, the residual stress concepts are well reasoned and appear to fill in some critical gaps in the understanding of coating performance as it pertains to erosion.

II.2.5 Erosion Environment

Their is no standard erosion test procedure due to the wide range of industrial applications that researchers wish to simulate (**25**). Since it has already been mentioned here that no one coating performs best under all wear conditions, coating selection must take these environmental affects into account. Generally erodent type, test temperature, and ambient atmosphere all affect the performance of materials subjected to erosion conditions. Since many of these factors go beyond the scope of this study a brief review of these environmental variables will follow for the sake of completeness.

The size, shape, and type of erodent are primary variables that affect the erosion performance of various materials (**41**). Table II.I contains the hardness values, particle sizes, and erodent types of bed ash taken from 2 coal fired utility boilers. For boiler applications bed ash is sometimes used in testing, where it has been reported that the

majority of damage stems from the hard larger particles found in the ash (**8,32**), such as SiO_2 (**22,31,40,48,50**), mullite, and possibly Al_2O_3 (**13,26,32**). Again referring to the data found in Table II.I, it was reported that ash A was considerably more erosive than B (6.35 mm/year compared to 0.23 mm/year), due to the larger particles and higher concentration of hard elements found in that ash (**48**). Some evidence has also been reported that small particles can accumulate on the surface, forming a protective barrier that greatly reduces subsequent material loss (**51,52**). Kosel (**28**) found that in cases where the erodent particles hardness exceeded that of the hard phase, plastic deformation and lateral cracking (parallel to the surface) occurred, again resulting in poor erosion behavior. Kosel also found that erodents softer than the reinforcement could also lead to severe material loss if the impacting particles were large enough to induce elastic Hertzian cone fracture, usually associated with spherical particles (spherical particles usually have a much larger impact area). In addition Bahadur et. al. and Wang (**41,53**) reported angular particles tend to produce micro cutting mechanisms that enhance erosion. Consequently, as mentioned earlier, in more aggressive atmospheres (large,hard, angular erodent) lower hard phase concentrations performed better, as where less aggressive environments (soft, small, round particles) higher hard phase concentrations are superior (**6,10,28,44**). Therefore varying erosion conditions can lead to changes in erosion mechanisms which alter the relative benefit of second phase additions.

The chemical atmosphere under which coatings are subjected controls what type of corrosion products will form on the surface of a given coating, which in turn can have a dramatic affect on the erosion performance. Several studies have reported that oxidizing conditions produce scales that can both inhibit or greatly increase erosion damage, depending on the type impacting particle and scale properties (**22,40,43,48,50,52**). In addition certain particles can react with the coatings to form a scale, which can also lead to accelerated material removal, especially at elevated temperatures. K, Na, P, Cl, and S are all common elements found in ash that tend to react with most coatings forming various

scales (**40,50**). When scale forming mechanisms are in operation it has been proposed that the increased damage is caused by the ability of the hard impacting particles to disrupt and spall the scales. The scales eventually reform, and can easily be knocked off again, creating a damage cycle that greatly increases the rate at which material is lost (**48**).

III. Experimental Procedure

III.1. Coating Application

Improvement in the erosion properties of low NOx boiler coatings was the ultimate aim of this research. Since low NOx boilers contain harsh oxidation as well as severe sulfidation environments, careful selection of the coating systems was required to ensure both good erosion as well as corrosion performance of the selected coatings. The two coating systems chosen were Fe/Al alloy-Al_2O_3 and FeCrAlY-Cr_3C_2, the FeCrAlY system been reported to posses good erosion properties (**2,3**) while the Fe/Al alloy system was used as a model. In addition both of the systems have excellent reported corrosion properties (**2,3,54,55**). Table III.I contains the chemical compositions of the starting powders for each system while Table III.II. lists the mechanically blended cermet compositions sprayed for each thermal spray process.

The Fe/Al alloy-Al_2O_3 plasma sprayed coatings were applied by Ames National Laboratory using a Miller Thermal S-G 100 gun, while the Fe/Al alloy-Al_2O_3 HVOF coatings were fabricated by Hobart Taffa with a JP-5000 system. The vacuum plasma spray (VPS) coatings were sprayed in a vacuum chamber back filled with argon. Two sets of VPS and HVOF coatings were sprayed with different starting Fe/Al alloy powder sizes: <25μm (-25μm) and 25-45μm (+25μm). The HVOF FeCrAlY-Cr_3C_2 coatings were prepared by the Idaho National Engineering Lab (INEL) with a Jet Kote gun. Additionally several pure FeCrAlY coatings were sprayed to determine the affect of the in-flight oxidation on the erosion resistance of the as-sprayed coatings. It should be pointed out that INEL employs a closed loop feedback control system during spraying that enables them to accurately control both the in flight velocity as well as temperature of the spray particles. It is thought that this control system allows for greater reproducibility and hence superior coating quality.

Two bulk materials were also tested to provide a reference point for the collected

data. The first of these reference materials was a wrought FeAl alloy obtained from Oak Ridge National Lab (ORNL) to allow comparisons of bulk and sprayed materials of similar compositions. The last reference material was a typical boiler tube material, T-11 CrMo steel, which provided a direct comparison to current industry standards. The exact compositions of both the FeAl and CrMo steel can also be found in Table III.I.

Several of the VPS -25 μm Fe/Al alloy-Al_2O_3 and HVOF FeCrAlY-Cr_3C_2 coatings were heat treated after spraying to simulate the potential aging process they might see in service. The samples were encapsulated in argon to prevent oxidation and heated to 600°C for 96 hours in a tube furnace.

III.2. Coating Characterization

The objective of characterizing each coating was to identify qualitatively and quantitatively the microstructural constituents found in each coating and to uncover potential erosion damage mechanisms found during testing. To accomplish this the as-sprayed, heat treated, as well a post erosion samples were analyzed using light optical microscopy (LOM), scanning electron microscopy (SEM), image analysis, energy dispersive spectroscopy (EDS), wavelength dispersive spectroscopy (WDS), wet chemical analysis, and microhardness testing.

III.2.1. Metallography

All samples were prepared using well researched metallographic techniques to ensure true representations of all analyzed coatings (**56**). To minimize coating deformation and pullout, sectioning was done on a Buehler Isomet low speed saw with a diamond wafering blade. To prevent coating spallation and chipping, rotation of the diamond blade was always maintained perpendicular and directly into the coating's surface. The cut samples were mounted in Buehler cold setting epoxide in the configuration found in figure III.1. Both the hard filler powder material and back to back coating orientation shown in

figure III.1 were done to prevent edge rounding. Since erosion is a surface phenomenon the edge retention procedures were of critical importance when analyzing the post erosion samples.

The mounted samples were ground and polished using an Abrapol automatic polisher. The samples were arranged in a radial fashion in the Abrapol holder, as shown in figure III.2, to provide uniform grinding/polishing conditions along the entire length of each coating. The samples were ground flat using 120 grit SiC paper followed by 240, 320, 400, and 600 grit SiC for 30s on each step. Finally using a nylon cloth, the samples were then polished for 3 minutes using 1μm diamond paste, removed from the Abrapol mounting ring and placed in a LECO Vibromet vibratory polisher with a 400g load for 10 minutes on colloidal silica. The low nap polishing cloth and vibratory polisher were again used to help minimize edge rounding and pullout, thereby providing true specimen cross sections.

Several etchants were used to reveal the underlying microstructure and provide enhanced contrast for some of the coatings. The exact composition of each etchant and their specific use can be found in Table III.III. Marshal's etch with a drop of HF was used to reveal the Fe/Al alloy grains, splat boundaries, and splat structure; typical etchant times ranged from 3-5 minutes. Murakami's was used to stain the matrix of the FeCrAlY cermets to provide enhanced contrast for image analysis, and an electrolytic boiling picric solution to etch the FeCrAlY matrix. Times ranged from 2-4 minutes for the Murakami's etch to 30 seconds for the boiling picric etch. Finally a mixture of HCl and HNO_3 and was also used to attack the FeCrAlY matrix and reveal the underlying the splat structure; etchant times were around 30 seconds.

III.2.2. LOM, Image Analysis, and Hardness Testing

Microstructural observation and documentation were done with a Reichert-Jung

MeF3 metallograph. The Reikert microscope was used in both normal as well as Nomarski operational modes to provide the clearest pictures of the as sprayed and post eroded samples. Quantitative analysis of the phases present in the as-sprayed coatings was performed on a LECO 2001 image analysis system interfaced with a Nikon Photophot LOM. The various phases present in thermal spray coatings usually have different gray levels when viewed under a LOM, which can be used to separate them. The separation, or thresholding, process is illustrated in figure III.3 for an Fe/Al alloy plasma coating. Once thresholding was completed the pixels present in each phase could easily be counted by the computer and divided by the total pixels present in the field of interest to obtain the volume fraction of the phase in question. For the FeCrAlY-Cr_3C_2 coatings, etching prior to analysis was required to distinguish the metal and carbide phases which both appeared white under the LOM.

For splat size and mean free path measurements a Dansanto Micro-plan II digitizing pad was used. The specimen was first viewed under a Nikon LOM affixed with a video camera positioned over top of the digitizing pad. The light intensity of the LOM was adjusted to allow the microstructure and digitizing pad to be viewed simultaneously. A mouse was then used to trace various length segments of interest in the coatings' microstructures, which were downloaded to an IBM personal computer and calibrated to obtain actual microstructural data.

A LECO M-400FT microhardness tested with a knoop indenter was used to evaluate the hardness of several as-sprayed and heat treated samples. Figure III.4 shows a picture of a typical indentation in a HVOF sprayed FeAl coating. The knoop indenter was applied parallel to the coatings surface with a load of 300g to provide an indent that was orientated similar to that of the coating itself and much larger than any microstructural feature (splat or reinforcement particle).

III.2.3. SEM, EDS, and WDS

ETEC and JEOL 6300 SEMs were employed to image the surfaces of the various thermal spray coatings prior to and after erosion. The ETEC SEM uses an ordinary thermionic tungsten source and was used to image the un-eroded surfaces and screen some of the post erosion samples. For higher magnification work the JEOL 6300, which uses a field emission gun, was used with accelerating voltages ranging from 1 to 10KV to obtain better surface sensitivity. Additional imaging of the post eroded cross sections was also completed on the JEOL 6300.

Although X-ray diffraction is a technique that is often employed in the chemical analysis of thermal spray coatings, diffuse x-ray patterns and overlapping peaks limit the effectiveness of this technique (**25**). Consequently it was decided to use SEM X-ray methods which can analyze small regions of the sample and provide chemical data that can be easily related to the actual microstructure. Chemical analysis of the various phases present in the thermal spray coatings were determined by using the EDS capabilities of the ETEC and both WDS and EDS functions of a JEOL 733 super probe. The FeAl-Al_2O_3 coatings were analyzed on the ETEC, while the more complex structure of the FeCrAlY-Cr_3C_2 coatings required the use of the JEOL probe. The probe work was done at 15KV with 35nA to provide acceptable overvoltages and current for good signal to noise ratio for iron, chromium, carbon, oxygen, and aluminum. Analysis of the iron and chromium were done with LiF crystals (WDS), carbon and oxygen with LDE crystals (WDS), and the aluminum was detected using EDS.

III.2.4. Wet Chemical Analysis

Further chemistry data was obtained on select coatings using wet chemical analysis techniques. Several of the plasma sprayed FeAl coatings were removed from their substrates with liquid nitrogen and sent out for elemental analysis to get a quantitative measure of the elements present in each tested coating. The materials were dissolved in a

mixture of HCl and HNO_3 and analyzed with a mass spectrometer. The solutions were fairly clear indicating good dissolution, although it was reported that their was some residue possibly corresponding to undissolved Al_2O_3.

III.3. Erosion Testing

A schematic of the erosion tester used in this study can be found in figure III.5 An Ingersol Rand compressor generates the air flow which is then filtered and dried. The clean air is then regulated with a flow meter to achieve a desired velocity and heated via a series of fluid heaters for elevated temperature testing. Particles are then injected into the air stream and allowed to accelerate to their equilibrium velocity (acceleration tube), after which they impinge on the sample. The particles are separated from the air stream with a cyclone and re-sieved for later use. Particle velocity's are measured with a laser dopler velocometer and downloaded to an IBM personal computer for a full statistical analysis.

Table III.IV contains all of the pertinent erosion variables used in this study. Since boiler environments are fairly aggressive (**41**), 100% brown tabular alumina was chosen to provide accelerated weight loss. Although alumina is not commonly found in bed ash (**48**), several previous studies have used alumina and suggested that it best simulates the majority of erosion conditions (**57**). Additionally the toughness of brown alumina prevented a great deal of break up of the impacting particles and allowed the erodent to be reused (after sieving them again) . Large alumina (46 grit) particles were used to achieve a reasonable weight loss in a short period of time (20 minutes). The particles were further sieved to between -45 and +40 mesh (355-425μm) before testing to provide uniform erosion conditions and reproducible results. The velocity of 40 m/s was chosen to simulate an aggressive boiler water wall condition; water wall velocities are designed to be in the 10-20 m/s range although local velocities can get as high as 30-35 m/s (**48**). Room temperature testing was performed to minimize oxidation and allow accurate erosion data to be obtained without corrosion effects. Also room temperature testing allowed one sample

to be reused for each 20 minute test interval, thereby greatly reducing the time needed to test each sample. In addition several studies have reported that temperature only affects the absolute erosion rate of materials but relative rankings remain the same (**10,52**). Since a wide range of impact angles can be found in a coal fired boiler, both 30° (low angle) and 90° (high angle) impact angles were studied. Finally 3/8" square samples were used to ensure the velocity was as uniform as possible across the face of the tested samples and that the entire sample was within the particle stream. With the entire sample entrained in the air stream, particle rebound interactions could be minimized and more accurate erosion data could be generated.

The 3/8" samples were first weighed using a Metler College 150 balance, accurate down to 0.1 mg. The specimens were then placed in the erosion tester for 20 minute intervals, removed and weighed again. This procedure was repeated until the samples had been exposed for a minimum of 80 minutes. The cumulative weight loss after each interval was recorded and then plotted versus time, an example of several such curves can be found in figure III.6. Initial discontinuities in the weight loss versus time curve are often due to surface irregularities and/or embedded erosion particles, which lead to erroneous erosion rates if included in the final analysis. Consequently the slope of the weight loss versus time curve, where a linear relationship persists, was taken as the steady state erosion rate of the material. Linear regression software was used to calculate the slope of the weight loss curves and determine the steady state erosion rates for all of the materials tested.

IV. Results and Discussion

IV.1. Wrought Alloys

IV.1.1.Microstructure Characterization

Photomicrographs of the fully dense wrought FeAl and T-11 CrMo steel can be found in figures IV.1 and IV.2, respectively. The FeAl contains a rather large equiaxed grain structure with fine alumina precipitates oriented in the rolling direction. Additional randomly oriented precipitates can also be seen, but due to their small size have as yet not be identified. The CrMo steel has a much finer structure than the FeAl, and it is well known that it is ferritic. Fine chromium carbide precipitates (as indicated by the arrow) can be seen dispersed throughout the grain structure at higher magnifications. Both the FeAl and CrMo precipitates compositions have not been determined experimentally, with their identification being solely based upon previously reported results (**58,59**).

IV.1.2. Erosion

Erosion Rates- A sample weight loss versus time curve for the 2 standard materials can be found in figure IV.3, as stated before the linear slope of these curves represents the steady state erosion rate of the materials. The steady state erosion data for both materials tested was found to be 0.1543mg/min for the CrMo steel and 0.0725mg/min for the wrought FeAl alloy for both 90° and 30° impact. All four erosion rates have R coefficients of .998 or better, corresponding to excellent correlations for the linear regression analysis. Additionally figure IV.4 contains the weight loss versus time curves for the CrMo steel conducted on 3 separate days to verify the repeatability of the testing. From the slopes of the curves in figure IV.35 the erosion rates varied from .1432 to.1543, producing a potential error of 7%, therefore it was assumed that all of the erosion data is accurate to within ±7%.

The wrought alloys performed well from an erosion standpoint, outperforming

most of the tested coatings, at both impact angles. The FeAl material was about twice as erosion resistant as the CrMo steel which may have been related to the different mechanical properties of the two materials or possibly even the large grain size variation observed between the two alloys. The higher hardness of FeAl alloy may allow the material to deflect a greater percentage of the impacting particles energy which helps offset its comparable toughness. Consequently the FeAl, for the same number of impact events, will have less plastic deformation and hence less material removal. Additionally, with its larger grain size (around 100μm) the FeAl may have been able to plastically deform more and hence absorb more impact energy prior to failure than the smaller CrMo steel (grain size was about 10μm). Similar results were recently reported by Lindsley (**26**), where he found that large grain samples actually deviated from the previously mentioned (microstructural spacing)$^{-1/2}$ (figure II.21) relationship, and provided surprisingly low erosion rates. It should be mentioned that though large grained materials did perform better than some of the medium grained samples, overall the best erosion resistance was obtained with very fine microstructures. Lindsley postulated that the superior erosion resistance of the large grain materials may be due to the increased plastic deformation they can withstand. Since large grained materials have little resistance to plastic deformation (such as grain boundaries), the deformation layer will be pushed deeper into the sample allowing the impact energy to be dispersed over a lager area. Although the grain size definitely contributes to the erosion performance, Venugopai et.al. (**60**) found that changing material properties overwhelms most microstructural effects. Consequently the benefit of using FeAl most likely stems from its superior properties not the observed grain size difference.

Post Erosion Analysis- Both the CrMo and FeAl showed classic ductile erosion behavior with clear ripple formation present in both. Figure IV.5 contains the cross section for the FeAl sample after 90° impact. Ripple formation and ductile failure are associated with gouging, which work hardens the surface of the material. Eventually the material can not be strained any more and failure will ensue. For a more in depth review of ductile

failure see section II.2.1 and figure II.9. Additionally figure IV.6 shows ploughing at 30° impact for the CrMo sample. Ploughing is the other dominant ductile erosion mechanism which takes over at lower impact angles. With the observation of ripple formation and ploughing in both of the bulk materials, it is clear that ductile mechanisms are clearly controlling the erosion performance of these alloys.

IV.2. FeAl Alloy Coatings

IV.2.1. Microstructure Characterization

LOM- All six of the FeAl alloy air plasma (AP, 25-45μm) and vacuum plasma (VP, -25μm) coating microstructures can be found in figure IV.7 and IV.8 respectively. Only the -25 μm VPS coatings are shown since the 25-45 μm coatings are almost identical. From figures IV.7 and IV.8 it can be seen that all of the plasma spray coatings contain a splat type structure, formed from the impact of fully molten particles. All of the coatings contain FeAl alloy splats (light), oxide splats (dark gray), and porosity (black) in addition to some unmelted particles. The presence of 2 distinct darker phases, dark and light gray, in the AP coatings may indicate some oxidation of the FeAl alloy matrix or reduction of the Al_2O_3 reinforcement during spraying, which was not evident in the VPS coatings. Figure IV.9 shows an APS coating polished from the top down (planar view), with a distinctly different microstructure from that found in figures IV.7 and IV.8. The different appearance of the coating is due to the non-equiaxed splat structure as shown schematically in figure IV.10, which appears elongated in cross section but round from a planar view. Finally, as can be seen in figures IV.11 and IV.12, etching reveals the intersplat microstructure of the coatings. Figure IV.11 shows the columnar structure of the splats produced by the directional solidification found in thermal spraying (figure IV.10). A slightly higher magnification photomicrograph, found in figure IV.12, provides a clearer picture of the columnar splat structure. Due to the propensity of the FeAl alloy coatings to pit rather than etch, a better picture of the splat microstructure was unable to be obtained. Also in figure

IV.11 there is an unmelted particle that contains a dendritic structure, resulting from the gas atomization process commonly used in powder fabrication. Since the particle in figure IV.11 did not melt, no structure change would be expected and its prior strcture is maintained.

Figure IV.13 contains the cross section of a VPS coating heat treated at 600°C for 96 hours. From figure IV.13 no apparent change in the macrostructure or microstructure of the heat treated VPS coating was noticed from those found in figure IV.4.

Figure IV.14 contains the as-sprayed microstructure of the +25μm HVOF sprayed Fe/Al alloy coating. From figure IV.14 it is clear the the HVOF coatings are nearly 100% dense and contain little or no oxides. Etching of the Fe/Al alloy HVOF coatings, figure IV.15, shows that the both the +25μm and -25μm coatings are mainly comprised of unmelted particles. The lack of melting is typical of the JP-500 system, which uses extremely high velocities and minimal heat input to create fully dense, well adhered coatings (**14**). It also was evident that there was more splats with the -25μm particles, and consequently more melting was occurring, in addition to a finer overall structure. The higher degree of melting is expected, since the smaller particles require less heat input to become molten. Figure IV.16 contains the intersplat microstructure of the +25μm HVOF coating. The deformation present in the particles at the point of particle impact (see the arrow in figure IV.16) suggests the particles did not melt and the previous dendritic processing structure was maintained. Due to the low heat input and resultant lack of melting occurring in the HVOF process, it would be expected that the powder microstructure generated in the atomization process would be retained in the final coating.

Image Analysis- Figures IV.17-IV.18 contain the measured oxide, porosity and FeAl content of the VPS (+25 μm) coatings versus the starting Al_2O_3 content respectively. Figure IV.17 shows that the final oxide content of the coatings were in good agreement with the initial starting mechanical blend compositions (very close to the 1:1 trend line). Additionally from figure IV.18 it is evident that as the Al_2O_3 content in the initial powder is

increased the porosity level in the final as-sprayed coating also increases, which is in agreement with other reported thermal spray cermet research (**30**). It should be mentioned that only the apparent porosity was able to be measured, due to the inability to separate true pores from pullout induced during sample preparation. The apparent porosity provides a maximum porosity level for the coatings, and in reality the actual values could be at least half of the measured values. Although apparent porosity is not the absolute porosity level in the coating it does represent the general trends (i.e. more porosity will lead to higher apparent porosity) and is therefore satisfactory for coating to coating comparisons. Finally as more Al_2O_3 was included in the pre-sprayed powder less FeAl was found in the coatings as shown in figure IV.18, which makes sense since less FeAl was present in the pre-sprayed powder. Similar results were also found for the VPS (-25 μm) as well as the APS coatings, figures IV.19 and IV.20 respectively.

Since splat shapes tend to exhibit anisotropy, the oxide and porosity of the APS coatings was measured from both the cross and planar section (looking down from the top) to verify the previous results held for different orientations. From figures IV.21 and IV.22 it is apparent that their is good agreement between the 2 different views, therefore the use of cross sections as a true representation of the coating is an accurate assumption. Consequently all further analysis will only consider cross section results. The higher porosity level in the planar view of the 80% Al_2O_3 coating (figure IV.22) is most likely pullout, caused by the necessity to polish the top section samples by hand.

The matrix mean free path (MFP) data for the APS coatings in planar and cross section can be found in Table IV.I. The matrix MFP refers to the size of the FeAl alloy splats, and was measured from splat boundary to splat boundary or splat boundary to second phase boundary. Plasma coatings are dominated by the splat morphology which produces long, thin particles parallel to the coating interface (with a distinct aspect ratios as shown in figure IV.12) formed upon impact by the molten powder. Since a random orientation was taken in determining the splat size, the aspect ratio associated with splats

explains the smaller and more varied MFP data collected in cross section. The large error associated with the planar measurements stems from the large variation in starting powder size (20-45μm) and the complex splat shape formed upon impact of the molten particles with the rough topography of the substrate. Overall the data shows no definitive trends in either orientation as the amount of Al_2O_3 in the starting powders is increased. Since particle interaction during spraying is limited and the molten particles freeze almost instantaneously (10^6°C/s cooling rates, (**6**)) it would be difficult for the Al_2O_3 to modify the splat size in any way. Consequently the relative constant splat size observed for all of the coatings is not unexpected.

Chemical Analysis - From the LOM pictures of the Fe/Al alloy cross sections (figures IV.7 and IV.8) it is evident that 2 primary phases were present in the both the APS and VPS systems, with an additional minor phase appearing in the APS coatings. A backscatter (BSE) image of the 40% Al_2O_3-60% Fe/Al alloy APS sample, figure IV.23, verified the presence of 3 phases: white regions (1), dark gray areas (2), and small fields of light gray (3) . The EDS spectra for the white, dark gray, and light gray phases can be found in figures IV.24-IV.26, respectively. Phase 1, the white portions of figure IV.23, has a large iron K alpha peak and its accompanying K beta peak, indicating a substantial amount of iron is present. Additionally aluminum and chromium peaks were also found in phase 1. Taking into consideration the large concentration of iron, the presence of chromium and aluminum (the Cr was added to the pre-sprayed powder for improved ductility), and the light appearance of the phase 1 in BSE mode (indicating the presence of heavier elements) it is safe to identify this phase as the Fe/Al alloy. Phase 2, dark areas in figure IV.23, contains a large aluminum K alpha and smaller aluminum K beta peak corresponding to a high aluminum concentration. Although no oxygen was found (O is below the minimum detectability limit for the ETEC EDS system), the large aluminum peaks indicate phase 2 is Al_2O_3. Finally the light gray regions found in figure IV.23 have a similar EDS spectra to phase 1, although the aluminum peak is much less pronounced. The

smaller aluminum content coupled with the darker appearance of phase 3 may indicate partial vaporization of some of the aluminum during spraying and subsequent oxidation of the remaining elements. Further analysis would be required to ascertain the exact composition of phase 3, nonetheless the identity of phase 3 will be left as some Fe-Cr-Al oxygen containing compound. Again only phases 1 and 2 are present in the VPS coatings and appearance alone suggests that the phase identification done above holds for these coatings as well.

Wet chemical analysis of the VPS(-25), VPS(+25), and APS pure FeAl coatings was completed and the data can be found in Table IV.II. Both of the VPS coatings contain similar concentrations of aluminum, iron, and oxygen while the APS coating has substantially less aluminum and more oxygen. The reduction in aluminum and increase in oxygen substantiate the above EDS observations and lend credence to the initial identity proposed for phase 3. Also the higher nitrogen content of the APS coating may indicate nitride formation during the spraying process, but the absolute quantity of nitrogen is so small the nitride increase is negligible to the overall performance of the coating.

Microhardness- All of the microhardness data taken from the as-sprayed and heat treated FeAl alloy coatings can be found in Table IV.III. The hardness of the as-sprayed and heat treated samples was then plotted versus starting oxide content in figure IV.27 to determine the effect of heat treatment. From figure IV.27 it appears that the heat treatment provided a slight increase in the hardness of the FeAl plasma alloy coatings after being heated at 600°C for 96 hours, although the increase was well within the error of the measurements.

Figure IV.28 compares the hardness values of several pure FeAl alloy coatings and the wrought FeAl alloy. The HVOF coatings were substantially harder than VPS coatings due to their higher density for a similar splat size. It was also noted that the finer structure of the HVOF coatings provided harder readings than those obtained from the course grain wrought material. Similar to grains, the splat boundaries impede the movement of

dislocations, making it harder to plastically deform the material. In addition, the finer microstructure of the -25μm HVOF coating also explains the observed hardness difference in the +25μm and -25μm coatings.

IV.2.2. Erosion

Erosion Rates- The steady state erosion data for Fe/Al alloy coatings can be found in Table IV.IV for 90° impact and Table IV.V for 30°. All of the data recorded in Tables IV.IV-IV.V have R coefficients of .998 or better, corresponding to excellent correlations for the linear regression analysis. The erosion rate versus oxide, porosity and FeAl content for the as-sprayed APS coatings for 90° can be found in figures IV.29-IV.31, respectively. As the oxide content of the APS coatings was increased so was the erosion rate. Alumina is a brittle material that does not easily plastically deform upon impact, consequently chipping and cracking will be the dominant failure modes. Brittle failure mechanisms tend to produce accelerated erosion (at 90°), hence more alumina will increase the overall erosion rate of the coating. Also, since alumina will erode faster than the FeAl matrix, potential undercutting of the FeAl splats may occur, causing them to be pulled out in whole. In addition as the porosity of the APS coatings was increased, the erosion rate was also found to rise. Higher porosity levels provide crack initiation sites which usually propagate along splat boundaries again leading to whole splat removal and also weaken the internal support structure of the coating, thereby greatly increasing the erosion rate. Finally, higher FeAl contents tended to minimize erosion. FeAl is considerably more ductile than alumina and will therefore be able to absorb more impact before catastrophic failure, leading to lower erosion rates for the matrix.

Similar results were also found for both of the VPS coatings as shown in figures IV.32 and IV.33. It should be pointed out that the courser FeAl powder produced VPS coatings with slightly better erosion resistance than that of the APS and VPS (-25). Since failure of plasma coatings is most likely attributed to splat pullout, the larger splats present

in the VPS (+25) coatings may be more difficult to remove thereby reducing material removal. Large splats have more contact area per individual splat particle, consequently it would be expected that more energy would be required to break the bond between the splats to remove them. Also, courser splats would have less overall grain boundary area which would provide fewer sites for cracks to initiate. Although there does seem to be a slight benefit for using larger powder to improve the erosion resistance of as-sprayed plasma coatings, more work would be required to determine the importance of of this variable.

A discontinuity in the slope of the erosion rate versus both oxide content (40-50%) and porosity (4-8%) was also noted, figures IV.32 and IV.33. The slope change suggests a change in erosion mechanism, associated with either porosity or the hard second phase. Substantial density differences between the alumina, 3.968 g/cm^3 (**61**), and the Fe/Al alloy, 6.56 g/cm^3 (**55**), necessitated the calculation of volumetric erosion rates to ensure that the trends discussed above were legitimate. The volumetric erosion rates were calculated for all of the Fe/Al alloy plasma coatings and were plotted versus oxide content and porosity in figures IV.34 and IV.35 respectively. From both figure IV.34 and IV.35, it appears that the change in erosion mechanism noted before is even more evident now, occurring above 45% oxide content and greater than 10% porosity. From the ceramics literature, between 5-15% ,a switch between open (interconnected) and closed (isolated) porosity is observed (**62**). Consequently when the porosity level in the plasma coatings exceeds 5% it may become interconnected and lead to a substantially weaker structure that cannot withstand the harsh solid particle bombardment. Alternatively, greater than 45% oxide contents could provide an interconnected hard phase network. Since it would be expected that the brittle oxide would erode faster than the Fe/Al alloy matrix, undercutting and splat removal may become more evident when the structure is interconnected. Consequently the poor performance of the higher oxide coatings can not be definitively

attributed to either higher porosity or the higher brittle second phase content.

After heat treatment of the VPS -25μm coatings a slight increase in erosion resistance (or decrease in erosion rate) was noted as shown in figure IV.36. Although heat treatment appears to provide beneficial results, the improvement is rather minor and would require additional testing to confirm.

The 30° impact results for the APS coatings are summarized in figures IV.37 and IV.38. The same trend of increasing erosion rate was noted as both the porosity and alumina content were increased, with the same inflection on the oxide and porosity curves at around 45% oxide content and 5% porosity. Again the discontinuity suggests a change in erosion mechanism and would be expected to be similar to that discussed earlier. At first glance it appears that the 30° erosion rates are lower than those found at 90° corresponding to a milder erosion condition. But in order to accurately compare the 2 conditions the 30° data needs to be corrected to compensate for the reduced number of particles seen when the samples are inclined in the erosion stream. Since the erosion tester operates in a linear mass flow regime, corrections can easily be made by dividing the results by the sin(30°) as shown in figure IV.39. The corrected 30° data was then replotted versus oxide content for both angles and is shown in figure IV.40 (volumetric erosion rates were now plotted to compensate for density variations between the constituents). The 30° erosion rates were actually higher than those found at 90° for all samples except the two highest alumina content coatings (the second highest actually has the same erosion rate at both angles). The change in severity of erosion at low and high impact angles also serves as an indication of a change in the dominant damage mechanism attributed to either the increased porosity or brittle second phase.

The MFP data for all of the APS coatings at both impact angles is plotted versus erosion rate in figures IV.41 and IV.42. No trends between the MFP of the splats and erosion are evident. Wayne and Sampath found a similar result (**12**), where they stated that although the mean free path is an important coating parameter for controlling erosion,

porosity and intersplat strength can often override and negate this effect. Since it has already been found that their is significant porosity variations in these coatings and the possibility of poor splat cohesion, it is not unexpected that the MFP is inconsequential.

Table IV.1 contains the erosion rate data for the FeAl alloy HVOF sprayed coatings, which was plotted as a bar graph in figure IV.43. As shown in figure IV.43, the smaller starting powder provides superior erosion resistance. Although at first this may appear contradictory to the earlier reported VPS results where the larger starting powders performed better (figure IV.32), in the final analysis it is actually expected. Typically HVOF spraying provides coatings with higher cohesive strengths (**17**), therefore removal of the splats would not be as likely as in a plasma coating. Consequently the problem associated with small splat removal is not there and the benefit of the smaller splats on the toughness of the coating is observed. The finer microstructure resists plastic deformation by blocking the movement of dislocations, which leads to a tougher material. Additionally the smaller particles will tend to get hotter in the jet and reach higher velocities which will enable them to plastically deform more upon impact. Higher deformation creates a higher residual stress level in the as-sprayed coating (**18**). As discussed before higher residual stresses impede crack propagation, remducing a significant failure mechanism of thermal spray coatings (**47**).

Finally the hardness of the various FeAl materials processed by HVOF, VPS, and wrought versus their measured erosion rates can be found in figure IV.44. There is absolutely no correlation between SPE and the hardness of the various materials, which is in agreement with the work conducted by Levin (**58**) on weld overlay coatings. Clearly other factors (such as toughness, porosity, and cohesive strength), beside hardness dictate the performance of materials subject to SPE conditions.

Post Erosion Analysis- Several photomicrographs of as eroded plasma surfaces can be found in figure IV.45. In both pictures it appears that a portion of the coating is missing, the size and shape of the missing regions are similar to those expected for splats.

To confirm this observation the cross section of several of the plasma coatings clearly show FeAl splats debonding from one another, figure IV.46, cracking of the alumina second phase, figure IV.47, and subsequent undercutting of the FeAl spats, figure IV.48. The delamination or debonding of whole splats can be directly attributed to poor coating cohesion which lends credence to the previous theory explaining the superior performance of the courser VPS coatings. Splat removal appears to be a dominant damage mechanisms for plasma sprayed coatings and is enhanced by the brittle nature of alumina which allows undercutting of the FeAl matrix. Consequently the change in erosion rate mechanism for the plasma coatings at around 50% alumina is most likely attributed to the enhanced undercutting of the FeAl splats. Additionally, undercutting is most likely also enhanced by porosity (due to crack initiation), although there is no definitive proof to link the two.

When the pure FeAl HVOF coatings were examined no delamination was observed as can be seen in figure IV.49. This helps explain the higher erosion resistance of the HVOF coatings, since whole spat removal would not occur. Also comparing the eroded cross sections of the +25μm and -25μm coatings (figure IV.49a and b respectively), cracking is evident along the unmelted particles in the +25μm coatings where none can be seen in the -25μm. Consequently it is possible that eventually whole unmelted particles may be pulled out with the courser starting powder, owing to its higher erosion rate. The lack of cracking in the FeAl -25 coating could be associated with a higher residual stress level present in coatings made from finer powders, which suppresses crack formation.

IV.2.3. Summary

A possible critical point around 50% oxide content and 5% porosity lead to substantially higher erosion rates at both impact angles, and suggested a fundamental change in the dominant material removal mechanism. At the 50% oxide contents and above, it is possible that the oxide content becomes interconnected. Once the oxide begins to support itself, its brittle nature may dominate failure (chipping and cracking) leading to

undercutting of the FeAl alloy splats. In addition interconnected porosity, occurring above 5%, may also provide easy splat removal paths and could also explain the erosion damage mechanism change.

To a lesser extent the size of the microstructure also seemed to play an important role in the erosion resistance of the tested materials. For the plasma coatings, where cohesion poor due in part to oxide formation, splat delamination is prevalent and leads to poor erosion performance for finer starting powders. Conversely in HVOF coatings, where cohesion is much higher due in part to reduced oxide formation, splat or unmelted particle removal is not observed and the finer microstructure may actually toughen the material. Finally, the FeAl HVOF coatings offered superior erosion resistance to the plasma sprayed FeAl coatings. The lack of splat delamination, lower porosity, and fewer oxides in the HVOF coatings most likely attributed to their lower erosion rates.

IV.3. FeCrAlY Coatings

IV.3.1 Microstructural Characterization

LOM- Figure IV.51 contains a typical microstructure of a FeCrAlY coating. The coating in Figure IV.51 shows the unmelted half moons and high density associated with the HVOF process along with an apparent fine oxide structure interlaced between the particles. The oxides are formed during spraying due to the elevated temperature of the particles and the interaction of the supersonic jet with the ambient atmosphere (**9**). Although most of the FeCrAlY coatings looked similar to that found in figure IV.51, the abnormal spray conditions (i.e HVOF gun pressures of 99 psi), used during spraying of a few of the coatings also produced poor adhesion resulting in severe porosity in some of the samples (figure IV.52).

A typical FeCrAlY-Cr_3C_2 microstructure can be found in figure IV.53. The FeCrAlY-Cr_3C_2 cermet appears similar to the pure FeCrAlY coating shown in figure IV.51 with a great deal of unmelted particles and the same oxide structure. Because the FeCrAlY

matrix and carbides appear white in LOM, Murakami's etch was used to help reveal the entrained carbides. The final post etch structure can be seen in figure IV.54 where the FeCrAlY matrix is now light gray, the carbides are white, and the dark areas are most likely oxides. From figure IV.54 it is apparent that the entrained carbides are quite small (5-10μm) compared to the matrix (20-40μm) due to their smaller initial size and possible reduction during spraying.

The interior microstructure of the particles comprising the FeCrAlY-Cr_3C_2 coatings can be seen in figure IV.55. Since the majority of particles in the HVOF coatings are unmelted, the gas atomized dendritic structure left over from powder processing appears to be retained. To further reinforce the retention of the dendritic structure, the microstructure of the FeCrAlY powder used to produce the coatings was also examined. Figure IV.56 depicts the etched and mounted FeCrAlY powder and clearly shows a similar dendritic structure to that observed in the as-sprayed coating in figure IV.55. The deformation present at the impact site of the unmelted particles also suggests retention of the atomized microstructure. If the microstructure of the particle had been generated after impact no evidence of plastic deformation would be visible since the particle would have solidified from a liquid state. When solidifying, a structure would be expected to form parallel to the heat flow producing long columnar grains starting at the edges of the particle and extending toward the center, similar to that shown in figure IV.57 for a cast structure. But as figure IV.55 clearly indicates the grains show a more perpendicular orientation to the heat flow, which would be expected from flattening of preexisting dendrites on impact.

Image Analysis- Table IV.VI lists the porosity and oxide contents of the 100% FeCrAlY HVOF coatings sprayed with variable gun chamber pressures. The majority of the coatings were near 100% dense (<1% apparent porosity) with oxide contents ranging from 13-33%. Figures IV.58 and IV.59 plot the oxide and porosity content of the coatings versus the chamber pressure used to during spraying. There was no definitive trend for either oxide content or porosity with chamber pressure, and a more detailed study of the

spray parameters,which is beyond the scope of this study, would be required to make any further comments. Therefore chamber pressure alone cannot explain the differences between the microstructures in figures IV.51 and IV.52.

Figure IV.60 compares the carbide content in the starting powder compared to the final as-sprayed coating. As can be seen in figure IV.60 the actual carbide concentration of the as-sprayed coatings falls well below the 1:1 trend line, indicating poor spray efficiency of the carbides or decomposition of the carbides during spraying. Both decomposition and particle rebound have both been found to reduce the overall carbon content of HVOF sprayed carbide cermet coatings in the past (**7,9,37**). The remainder of the coating constituents were plotted versus the initial carbide content and can be found in figure IV.61. From figure IV.61 it is clear that as the initial carbide content in the pre-sprayed powder is raised so is the final as-sprayed carbide and oxide level. Therefore by adding the carbide and oxide content of the as-sprayed coatings together (hereafter referred to as the total hard phase content hereafter), and relating this to initial carbide content, compares favorable with the 1:1 correspondence line shown in figure IV.62. Consequently it would appear that decomposition of the carbides is occurring during flight and the dark phases which have been tentatively labeled as oxides may in fact be a complex combination of chromium rich carbides and various oxygen containing compounds.

Chemical Analysis- The EDS and WDS dot maps of aluminum, iron, chromium, carbon, and oxygen for an 80% Cr_3C_2- 20% FeCrAlY coating can be found in figure IV.63, where as the intensity in a map increases so does the concentration of the element in the coating. From figure IV.63 three distinct regions have been highlighted corresponding to the three major phases seen in the LOM: FeCrAlY matrix, carbides, and oxides. Region 1 contains high concentrations of both iron and aluminum and is free of oxygen and carbon, and has consequently been identified as the FeCrAlY matrix. Region 2 contains the highest concentration of carbon in addition to a high level of chromium, indicating the presence of a carbide phase. Region 3 contains all of the elements measured, and is a

complex mixture of chromium rich carbides (a and b) and several different oxides (c and d). Areas a and b contain materials of descending carbon concentrations with high levels of chromium, pertaining to chromium rich carbides. Area c appears to be some type of CrO, most likely formed from the total decarburization and subsequent oxidation of a carbide particle during spraying. While area d is a mix of predominantly iron and maybe even some aluminum and chromium oxides, stemming from the oxidation of the FeCrAlY matrix. For all subsequent analysis phase 3 will be referred to as an oxide, although it is actually a mixed region, since it would be difficult to separate the oxides and carbides in LOM analysis.

Microhardness- All of the microhardness data taken from the as-sprayed and heat treated samples can be found in Table IV.VII. The hardness of the as-sprayed and heat treated samples was then plotted versus starting hard phase content in figure IV.64 to determine the effect of the heat treatment. From figure IV.64 it appears that the heat treatment had little effect on the hardness of the coatings. The FeCrAlY coatings experienced a slight gain in hardness after being heated at 600°C for 96 hours, although the increase was well within the error of the measurements. Often the carbides formed during spraying are referred to as metastable since they will reform the higher carbon content carbides upon heat treatment (**9**). The higher carbon content carbides are harder, and consequently provide a substantial increase in the hardness of post heat treated coatings if they are formed. Since no hardness increase was noted, it is safe to assume that the loss of carbon is permanent and the resulting metal rich carbides are stable (at least at 600°C, which is the maximum operating temperature of most boilers).

IV.3.2. Erosion

Erosion Rates- The steady state erosion data for the FeCrAlY coatings can be found in Tables IV.VIII for 90° impact and IV.IX for 30°. All of the data recorded in Tables

IV.VIII-IV.IX have R coefficients of .998 or better, corresponding to excellent correlations for the linear regression analysis. The 90° erosion rates versus the various coating constituents for the pure FeCrAlY powders can be found in figures IV.65-IV.67. As the sprayed oxide content of the FeCrAlY coatings was varied no visible trend between the erosion rate was noticed (figure IV.65), although reducing the porosity (figure IV.66) or increasing the matrix content (figure IV.67) did seem to improve the erosion resistance of the coatings. In attempt to separate the effects of the porosity and oxide content, only the completely dense coatings (less then 1% porosity) were replotted versus oxide content in figure IV.68. Without porosity it is still difficult to confirm the presence of any trend and since the overall difference in erosion rates is small, it appears that the oxide content has no affect on erosion in these coatings. In addition it is also possible that the variable spray conditions used to fabricate the coatings could have caused other microstructural changes that may mask any observed trends, such as different degrees of melting which can drastically alter the coatings' structure.

Figures IV.69-IV.71 contain the erosion rates for the FeCrAlY-Cr_3C_2 coatings at 90° impact versus carbide, oxide, and matrix content, respectively. Increasing the oxide and carbide content increase the erosion rate of the coatings with a potential minimum at lower hard phase contents. Conversely increasing the matrix content improves the erosion rate with a potential minimum at higher matrix contents. Since both the retained carbides and oxides seem to play a similar role in the erosion resistance they were added together and plotted versus the erosion rate and volumetric erosion rate, figures IV.72 and IV.73 respectively, with a possible minimum in erosion rate again evident at lower hard phase concentrations. No difference between the erosion rate and volumetric erosion rate curves was noticed for the FeCrAlY coatings since the density of the various constituents were fairly close (consequently volumetric erosion rates will not be used for any of the FeCrAlY coatings). It is impossible to classify the minimum erosion rate, observed at about 25% hard phase, as a true minimum without additional testing. In addition when the fully dense

FeCrAlY data, discussed above, was added to the FeCrAlY-Cr_3C_2 results (figure IV.74) the erosion minimization conclusion becomes even weaker.

Although a minimum point cannot be identified, the data does present some interesting trends in regard to the continuous hard phase argument mentioned for the plasma FeAl alloy coatings. Again a discontinuity in the erosion rate is noticed at around 45% hard phase, and may be attributed to the formation of a continuous hard second phase network. The brittle second phase network may lead to enhanced material removal via particle delamination caused by undercutting (see earlier explanation for the FeAl alloy plasma coatings). Also, since all of the oxide levels for the 100% FeCrAlY coatings were below the critical hard phase threshold (roughly 45%), it makes sense that the erosion rates for the various coatings would be fairly constant. Consequently the lack of a trend for these coatings fits in well with the interconnected network concept.

The FeCrAlY-Cr_3C_2 30° erosion rate data versus hard phase content can be found in figure IV.75 and shows a similar trend to the 90° data discussed above, where a critical change in the erosion rate appears at about 45% hard phase. Again for 30°, the data had to be corrected for accurate comparison to the 90° results, which can be found in figure IV.76. Similar to the previously discussed FeAl plasma coatings their is a critical change (90° results are higher than the 30° results) in erosion mechanism from ductile to brittle at above 50 volume % hard phase. The change in severity of the impact angles again reinforces the change in erosion mechanism discussed above. Consequently an interconnected second phase network may seriously limit the ability of the material to absorb impact and drastically increase the erosion rate.

Post Erosion Analysis- The as eroded surfaces of the carbide cermets exhibited some cracking and potential carbide pullout which is shown in figure IV.77. The size of the damage event present in the FeCrAlY coatings is much smaller than that observed in the FeAl plasma coatings and appears much more angular in shape. The top picture in figure IV.77 also shows a crack that may represent the initial stages of carbide pullout, where the

carbide must first crack away from the surrounding matrix before it can be removed. Since it has already been shown that the carbides incorporated in the coating are small and angular in shape (unmelted), it makes sense that these damage regions correspond to carbide pullout. Also the fact that the carbides were almost always surrounded by weaker chromium rich carbides and oxides (figure IV.63), would allow them to be removed easier, lending more credence to the pullout argument. Finally splat delamination and cracking was also seen in the high carbide content FeCrAlY coatings, as shown in figures IV.78 and IV.79. Although it is difficult to see, the debonded and cracked areas are slightly darker, corresponding to lighter elements such as those found in the metastable carbides and oxides. Additionally since the the debonding was only seen in the higher hard phase content coatings this failure mechanism could only be associated with the presence of a large amount of mixed region. Therefore debonding, cracking and eventual pullout of the metastable carbides is also occurring in addition to pullout of the small retained carbide particles. Again both of these conclusions agree well with the observed increase in erosion rates found as the carbide and oxide contents rose and would be expected to be enhanced for a continuous hard second phase.

Although carbide pullout appears to be present (to a lesser extent), examination of the cross sections of the lower hard phase coatings revealed other erosion mechanisms at work in the FeCrAlY coatings as well. Figure IV.80 shows the cross section of a 40% Cr_3C_2-60% FeCrAlY coating, exhibiting inter splat damage. The bottom portion of the unmelted particle shows plastic deformation of the dendrites due impact during spraying, while the top portion, exposed during erosion, shows clear material loss. Closer examination of the top portion of the particle reveals no signs of plastic deformation and possible fracture along dendrite boundaries. Therefore the lower hard phase materials' improved erosion resistance is controlled by the partial removal of splats and unmelted particles which may be caused by dendrite spallation.

IV.3.3. Summary

Similar to the FeAl alloy plasma coatings a critical hard phase content was found to exist at about 50% and above for the FeCrAlY carbide HVOF coatings, where accelerated erosion (at both impact angles) was found to persist. The possibility of the second phase becoming interconnected above 50% and providing a network of brittle material, may explain the increased erosion . Carbide pullout, carbide cracking, and FeCrAlY dendrite delamination were observed in the HVOF sprayed FeCrAlY-carbide cermet coatings. Pullout and cracking are more prevalent at higher hard phase concentrations, while dendrite spallation is dominant at lower hard phase concentrations. The change from dendrite spallation to hard phase cracking and pullout, which could be enhanced by an interconnected hard phase network, may explain the higher erosion rates above the 50% threshold.

IV.4. Coating Rankings

The following section compares the erosion rates of all the coating systems and processes previously mentioned in an attempt to further contrast the failure mechanisms prevalent in each coating.

The erosion rate data for all coatings versus hard phase content can be found in figures IV.81 (90° data), IV.82 (30° data). Due to the different densities of several of the constituents of the coatings, volumetric erosion rates were used for more accurate comparisons. As can be seen the wrought materials performed very well at both angles, again relating back to their ductile failure mechanisms. The FeCrAlY-Cr_3C_2 and 0% hard phase FeAl alloy HVOF coatings (dark symbols) come closest to matching the erosion rates of the bulk materials. The lower hard phase concentrations in the FeCrAlY are actually better than the CrMo bulk material (figure IV.83). The benefits of HVOF coatings has been reported in the literature (**35,45**) and is attributed to the improved density and higher

cohesive strength of the coatings. It has already been shown that the HVOF coatings are considerably more dense, consequently excluding the porosity damage mechanisms. Although the cohesive strength of the various coatings has not been determined, the lack of splat delamination in the FeCrAlY HVOF coatings seems to indicate higher cohesion than observed for the FeAl plasma coatings where delamination was found.

V. Conclusions

From the study of several Fe/Al alloy and FeCrAlY cermet materials, sprayed with plasma and HVOF, the following can be concluded:

1a. The FeAl alloy plasma coatings tend to have a fully melted splat structure that yields columnar grains perpendicular to the substrate with some unmelted particles retaining the dendrite structure formed during the atomization process. The HVOF microstructures seemed primarily dendritic and were close to 100% dense. Good correlation between the starting Al_2O_3 contents and the final as-sprayed Al_2O_3 content for all of the plasma coatings was observed. Also as the Al_2O_3 content of the starting powders was increased the porosity level in the final plasma coatings was also found to rise.

1b. A possible critical point around 50% oxide content and 5% porosity lead to substantially higher erosion rates at both impact angles, and suggested a fundamental change in the dominant material removal mechanism for the FeAl coatings. At 50% oxide contents and above, it is possible that the oxide content becomes interconnected. Once the oxide begins to support itself, its brittle nature may dominate failure (chipping and cracking) leading to undercutting of the FeAl alloy splats. Since splat delamination, which was enhanced by oxide cracking and lead to FeAl undercutting (in the higher oxide coatings), was observed this theory seems plausible. In addition interconnected porosity, occurring above 5%, may also provide easy splat removal paths and could also explain the erosion damage mechanism change.

1c.To a lesser extent the size of the microstructure also seemed to play an important role in the erosion resistance of the tested FeAl alloys. For the plasma coatings, where cohesion is poor, splat delamination is prevalent due in part to oxide formation and leads to poor

erosion performance for finer starting powders. Conversely in HVOF coatings, where cohesion is much higher, splat or unmelted particle removal is not observed and the finer microstructure may actually toughen the material. Finally, the FeAl HVOF coatings offered superior erosion resistance to the plasma spray coatings. The higher cohesive strength, evidenced by the lack of splat delamination and lower porosity of the HVOF coatings, most likely attributed to their lower erosion rates.

2a.The FeCrAlY HVOF microstructures were primarily dendritic in nature due to the low heat content and resultant lack of melting associated with the HVOF process. The HVOF process produced coatings with little porosity. HVOF spraying resulted in the breakdown of the carbides into a complex mixture of metal rich carbides and various oxides.

2b. Similar to the FeAl alloy plasma coatings a critical hard phase content was found to exist at about 50% above which accelerated erosion (at both impact angles) was found to persist. The possibility of the second phase becoming interconnected above 50% and providing a network of brittle material, may explain the increased erosion . Carbide pullout, carbide cracking, and dendrite delamination are all possible mechanisms present in HVOF sprayed FeCrAlY cermet coatings. Pullout and cracking are more prevalent at higher hard phase concentrations, while dendrite spallation is dominant at lower hard phase concentrations. The change from dendrite spallation to hard phase cracking and pullout could be related to the continuity of the hard second phase.

VI. References

1. Solutions for Solid Particle Erosion; EPRI Journal; Oct/Nov 1990; pages 30-37.

2. Wlodek,S.T.; "Development and testing of plasma sprayed coatings for SPE resistance"; EPRI report CS4683; 1985.

3. Wlodek,S.T.; "Erosion resistant coatings for steam turbines"; EPRI report CS5415; 1987.

4. Scholl,M. & Clayton,P.; "Abrasive and Erosive Wear of Some Hypervelocity Air Plasma Sprayed Coatings"; National Thermal Spray Conference Proceedings; 1991; pages 39-52.54.

5. Herman,H. & Sampath S.; "Thermal Spray Coatings"; preliminary book; New York State University: Stony Brook.

6. Kim,H.J., Kweon, Y.G., Chang, R.W.; "Wear and Erosion Behavior of Plasma Sprayed WC-Co Coatings"; Journal of Thermal Spray Technology; June 1994, vol 3(2). pages 169-178.

7. Tiwari, R. and Herman, H,; "Development of Composite Microstructures by Thermal Spraying"; Thermal Spray Conference Proceedings; 1991; pages 375-380.

8. Linsey,J.R., Zheng, X., Bajan, R., & Slavin,T.P.; "Solid Particle Erosion Resistant Thermal Spray Coatings for Steam Turbine Applications"; Advances in Steam Turbine Technology for the Power Generation Industry (ASME); 1992; pages 137-144.

9. Sasaki,M., Fumio,K., Nakagawa,M., & Kudo,T.; "Study on Improvement of High Temperature Resistance of HVOF Cr_3C_2 Cermet Coatings"; International Conference on Processing Materials for Properties; 1993; pages 1093-1096.

10. Walsh,P.N.; "Erosion Resistance of Coatings at Steam Turbine Temperatures"; Steam Turbine-Generator Developments for the Power Generation Industry (ASME); 1992; pages 123-128.

11. Lewis,T., Sokol,L., & Hanna,E.; "Optimization of Gator-Gard Applied Chrome Carbide-MCrAlY Composite Overlays for Maximum Solid Particle Erosion Resistance"; Thermal Spray: Advances in Coatings Technology; 1987; pages 149-154.

12. Wayne, S.F. and Sampath, S.; "Structure/Property Relationships in Sintered and Thermally Sprayed WC-Co"; Journal of Thermal Spray Technology, Vol 1; December 1992; pages 307-315.

13. Guo,X.X. & Zhang, Hong; "HVOF-Sprayed Tribaloy (T-800): Microstructure and Particle Erosion Behavior"; International Thermal Spray Conference Proceedings; 1992; pages 729-734.

14. Thorpe, M.L.; JP-5000 HVOF manual; Hobart Taffa; 1992.

15. Hackett,C.M.& Settles,G.S.; "Turbulent mixing in HVOF thermal spray and oxidation"; Thermal Spray Conference Proceedings; 1994; pages 307-312.

16. Kraak, T. & Herlaar, W.; Influence of Different Gases on the Mechanical and Physical Properties on HVOF Sprayed Tungsten Carbide Cobalt; Thermal Spray Conference Proceedings; 1992; pages 153-158.

17. Irons,G.; "Higher velocity thermal spray processes produce better aircraft engine coatings"; SAE Technical Paper Series: paper# 920947; SAE; 1992.

18. Knight,R. & Smith,R.W.; "Residual Stress in Thermally Sprayed Coatings"; National Thermal Spray Conference Proceeding; 1993; pages 607-612.

19. Hutchings, I.M. & Levy, A.V.; Wear; 1989; pages 105-121.

20. Karimi, A. & Schmid,R.K.; "Ripple Formation in Solid-Liquid Erosion"; Wear, 156, 1992; pages 33-47.

21.Kingswell,R., Rickerby,D.S., Scott,K.T., & Bull,S.J.; "Comparison of Erosive Wear Behavior of Vacuum Plasma Sprayed and Bulk Alumina"; National Thermal Spray Conference Proceedings; May 1990; pages 179-185.

22.Wang,B.Q. & Luer,K.; "The Erosion-Oxidation Behavior of HVOF Cr_3C_2-NiCr Cermet coatings"; Wear, 174, 1994; pages 177-185.

23. Levy, A.V.; Solid particle erosion and erosion-corrosion of materials; ASM International; 1995, pages 35-54.

24. Hutchings, I.M.; Monograph on the Erosion of Materials by Solid Particle Impact; MTI Publication #10; 1983.

25. Taylor,M.L., Murphy, J.G., & King, H.W.; "Brittle/Ductile Erosion of Plasma Sprayed Ceramic and Metallic Coatings"; International Thermal Spray Conference Proceedings; 1988; pages 143-148.

26. Lindsley,B.; "Erosion of Spheroidized Fe-C Alloys"; unpublished Phd. dissertation: Lehigh University; 1996.

27. Ninham, A.J. & Levy A.V.; The Erosion of Carbide Metal Composites; Wear, vol. II; 1987; pages 825-831.

28. Kosel, T.H. & Aptekar S.S.; "Effect of Hard Second-Phase Particles on the Erosion Resistance of Model Alloys"; Corrosion '86; 1986; paper # 113.

29. Ramm, D.A.J. & Clyne, T.W.; The Effect of Metal Content on the Erosion Resistance

of Metal/Ceramic Co-Sprayed Composite Coatings Produced by VPS; Thermal Spray Conference Proceedings; 1994; pages 789-794.

30. Tu,J.P., Mao,Z.Y., & Wang,L.Z.; "Erosion Behavior of a Thermally Sprayed Ni-WC Coating at High Temperature"; National Thermal Spray Conference Proceeding; 1991; pages 53-57.

31. Schmid,R.K.; "Thermal Spray Cermet and Ceramic Coatings"; The South African Mechanical Engineer; June 1993. pages 171-174.

32. Anand, K. & Conrad, H.; Microstructure Effects in the Erosion of Cemented Carbides; Wear of Materials, vol. I; 1989; pages 135-142.

33.Liu,Y.X. & Zhang,S.H.; "Relationships between fracture toughness and microstructures of WC-Co Cemented carbide alloys"; Mechanical Behavior of Materials V, Vol 2; 1987; pages 1297-1303.

34. Lugscheider, E., Jokiel, P. & Remer, P.; Hard Particle Reinforced Aluminum Alloys for Aircraft Applications EWISCO; Thermal Spray Conference Proceedings; 1994; pages 79-83.

35.Wang,B.Q., Geng,G.Q., Levy,A.V., & Buchanan,E.R.; " Elevated Temperature Erosion of Carbide-Metal Composite Coatings"; International Thermal Spray Conference Proceedings; 1992; pages 735-742.

36. Aptekar,S.S. and Kosel,T.H.; "Erosion of white cast irons and Stellite"; Proceedings of the International Conference on Wear of Materials; ASME; 1985; pages 677-686.

37. Tucker Jr., R.C.; "Structure Property Relationships in deposits produced by Plasma Spray and Detonation Gun Techniques"; Journal of Vacuum Technology; July/August 1974; pages 725-734.

38. Lewis,C.; "Processing Makes the Difference in Thermal Spray Coatings"; Materials Engineering; August 1988; pages 45-48.

39. Kembaiyan,K.T. & Keshavan,K.; "Combating Severe Fluid Erosion and Corrosion of Drill Bits Using Thermal Spray Coatings"; Wear, 186-187, 1995; pages 487-492.

40. Wang,B.Q. & Luer,K.; "The Relative Erosion-Corrosion Resistance of Commercial Thermal Sprayed Coatings in a Simulated Circulating Fluidized Bed Combustor Environment"; National Thermal Spray Conference Proceedings; 1994; pages 115-120.

41. Wang,B.Q.; "The Elevated Temperature Erosion Behavior of HVOF Tungsten Carbide Cermet Coatings"; National Thermal Spray Conference Proceeding; 1995; pages 711-715.

42. Chandler, P.E.; "Improving the bonding of plasma sprayed coatings"; report from the Central Electricity Generating Board; May 1985.

43. Sue,J.A. & Tucker Jr., R.C.; "High Temperature Erosion Behavior Tungsten and Chromium Carbide Based Coatings"; Surface and Coatings Technology; 32, 1987; pages 237-248.

44. Wang, X., Popoola,O., & McCune,R.C.; "The Microstructure and Wear Mechanisms of Wire-Arc Sprayed Inconel 625 Coatings on 319 Aluminum"; National Thermal Spray Conference Proceeding; 1995, pages 633-638.

45.Vuoristo,P., Niemi,K., Makela,A., & Mantyla,T.; "Abrasion and Erosion Wear Resistance of Cr_3C_2-NiCr Coatings Prepared by Plasma, Detonation, and High Velocity Oxyfuel Spraying"; National Thermal Spray Conference Proceedings; 1994; pages 121-126.

46. Bianchi,L., Lucchese, P., Denoirjean,A., & Fauchais,P.; "Zirconia Splat Formation and Resulting Coating Properties"; National Thermal Spray Conference Proceeding; 1995; pages 261-266.

47. Irons, G., Kratochvil, W.R., Bullock, W.R., and Roy, A.; " Investigation of Erosion-Resistant Chromium Carbide Coatings Sprayed with the High Pressure HVOF Process"; Thermal Spray Conference Proceedings; 1994; pages 127-133.

48. Stringer,J.; "Practical Experience With Wastage at Elevated Temperatures in Coal Combustion Systems"; Wear, 186-187, 1995; pages 11-27.

49.Mottana,A., Crespi,R., & Liborio,G.; Guide to Understanding Rocks and Minerals; Simon and Schuster; 1977.

50.Wang, B.Q.; "Erosion-Corrosion of Coatings by Biomass-Fired Boiler Fly Ash"; Wear, 188, 1995; pages 40-48.

51.Sundararajan,G., Roy,M., and Venkatarman,B.; "Erosion Efficiency- a New Parameter to Characterize the Dominant Erosion Mechanism"; Wear, November, 1990; pages 369-381.

52. Wang,B.Q., Geng,G.Q., & Levy,A.V.; "Surface Behavior of Heat Exchanger Tubes in Fluidized-Bed Combustors"; Surface and Coatings Technology; 42, 1990; pages 253-274.

53.Bahadur,S. & Badruddin,R; "Erodent Particle Characterization and the Effect of Particle Size and Shape on Erosion"; Iowa State University, Department of Mechanical Engineering.

54.Reinshagen, J.H. and Sikka, V.K.; "Thermal Spraying of Selected Aluminides"; Thermal Spray Conference Proceedings; 1991; pages 307-313.

55. Sikka,V.K.; "Data package on Fe_3Al - and Fe-Al based alloys developed an ORNL"; unpublished report; January 1993.

56. Blann,G.A., Diaz,D.J., & Nelson,J.A.; "Raising the Standards for Coating Analysis"; Advanced Materials and Processes; 12, 1989; pages 31-36.

57. Walsh,P.N., Quets, J.M., & Tucker Jr.,R.C.; "The Effects of Erodent Particle Size and Composition on the Erosion of Chromium Carbide Based Coatings"; Advances in Steam Turbine Technology for the Power Generation Industry (ASME); 1994; pages 261-265.

58. Levin,B.; "Erosion of Weld Overlay Coatings"; unpublished Masters thesis: Lehigh University; 1994.

59. Bardes,B.P.; Metal's Handbook 9th Edition, V1: Properties and Selection:Irons and Steels; ASM; 1978.

60. Venugopai,R. & Sundarajan,S.; "The Influence of Grain Size on the Erosion Rate of Metals"; Metallurgical Transactions A; 18A, June 1997; pages 1043-1052.

61. Lide,D.R.; "Handbook of Chemistry and Physics"; CRC Press; 1990.

62. Richerson,D.W.; Modern Ceramic Engineering; Marcel Decker, Inc.; 1992.

Table II.I- Major ash constituents for 2 coal fired utility boilers (**48**)

Constituent	Hardness (Moh)	Boiler A(%)	Boiler B (%)
SiO_2 (quartz)[1]	7	2	48
Al_2O_3[1]	9	24	28
Fe_2O_3	6	6	16
CaO	N/A	3	1.7
MgO	5	0.8	0.7
Na_2O	N/A	1.4	0.3
K_2O	N/A	1.0	2.2

[1]The majority of Al_2O_3 and a good portion of the SiO_2 are tied up in Mullite ($2\ SiO_2 + 3Al_2O_3$) which has a hardness of 7.5. All hardness data was taken from reference **49**.

Ash size (um)	Boiler A(%)	Boiler B(%)
> 930	11.9	0.4
300 - 930	3.7	0.9
173 - 300	9.2	5.0
66 - 173	25.9	14.2
30 - 66	14.9	11.9
< 30	34.4	67.6

Table III.I- Chemical compositions of starting powders and bulk alloys used in this study (all values listed are weight %).

Material	Aluminum	Carbon	Chromium	Iron	Yttrium	Molybdenum	Oxygen
FeCrAlY powder	6.5	---	28.50	BAL	0.65	---	---
Cr_3C_2 powder	---	12.75	86.00	---	---	---	---
FeAl powder	16.76	0.028	2.25	BAL	---	---	0.068
Al_2O_3 Powder	53	---	---	---	---	---	47
Wrought FeAl	35.8	0.13	---	BAL	---	0.2	---
CrMo Steel (T-11)	---	<0.17	1.15	BAL	---	0.5	---

Table III.II- Mechanical blends for each coating system and process (all values are in volume %).

Cr_3C_2/FeCrAlY (HVOF)	Al_2O_3/FeAl (APS) 25-45μm	Al_2O_3/FeAl (VPS) 25-45μm	Al_2O_3/FeAl (VPS) <25μm	Al_2O_3/FeAl (HVOF) 25-45μm	Al_2O_3/FeAl (HVOF) <25μm
0 / 100	0 / 100	0 / 100	0 / 100	0 / 100	0 / 100
10 / 90	10 / 90	10 / 90	10 / 90	-----	-----
20 / 80	20 / 80	20 / 80	20 / 80	-----	-----
40 /60	40 /60	40 /60	40 /60	40 /60	-----
60 / 40	60 / 40	60 / 40	60 / 40	-----	-----
80 / 20	80 / 20	80 / 20	80 / 20	-----	-----

Table III.III- Compositions and usage of etchants

Etchant	Composition	Use	Time
Murakami's	5g $K_3Fe(CN)_6$, 7g NaOH, & 100ml H_20	stain FeCrAlY matrix	2 min
Boiling Picric (electrolytic)	5g picric, 2ml HCl, & 100ml H_2O	etch FeCrAlY alloy	30 sec
Marshal's	8g Oxalic acid, 5ml H_2SO_4, 100ml H_20, & 100ml H_2O_2	etch Fe/Al alloy	3 min
HCl-HNO_3 mixture	12ml HNO_3, 20ml HCl, 20ml H_20, & 40ml H_2O_2	etch FeCrAlY and Fe/Al alloy	10 sec

Table III.IV- Erosion test conditions

Parameter	Setting
Sample Size	3/8"(l) x 3/8"(w)
Erodent	Brown Tabular Alumina
Erodent Size	355-425 μm
Velocity	40 m/s
Feed Rate	90 g/min
Temperature	Room Temperature (26° C)
Angle	30° & 90°
Time	20, 40, 60, and 80 minutes

Table IV.I- Matrix splat mean free path (MFP) data for planar and cross section orientations of APS coatings (each value is based on 100 individual microstructure measurements).

Coating Composition (Powder)	MFP-Top (μm)	MFP-Side (μm)
100% FeAl	19.17 ± 14.13	14.92 ± 21.80
10% Al_2O_3-90% FeAl	19.26 ± 12.28	8.354 ± 6.074
20% Al_2O_3-80% FeAl	15.85 ± 10.95	8.674 ± 8.01
40% Al_2O_3-60% FeAl	19.95 ± 10.89	13.35 ± 13.12
60% Al_2O_3-40% FeAl	15.79 ± 7.90	12.99 ± 13.77
80% Al_2O_3-20% FeAl	17.00 ± 9.90	10.42 ± 13.10

Table IV.II- Wet chemical analysis data for FeAl alloy plasma coatings (all values are in weight %).

Coating	Process	Al (%)	Fe (%)	O (%)	N (%)
100% FeAl (-25)	VPS	14.7	83.1	0.220	0.0016
100% FeAl (+25)	VPS	15.8	82.6	0.228	0.00149
100% FeAl	APS	11.3	83.9	2.83	0.00960

Table IV.III- Knoop micro hardness data for the FeAl wrought alloy and FeAl alloy coatings (hardness data for the post heat treated samples is also included).

Material	Process	Heat Treatment	Knoop Hardness
FeAl	Wrought	None	259 ± 8
0% Al_2O_3- 100% FeAl	VPS	None	282 ± 29
20% Al_2O_3- 80% FeAl	VPS	None	293 ± 25
60% Al_2O_3- 40% FeAl	VPS	None	393 ± 58
0% Al_2O_3- 100% FeAl	VPS	600°C for 96 hours	282 ± 12
20% Al_2O_3- 80% FeAl	VPS	600°C for 96 hours	323 ± 53
60% Al_2O_3- 40% FeAl	VPS	600°C for 96 hours	423 ± 76
100% FeAl (+25)	HVOF	None	427 ± 18
100% FeAl (-25)	HVOF	None	497 ± 36

Table IV.IV- Erosion rate data for both reference materials and all FeAl alloy coatings, at 90°.

Material	Process	Heat Treatment	Erosion Rate (mg/min)
CrMo Steel (T-11)	**Rolled**	**None**	**0.1543**
FeAl	**Wrought**	**None**	**0.0725**
0% Al_2O_3-100% FeAl	APS	None	0.2585
10% Al_2O_3-90% FeAl	APS	None	0.4185
20% Al_2O_3-80% FeAl	APS	None	0.5125
40% Al_2O_3-60% FeAl	APS	None	0.4865
6% Al_2O_3-40% FeAl	APS	None	0.9875
80% Al_2O_3-20% FeAl	APS	None	1.5600
100% FeAl (-25)	VPS	None	0.3550
10% Al_2O_3-90% FeAl (-25)	VPS	None	0.3955
20% Al_2O_3-80% FeAl (-25)	VPS	None	0.4275
40% Al_2O_3-60% FeAl (-25)	VPS	None	0.5105
60% Al_2O_3-40% FeAl (-25)	VPS	None	0.7785
80% Al_2O_3-20% FeAl (-25)	VPS	None	1.5900
100% FeAl (+25)	VPS	None	0.2255
40% Al_2O_3-60% FeAl (+25)	VPS	None	0.4035
80% Al_2O_3-20% FeAl (+25)	VPS	None	1.5150
100% FeAl	VPS	600°C for 96 hours	0.1660
20% Al_2O_3-80% FeAl	VPS	600°C for 96 hours	0.2345
60% Al_2O_3-40% FeAl	VPS	600°C for 96 hours	0.6159
100% FeAl (+25)	HVOF	None	0.2075
100% FeAl (-25)	HVOF	None	0.1315

Table IV.V- Erosion rate data for both reference materials and tested FeAl alloy APS coatings, at 30°.

Material	Process	Erosion Rate (mg/min)
CrMo Steel (T-11)	**Rolled**	**0.1543**
FeAl	**Wrought**	**0.0725**
0% Al_2O_3-100% FeAl	APS	0.2555
10% Al_2O_3-90% FeAl	APS	0.3250
20% Al_2O_3-80% FeAl	APS	0.3220
40% Al_2O_3-60% FeAl	APS	0.2710
6% Al_2O_3-40% FeAl	APS	0.4927
80% Al_2O_3-20% FeAl	APS	0.6950

Table IV.VI- As-sprayed 100% FeCrAlY coating compositions.

Chamber Pressure (psi)	Porosity (Vol %)	Oxide (Vol %)	FeCrAlY (Vol %)
45	0.89 ± 0.68	13.00 ± 1.64	85.90 ± 2.10
45	3.46 ± 0.61	24.59 ± 2.78	71.15 ± 2.53
78	1.08 ± 0.95	32.94 ± 5.44	65.97 ± 5.87
78	0.3 ± 0.15	29.75 ± 1.92	70.04 ±4.59
99	0.68 ± 0.48	22.87 ± 3.27	76.45 ± 3.30
99	0.08 ± 0.02	20.56 ± 1.80	77.28 ± 1.14
48	0.09 ± 0.05	14.98 ± 0.99	84.90 ± 2.53
78	1.71 ± 1.28	27.15 ± 1.92	69.82 ± 1.84
75	4.62 ± 2.31	16.13 ± 1.45	78.59 ± 3.13

Table IV.VII- Knoop micro hardness data for the FeCrAlY-Cr_3C_2 HVOF cermets before and after heat treatment.

Material	Process	Heat Treatment	Knoop Hardness
10% Cr_3C_2- 90% FeCrAlY	HVOF	None	466 ± 30
40% Cr_3C_2- 60% FeCrAlY	HVOF	None	423 ± 69
80% Cr_3C_2- 20% FeCrAlY	HVOF	None	672 ± 63
10% Cr_3C_2- 90% FeCrAlY	HVOF	600°C for 96 hours	418 ± 37
40% Cr_3C_2- 60% FeCrAlY	HVOF	600°C for 96 hours	521 ± 50
80% Cr_3C_2- 20% FeCrAlY	HVOF	600°C for 96 hours	707 ± 123

Table IV.VIII- Erosion rate data for both reference materials and all FeCrAlY HVOF coatings, at 90°.

Material	Process	Chamber Pressure (psi)	Erosion Rate (mg/min)
CrMo Steel (T-11)	**Rolled**	**-----**	**0.1543**
FeAl	**Wrought**	**-----**	**0.0725**
100% FeCrAlY	HVOF	45	0.1820
100% FeCrAlY	HVOF	45	0.1530
100% FeCrAlY	HVOF	78	0.1699
100% FeCrAlY	HVOF	78	0.1250
100% FeCrAlY	HVOF	99	0.1564
100% FeCrAlY	HVOF	99	0.1267
100% FeCrAlY	HVOF	48	0.1012
100% FeCrAlY	HVOF	78	0.1395
100% FeCrAlY	HVOF	75	0.2867
100% FeCrAlY	HVOF	78	0.1199
10% Cr_3C_2-90% FeCrAlY	HVOF	78	0.1043
20% Cr_3C_2-80% FeCrAlY	HVOF	78	0.1101
40% Cr_3C_2-60% FeCrAlY	HVOF	78	0.1248
60% Cr_3C_2-40% FeCrAlY	HVOF	78	0.1520
80% Cr_3C_2-20% FeCrAlY	HVOF	78	0.3190

Table IV.IX- Erosion rate data for both reference materials and FeCrAlY-Cr_3C_2 HVOF coatings, at 30°.

Material	Process	Erosion Rate (mg/min)
CrMo Steel (T-11)	**Rolled**	**0.1543**
FeAl	**Wrought**	**0.0725**
100% FeCrAlY	HVOF	0.0950
10% Cr_3C_2-90% FeCrAlY	HVOF	0.0955
20% Cr_3C_2-80% FeCrAlY	HVOF	0.0930
40% Cr_3C_2-60% FeCrAlY	HVOF	0.1005
60% Cr_3C_2-40% FeCrAlY	HVOF	0.1145
80% Cr_3C_2-20% FeCrAlY	HVOF	0.1490

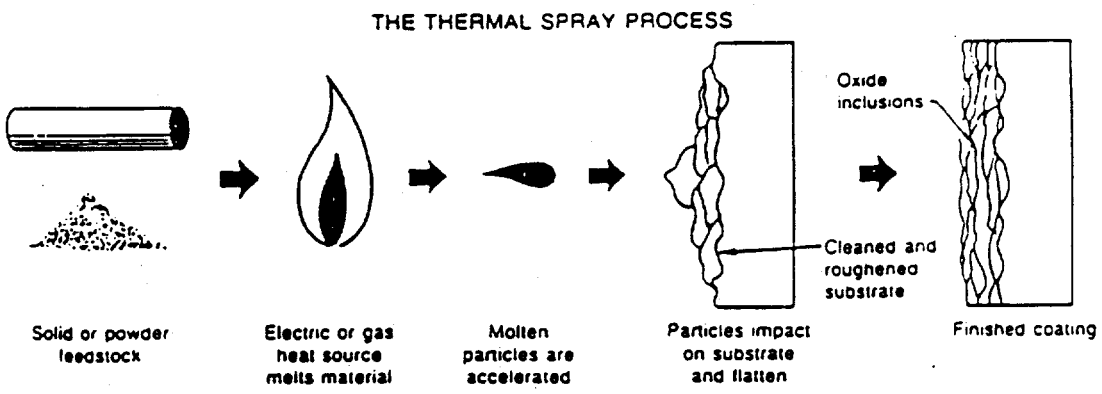

Figure II.1- Thermal spray process schematic (5).

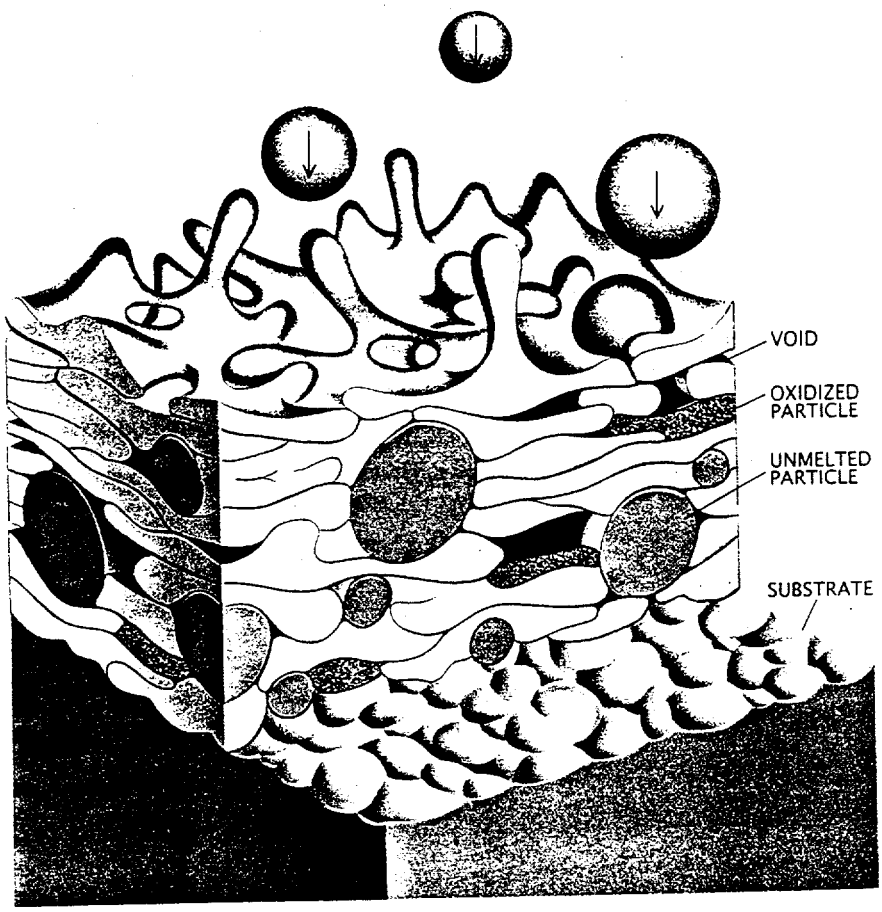

Figure II.2- Illustration of the deposit build-up process in a thermal spray coating (5).

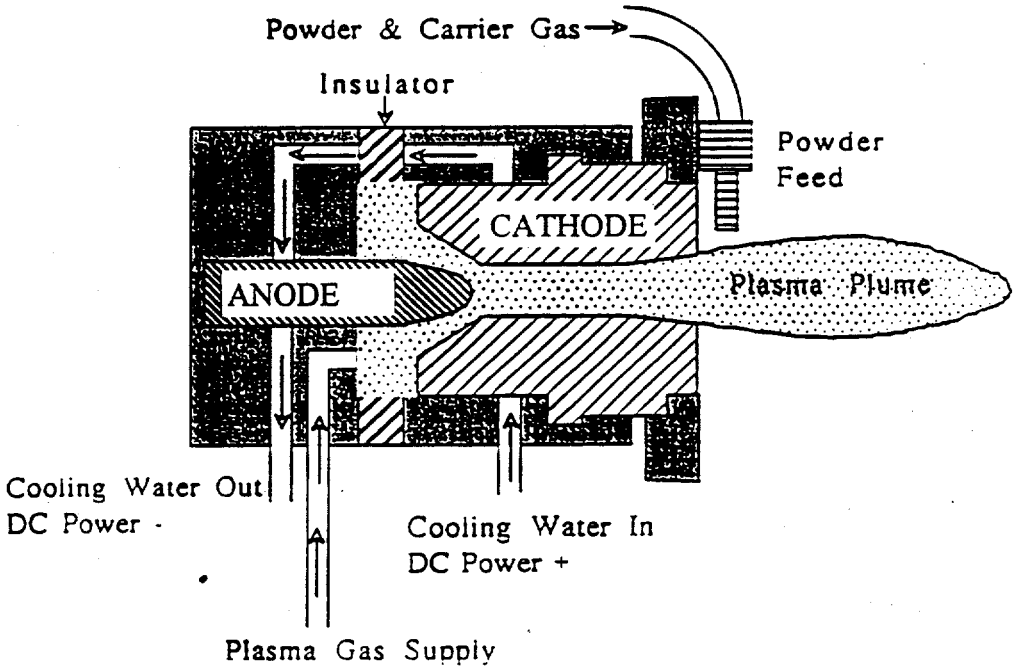

Figure II.3- Schematic of a typical plasma spray gun (**5**).

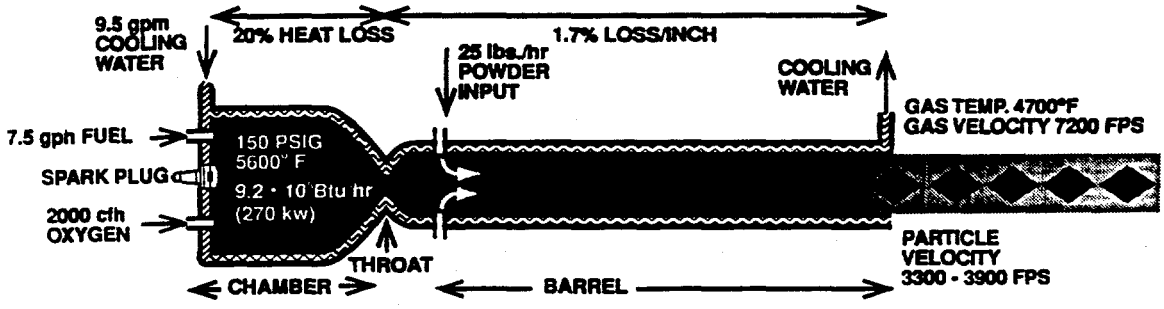

Figure II.4- Schematic of a typical HVOF torch (**14**).

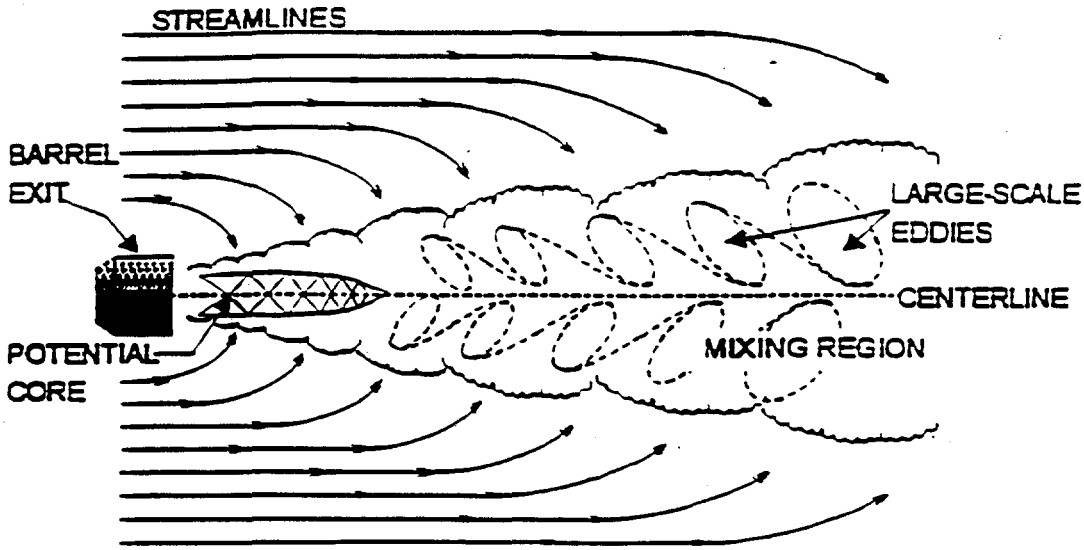

Figure II.5- Turbulent mixing of the HVOF jet and the surrounding atmosphere (**15**).

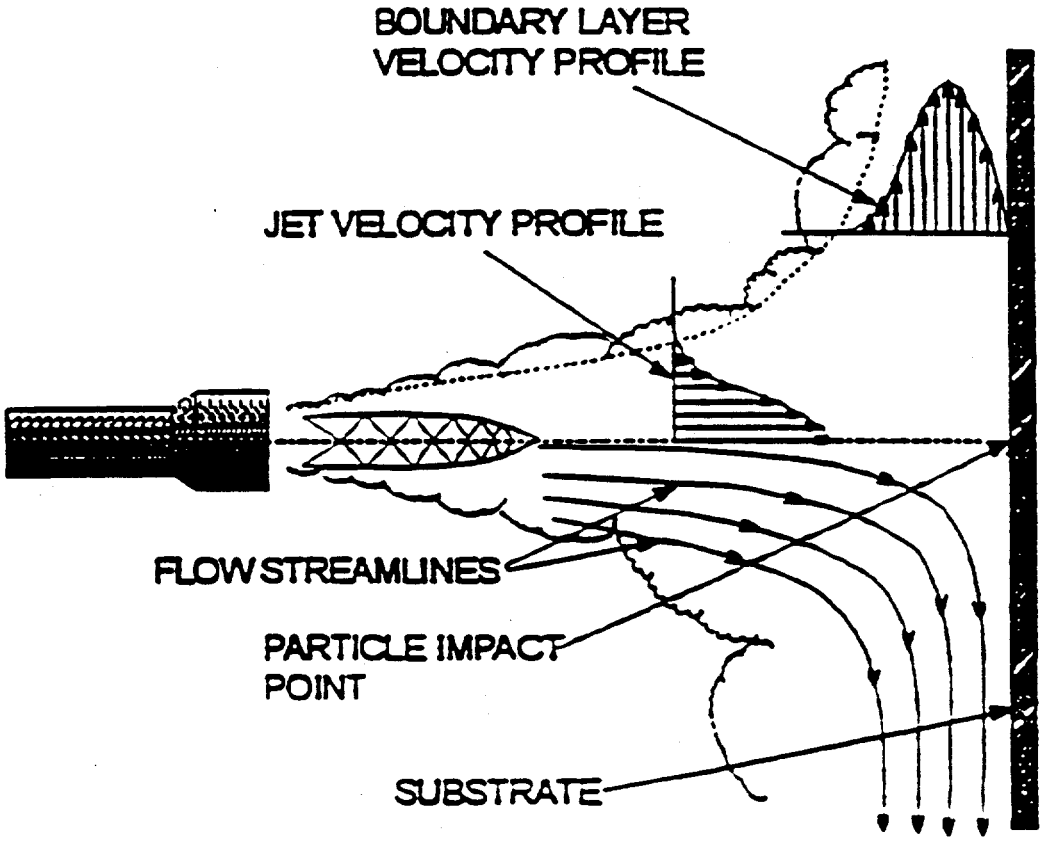

Figure II.6- HVOF jet impingement and boundary layer formation, causing oxygen to be trapped near the surface of the coating enhancing oxidation (**15**).

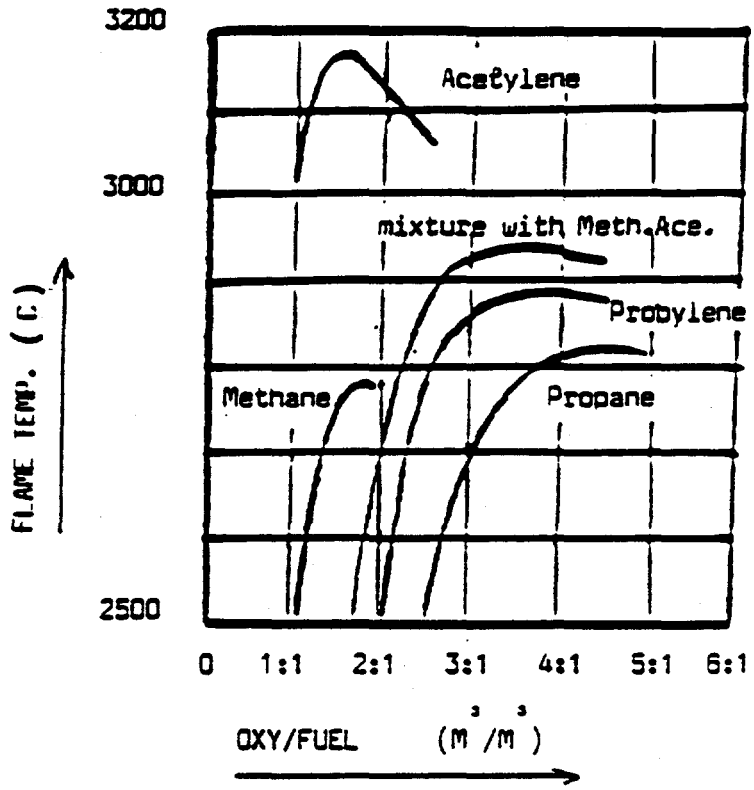

Figure II.7- Effect of fuel gas on flame temperature for the HVOF spray process (**16**).

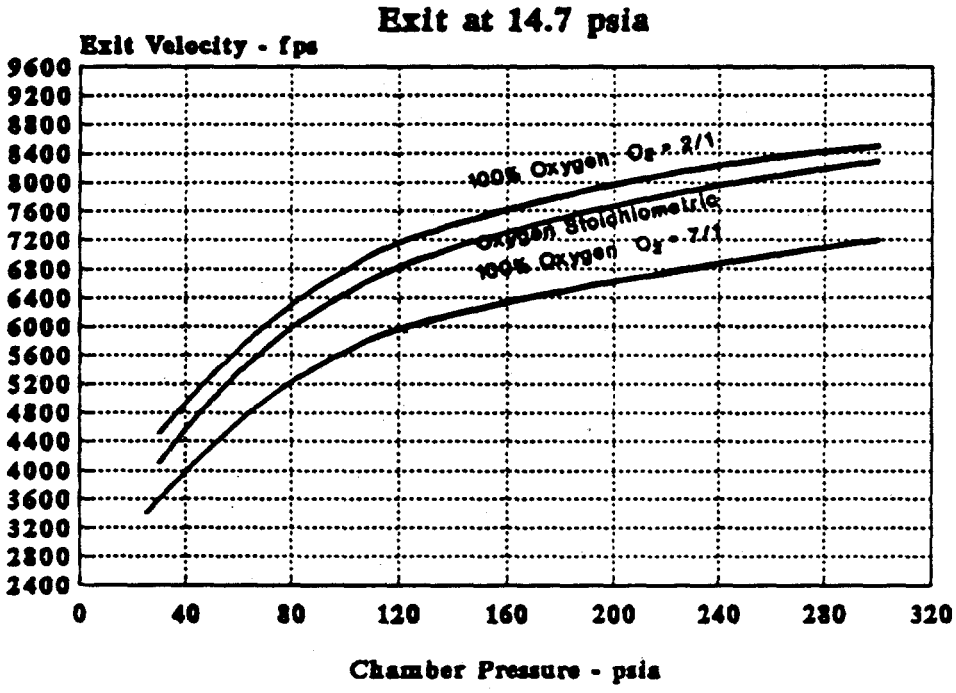

Figure II.8- Variation in exit velocity with chamber pressure and oxygen/fuel ratio for HVOF (14).

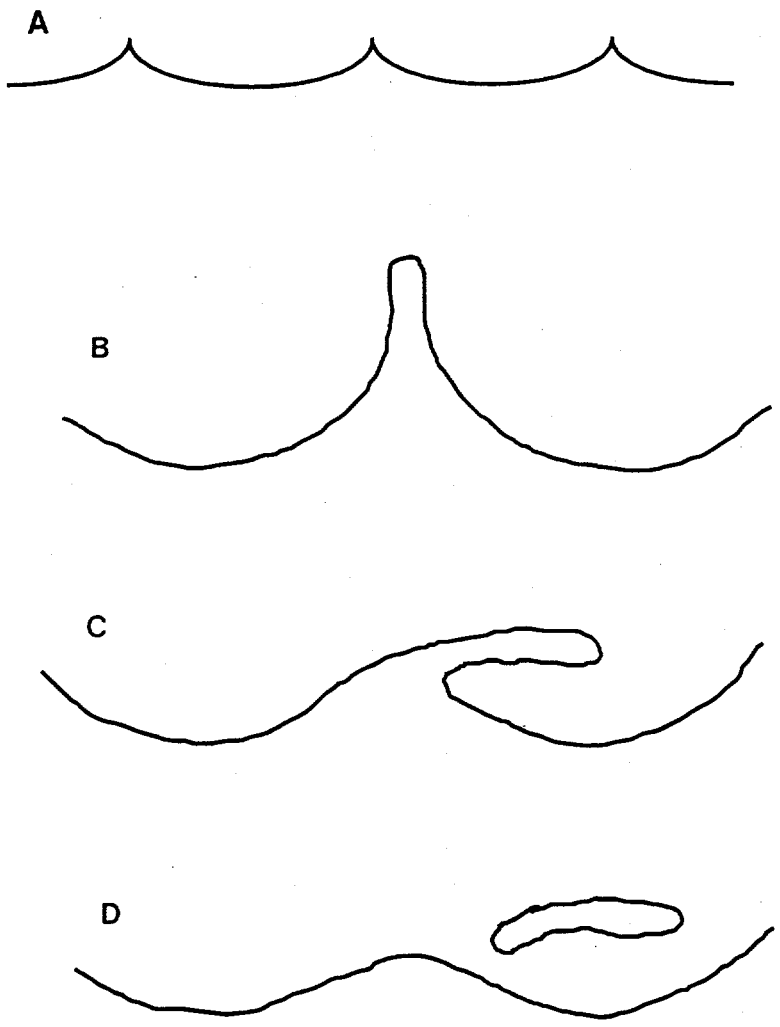

Figure II.9- Ripple formation and eventual material loss for pure ductile erosion (**20**):a. Ripple formation due to isolated impact events & b. subsequent impact results in severe plastic deformation associated with raised lipped craters, c. additional impact events result in the deformed area reaching its critical strain and d. eventually breaking off, resulting in material removal.

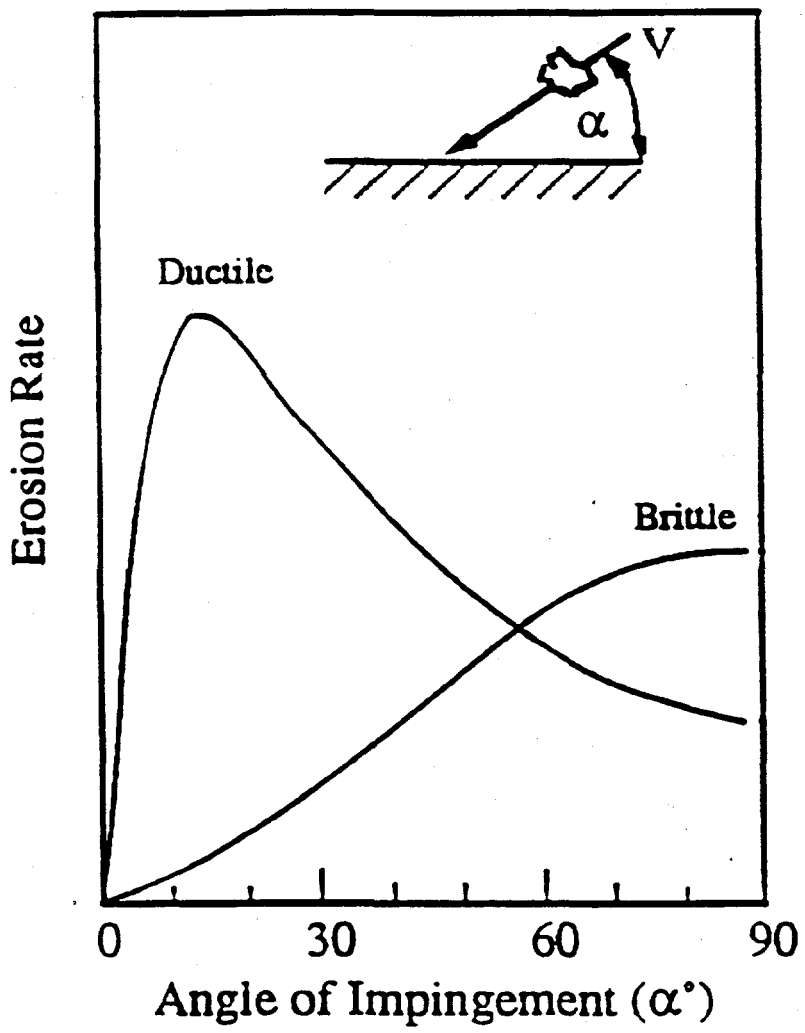

Figure II.10- Ideal erosion of both ductile and brittle materials for 30° & 90° impact angles (**19**).

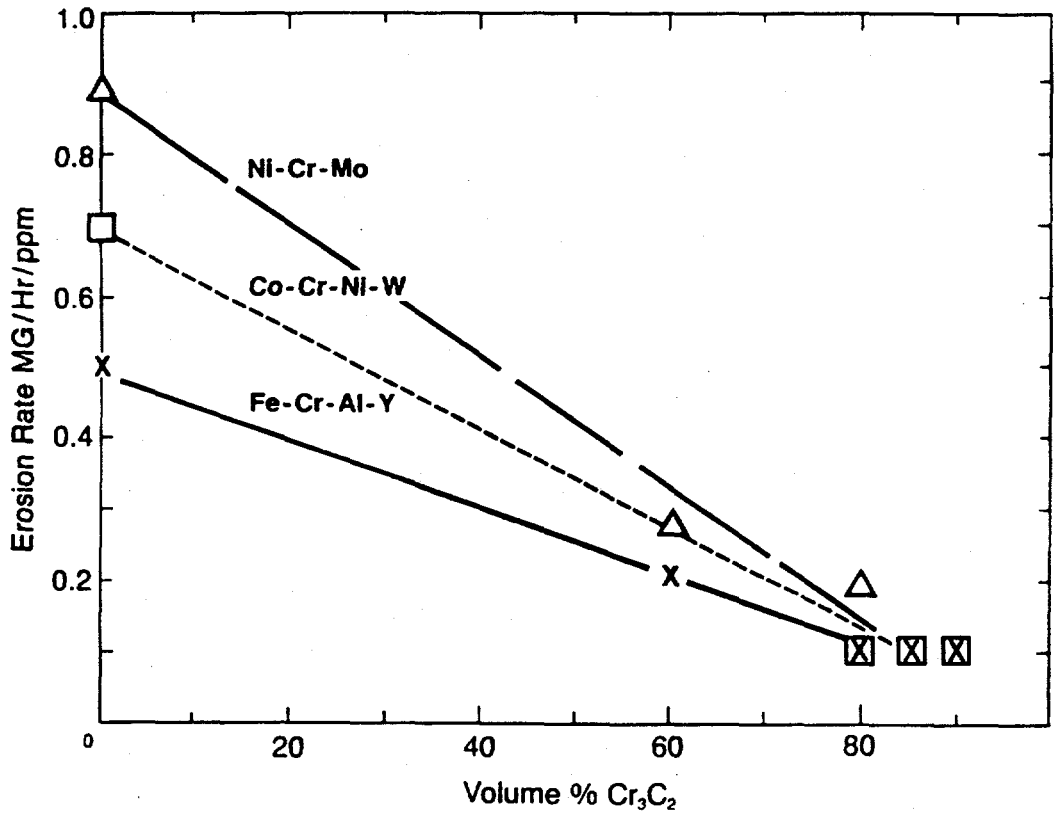

Figure II.11- Cr_3C_2 cermet plasma coating erosion results for various matrices and carbide concentrations (2).

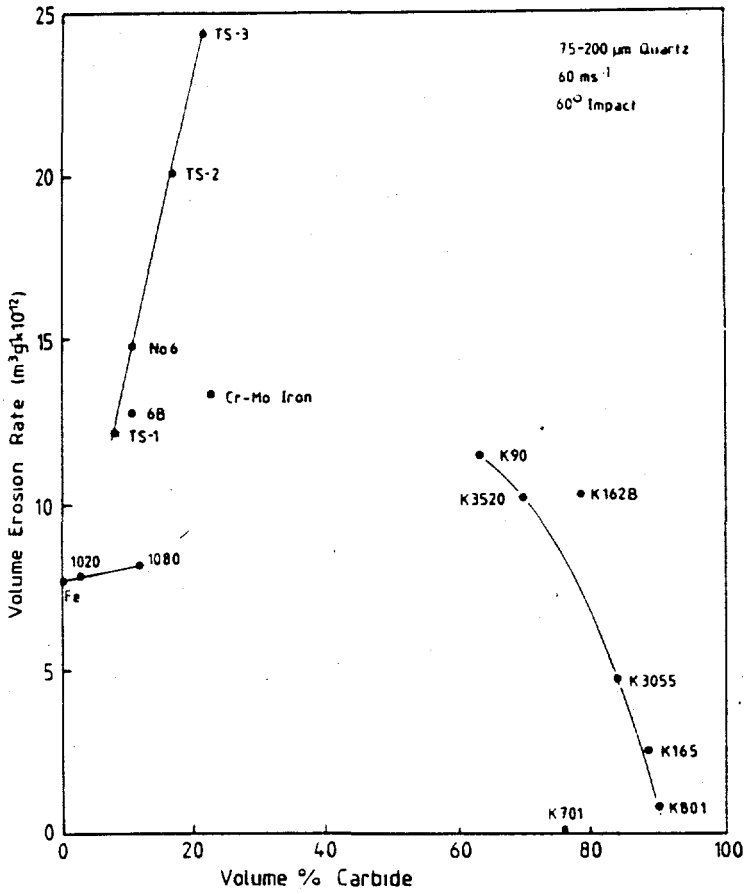

Alloy	Nominal composition, wt%	Carbide, vol%
Pure iron	Ingot iron	0
Spheroidized 1020	Fe-0.2C	3.1
Spheroidized 1080	Fe-0.8C	12.0
Stellite No. 6	Co-30Cr-4W-1.1C	10.4
Haynes 6B	Co-30Cr-4W-1.1C	10.4
Tristelle TS-1	Fe-30Cr-10Ni-12Co-5Si-1C	8.3
Tristelle TS-2	Fe-35Cr-10Ni-12Co-5Si-2C	16.8
Tristelle TS-3	Fe-35Cr-10Ni-12Co-5Si-3C	21.4
Cr-Mo white iron	Fe-20Cr-2.5Mo-2.6C	23.1
K90	WC-25Co	63.1
K3520	WC-20Co	69.5
K3055	WC-10Co	83.7
K701	WC-10Co-4Cr	76.2
K801	WC-5.7Ni-0.4Co	89.9
K162B	TiC-6NbC-2WC-25Ni-7Mo	78.5
K165	TiC-7WC-2.5NbC-9Ni-9Mo	88.8

Figure II.12- Erosion results indicating a potential minimum erosion rate at around 85% hard phase content (**27**).

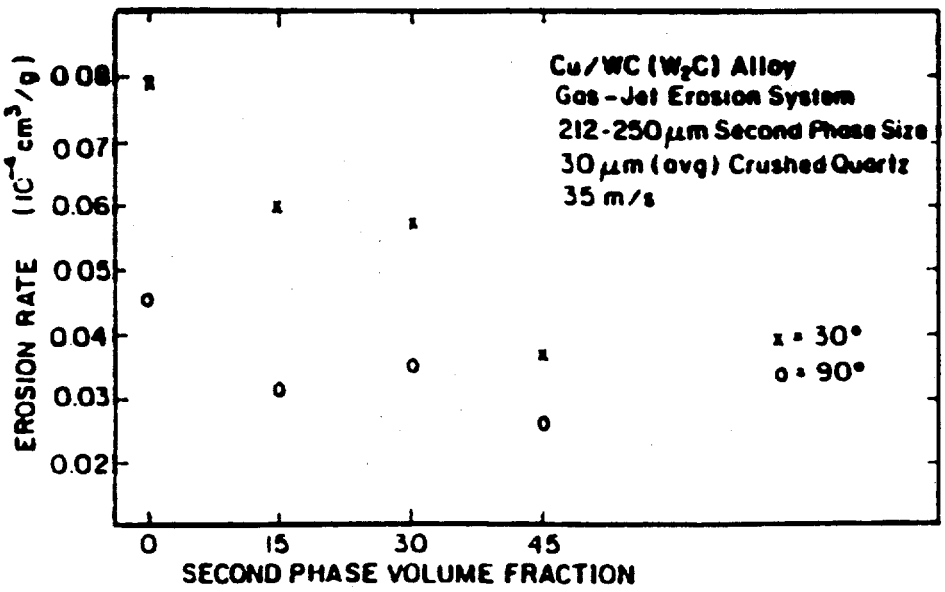

Figure II.13- Mild erosion condition results for Cu-Cr_3C_2 cermets at 90° (5): 30μm crushed quartz particles and 35m/s (28).

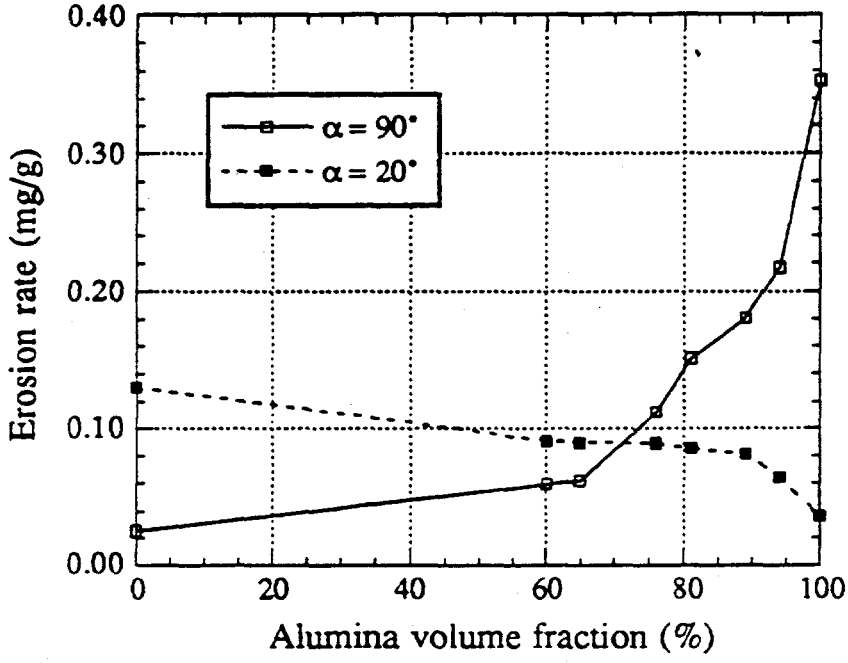

Figure II.14- Erosion results for aluminum-alumina plasma sprayed composites at 90° and 30° impact (29).

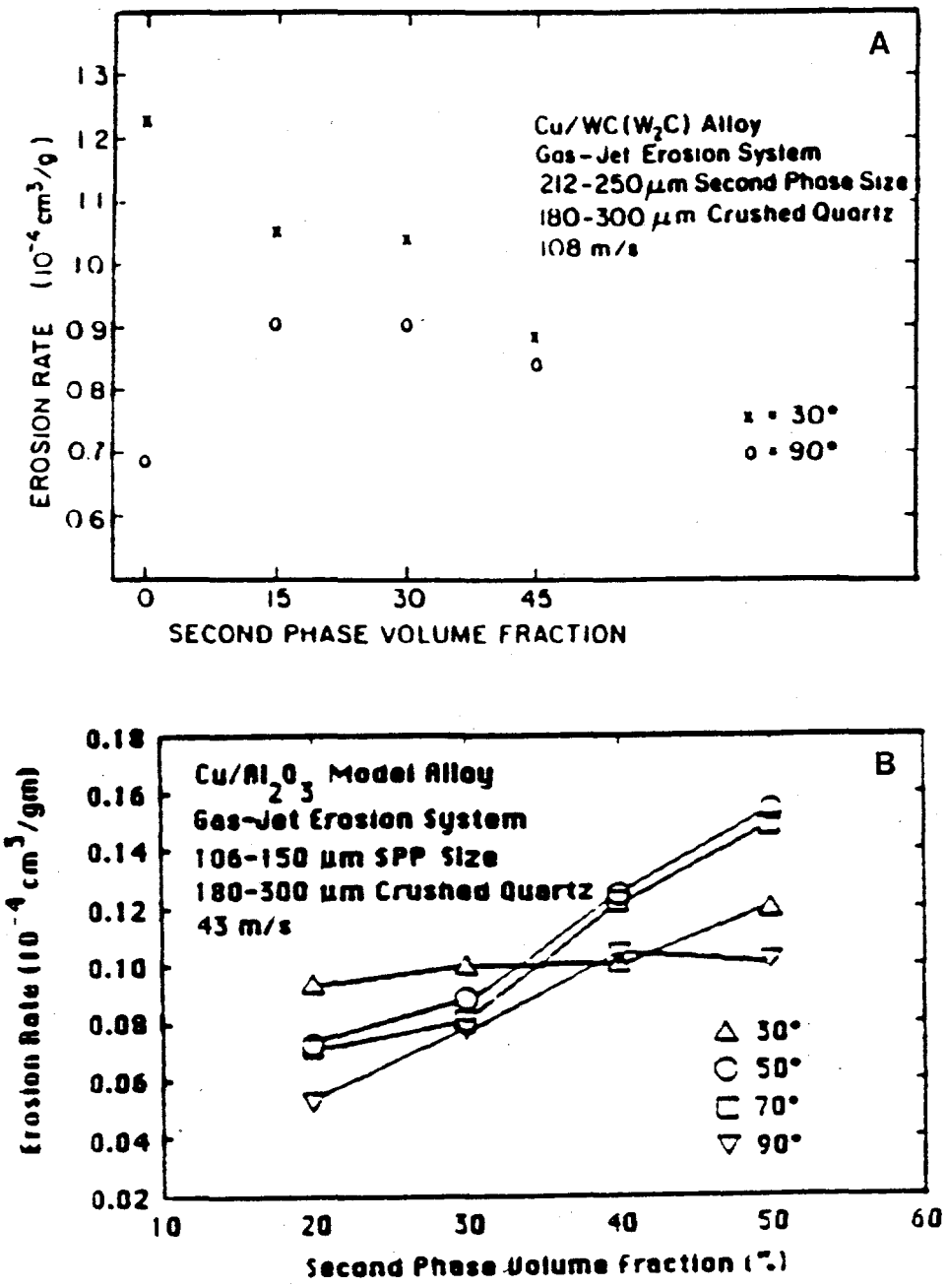

Figure II.15- Aggressive erosion results for a.Cu-Cr_3C_2 and b.Cu-Al_2O_3 cermets at 90°: 180-300μm crushed quartz particles and 80m/s (28).

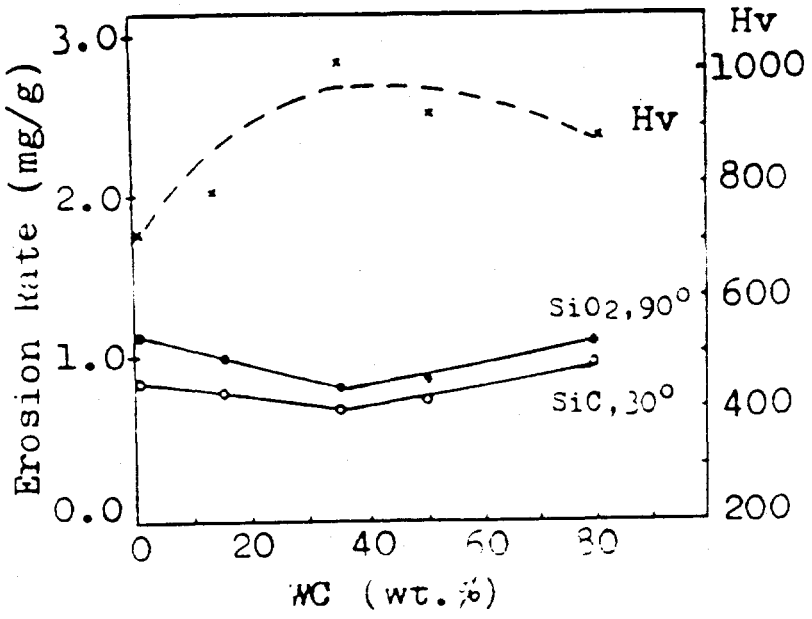

Figure II.16- Erosion results for WC-Co cermets at 90° impact (**30**).

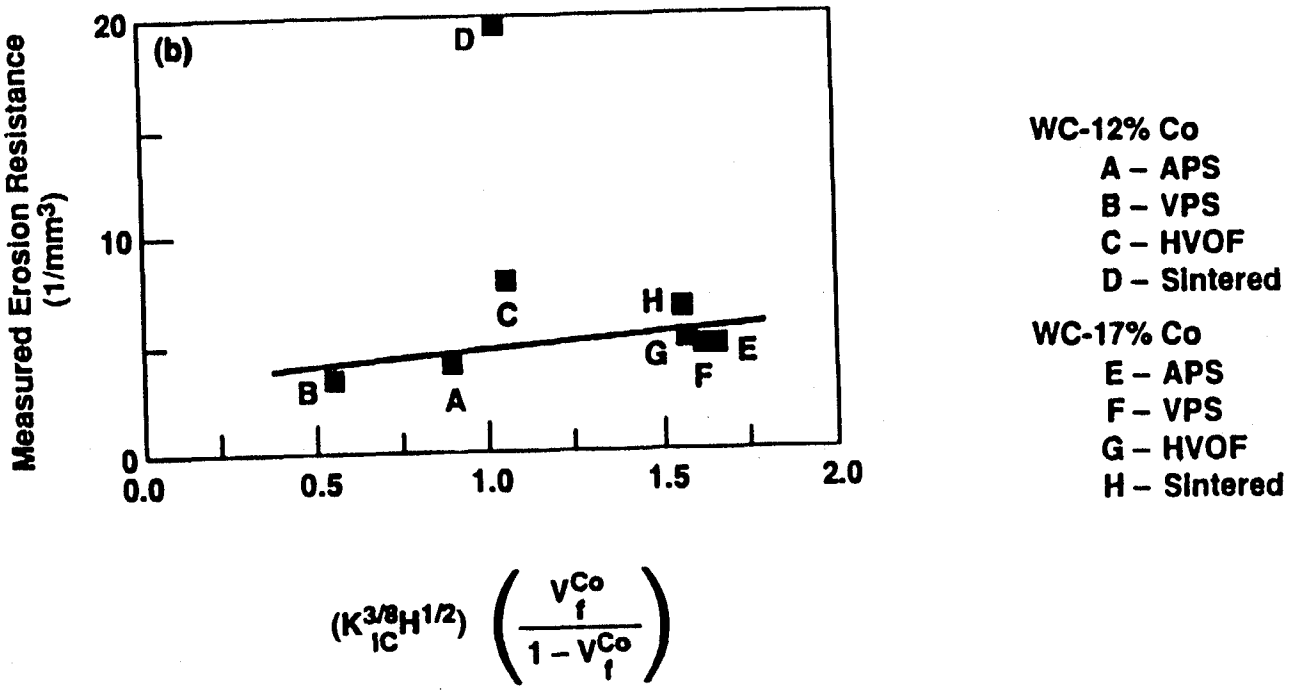

Figure II.17- Erosion data versus proposed microstructure/mechanical property parameter (12).

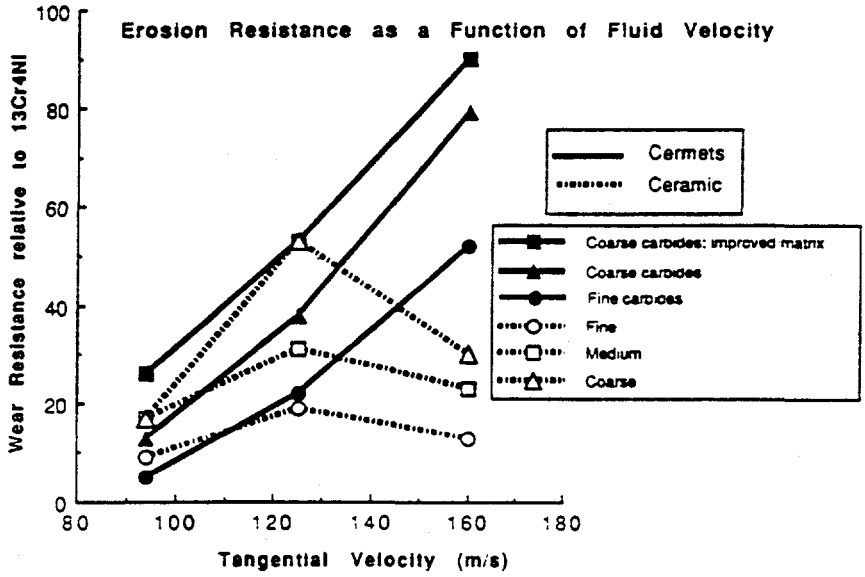

Figure II.18- Erosion rate versus particle velocity for various carbide reinforcement sizes (**31**).

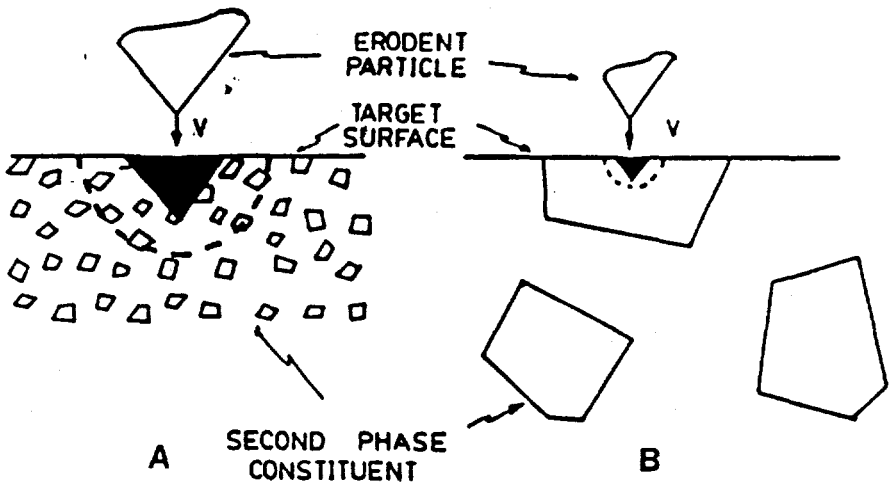

Figure II.19- Erodent size - hard phase (E/HP) ratio schematic: a. Large E/HP leading to matrix toughening and ductile failure --> lower erosion rates & b. Small E/HP leading to hard phase fracture and brittle failure --> higher erosion rates (32).

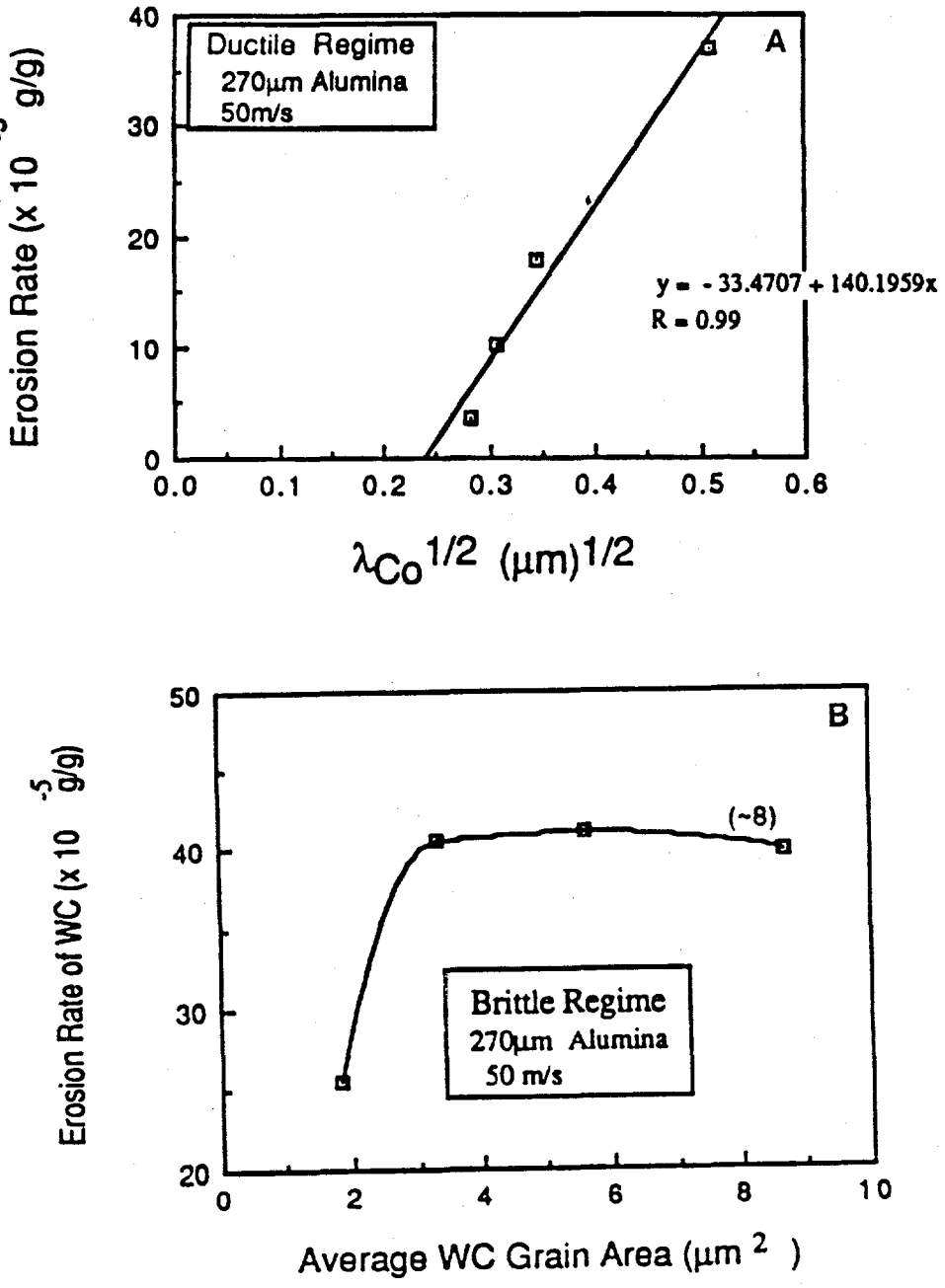

Figure II.20- Erosion rate versus various microstructural features for a.Ductile regime and b. Brittle regime (32).

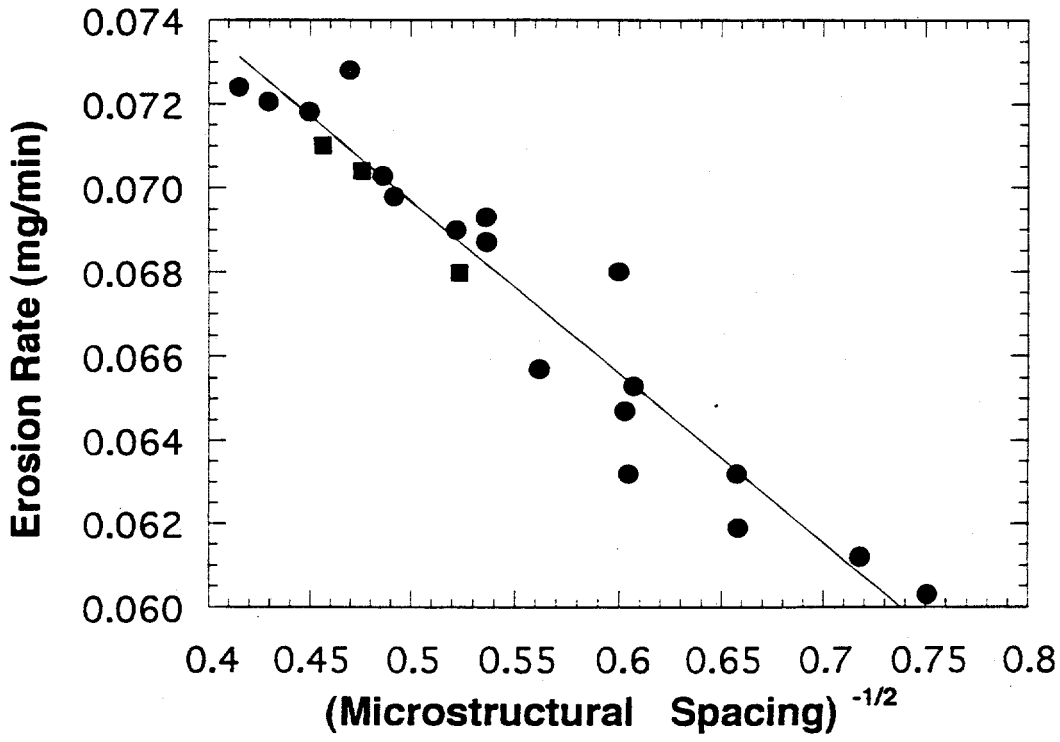

Figure II.21- Erosion rate versus 1/(microstructural spacing)$^{-1/2}$ for shperodized plain carbon steels (**26**).

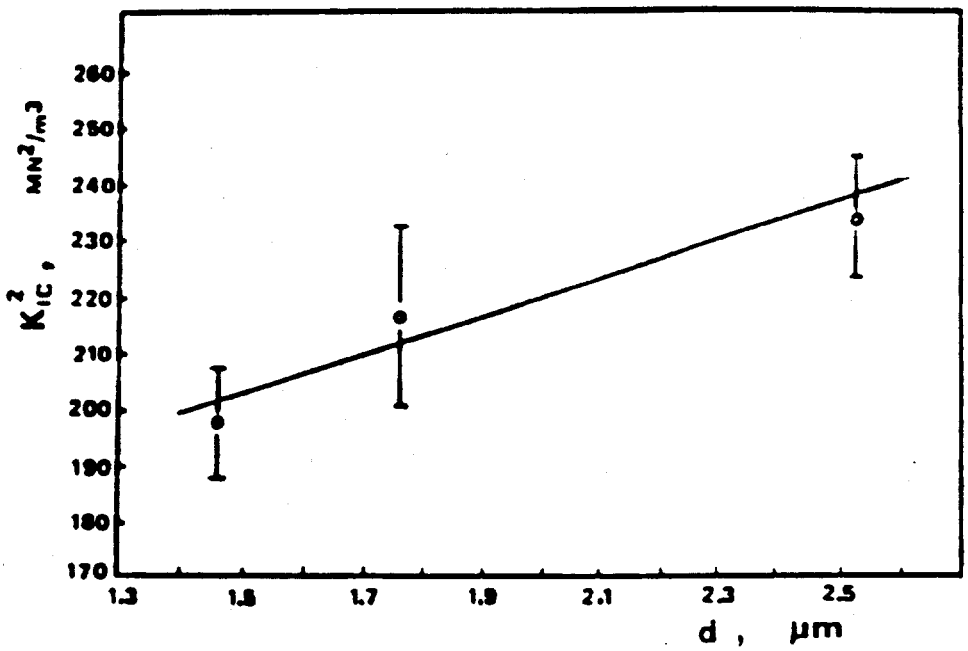

Figure II.22- WC-Co cermet toughness versus the size of the carbide reinforcement (33).

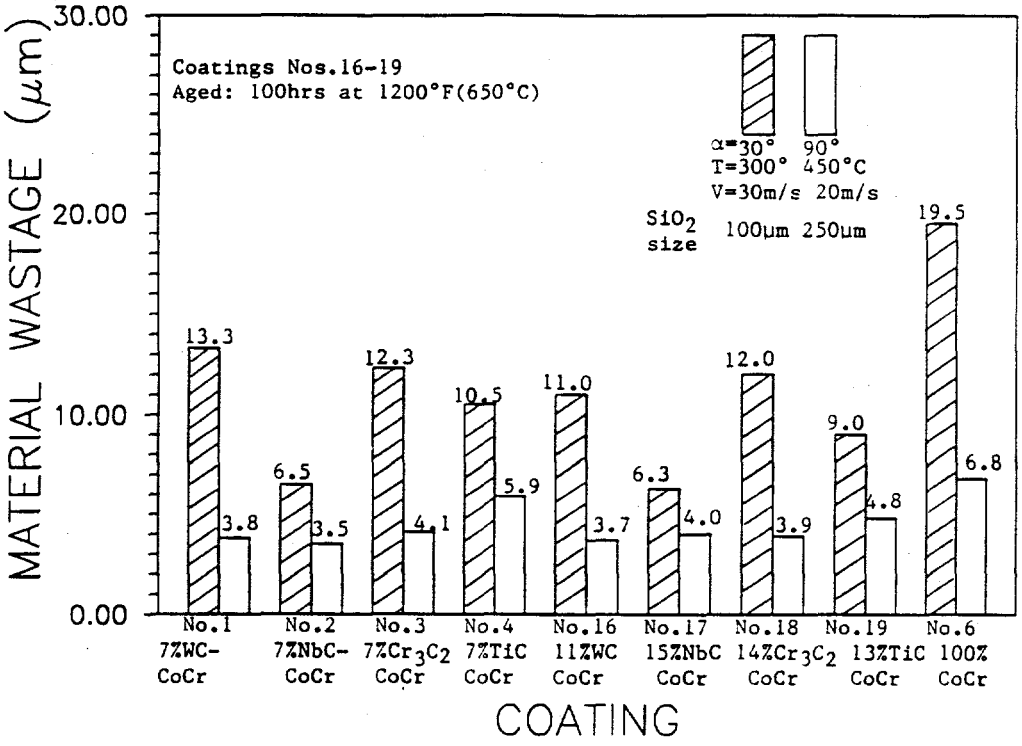

Figure II.23- Erosion rates for various CoCr-carbide cermets (35).

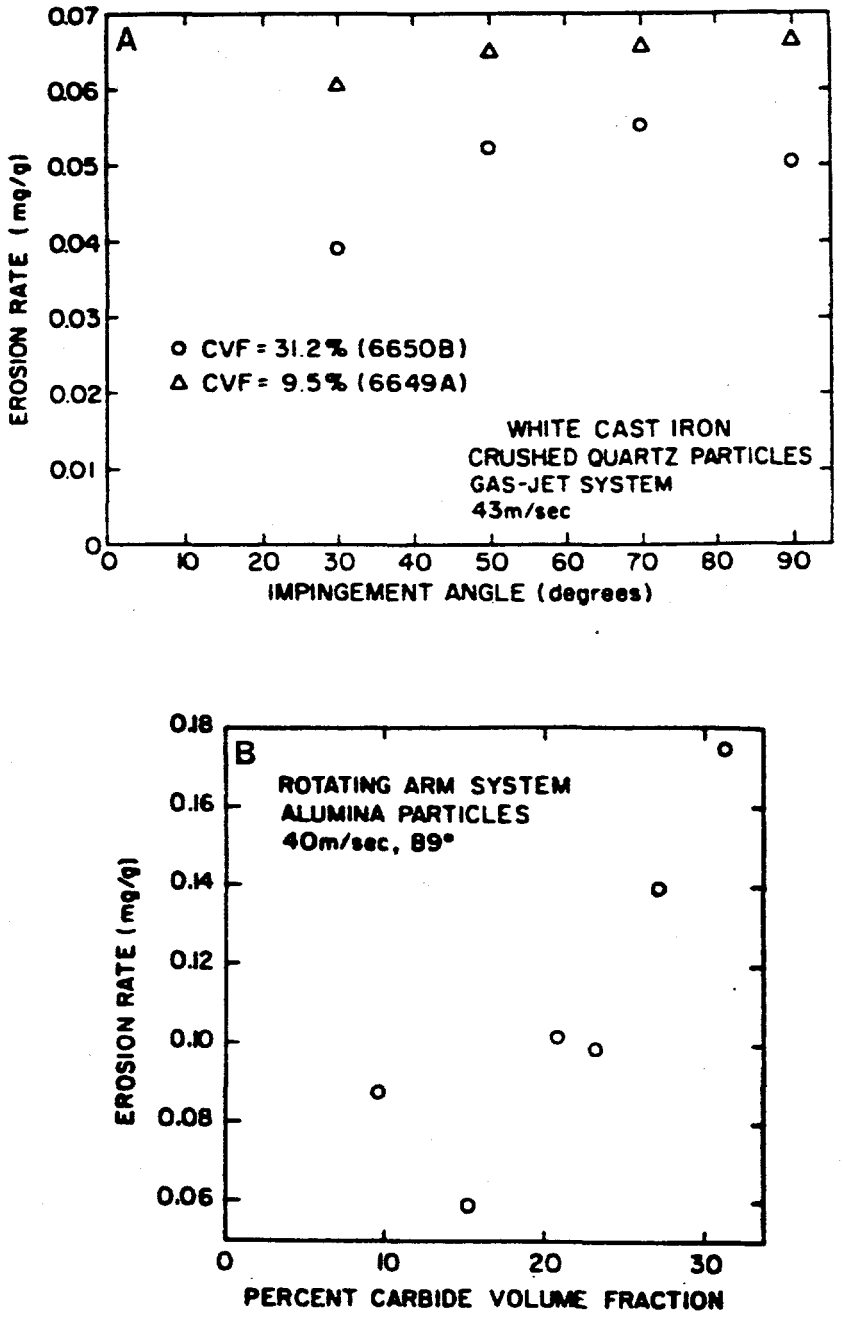

Figure II.24- White cast iron erosion data for a.Crushed quartz and b. Alumina (36).

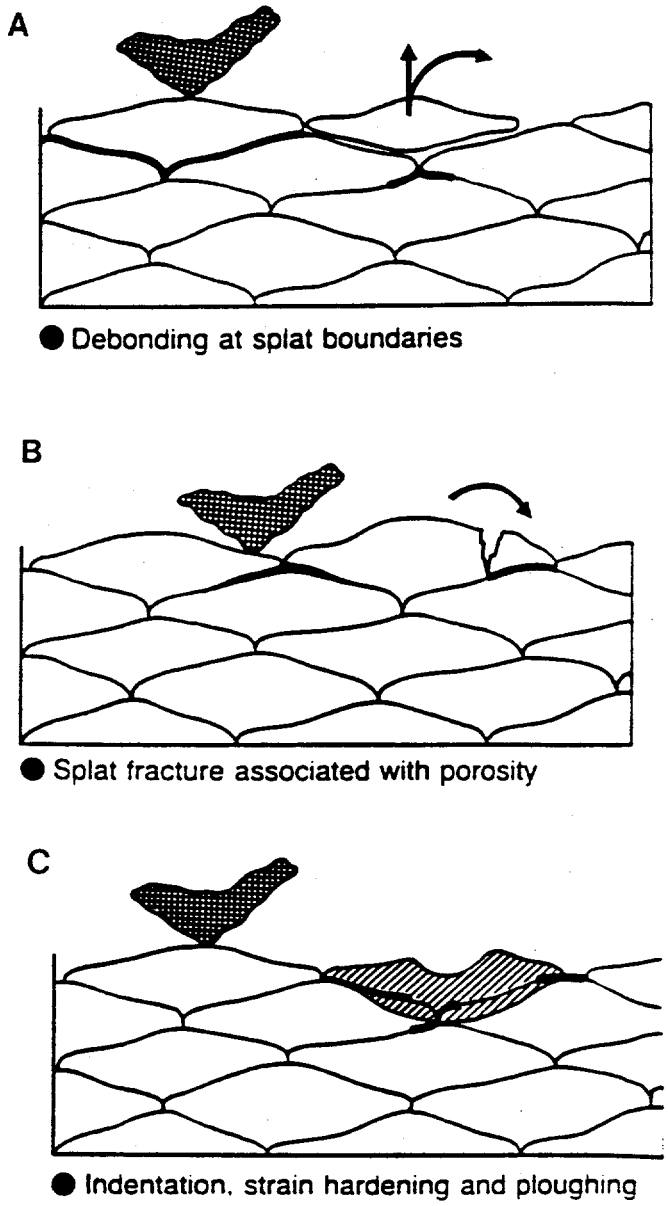

Figure II.25- Erosion failure mechanisms for thermal spray coatings: a) Splat debonding, b) Splat fracture associated with porosity , and c) Splat deformation (**21**).

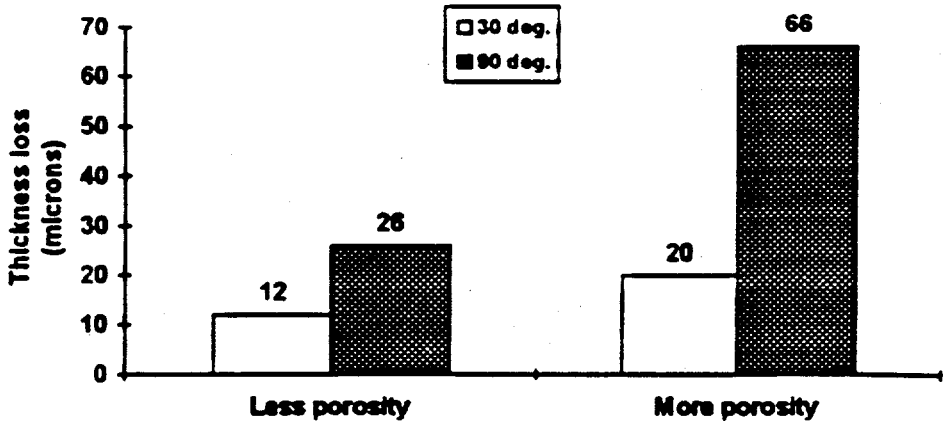

Figure II.26- Erosion results for similar WC-Co cermets with varying porosity levels (**41**).

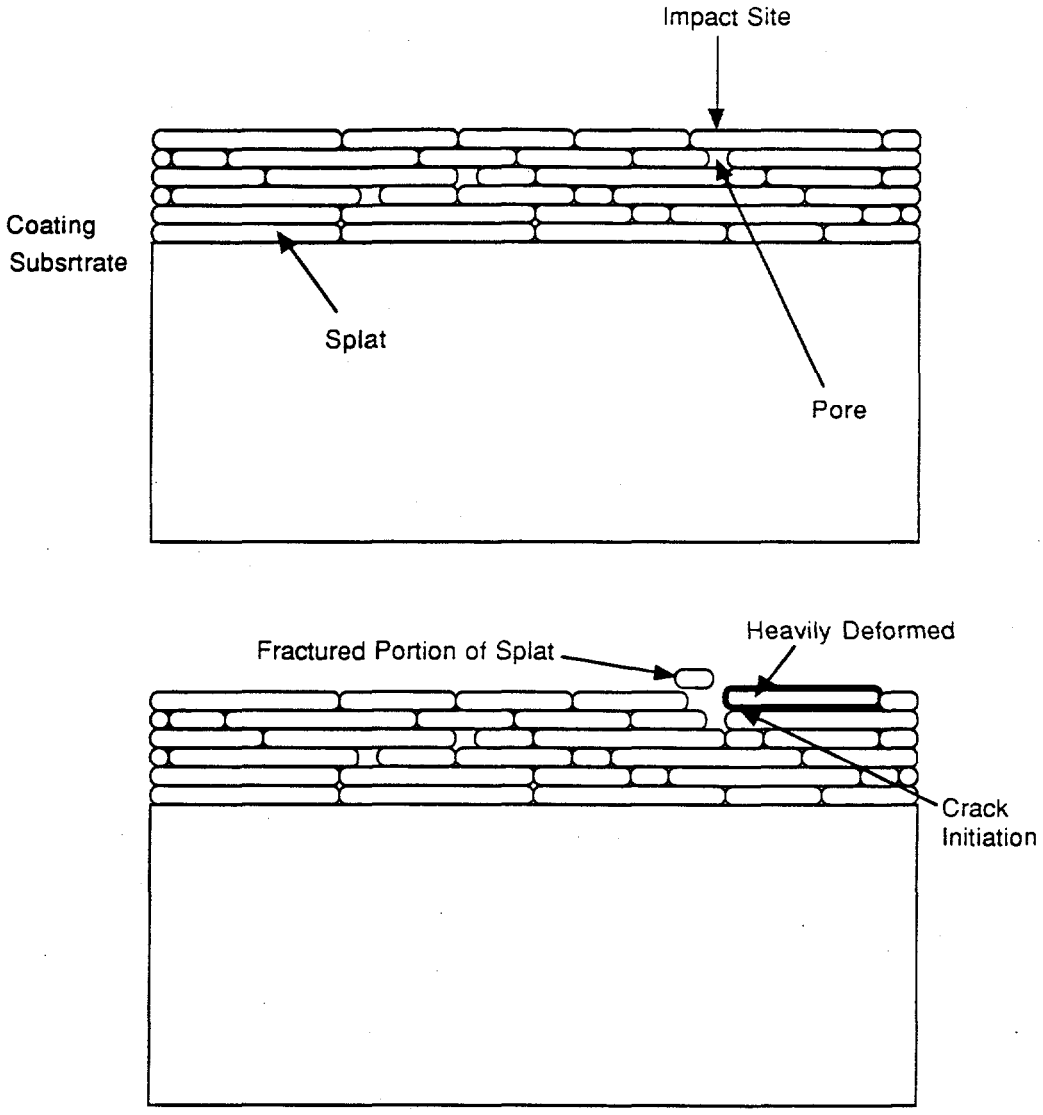

Figure II.27- Splat fracture and delamination associated with porosity of an impacting particle striking a splat directly above a pore. Due to the lack of support for the splat, excessive deformation and eventual splat fracture may occur or impact may be absorbed by the relatively weak splat to splat bonds failing resulting in delamination.

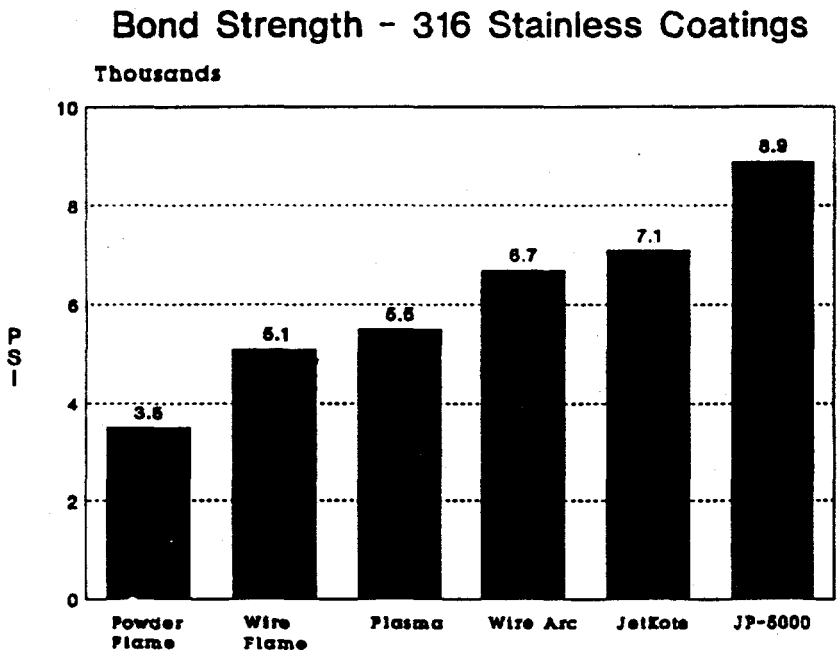

Figure II.28- Cohesion values for various thermal spray processes (**17**).

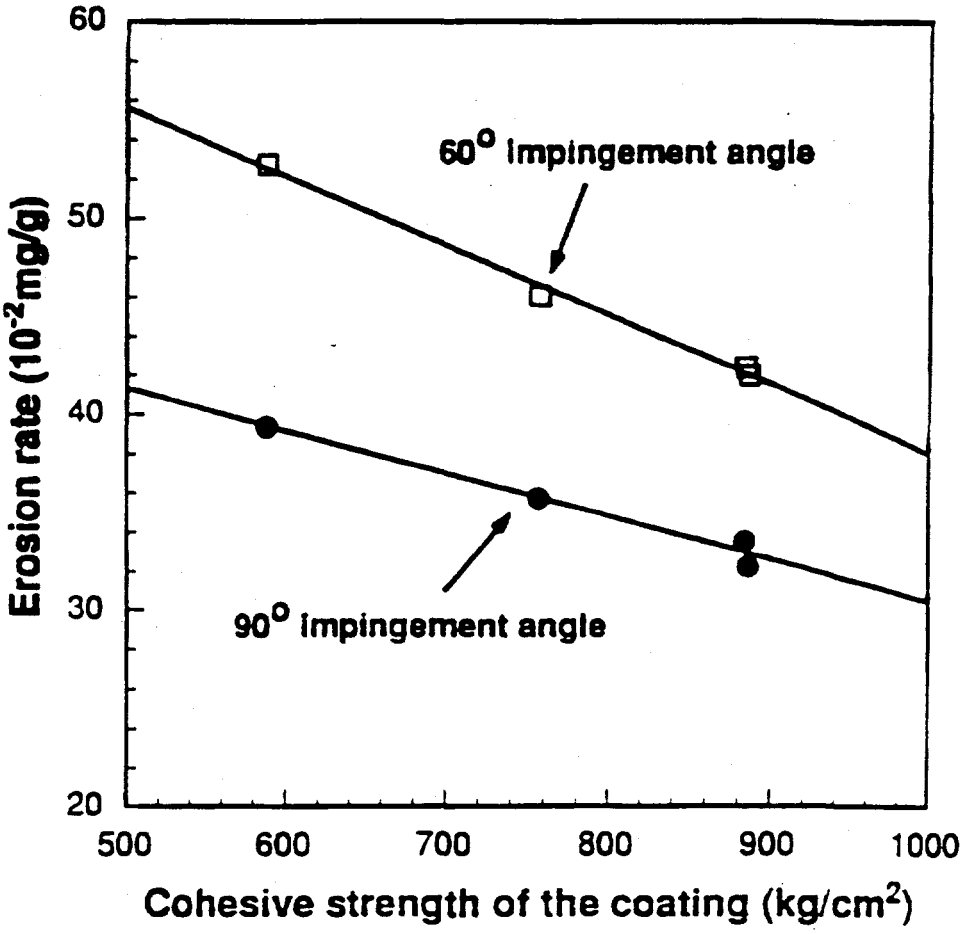

Figure II.29- Erosion rate versus cohesive strength for HVOF coatings (6).

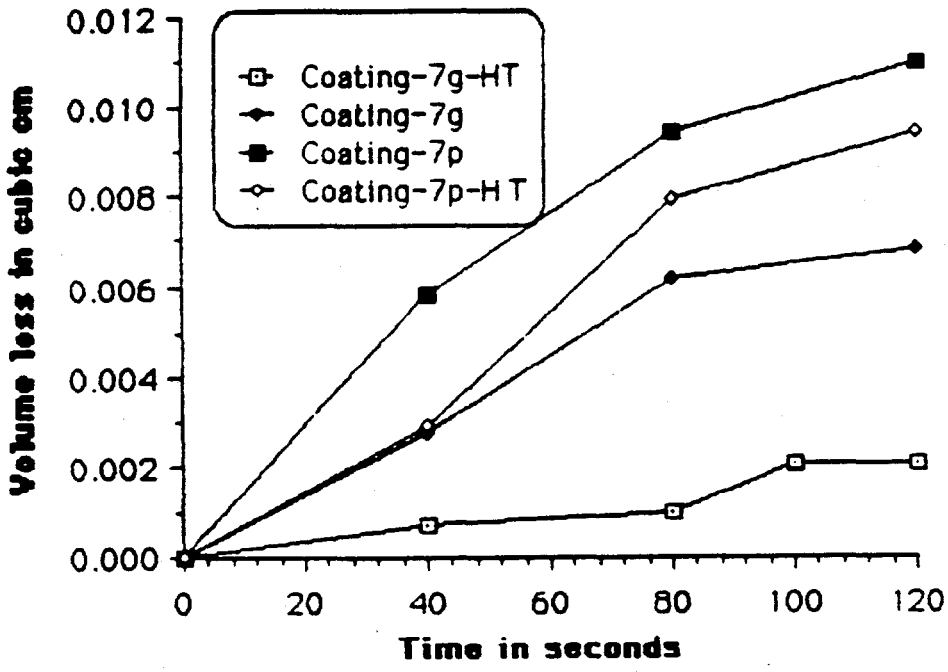

Figure II.30- Comparison of erosion performance of as-sprayed and post heat treated coatings (**11**).

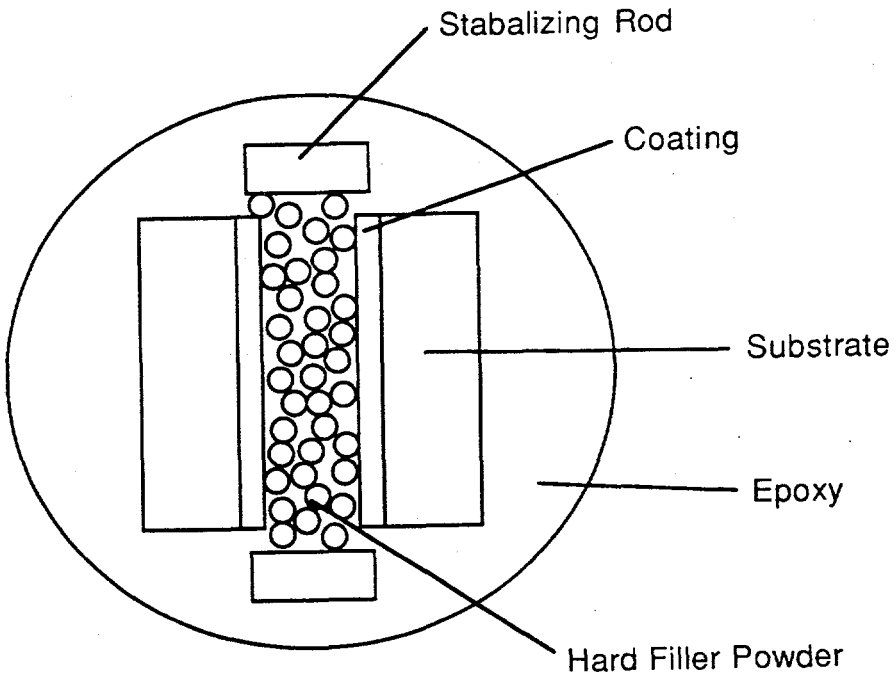

Figure III.1- Schematic of thermal spray mounts.

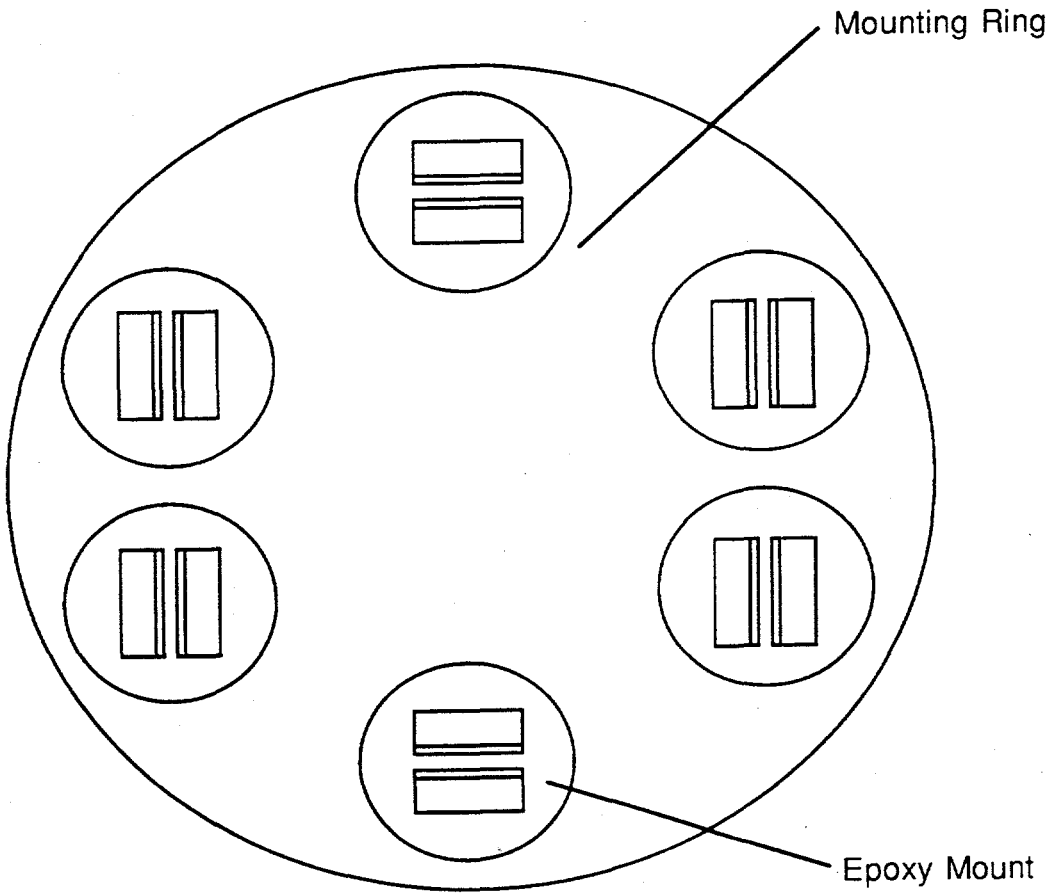

Figure III.2- Specimen orientation in Abrapol ring holder.

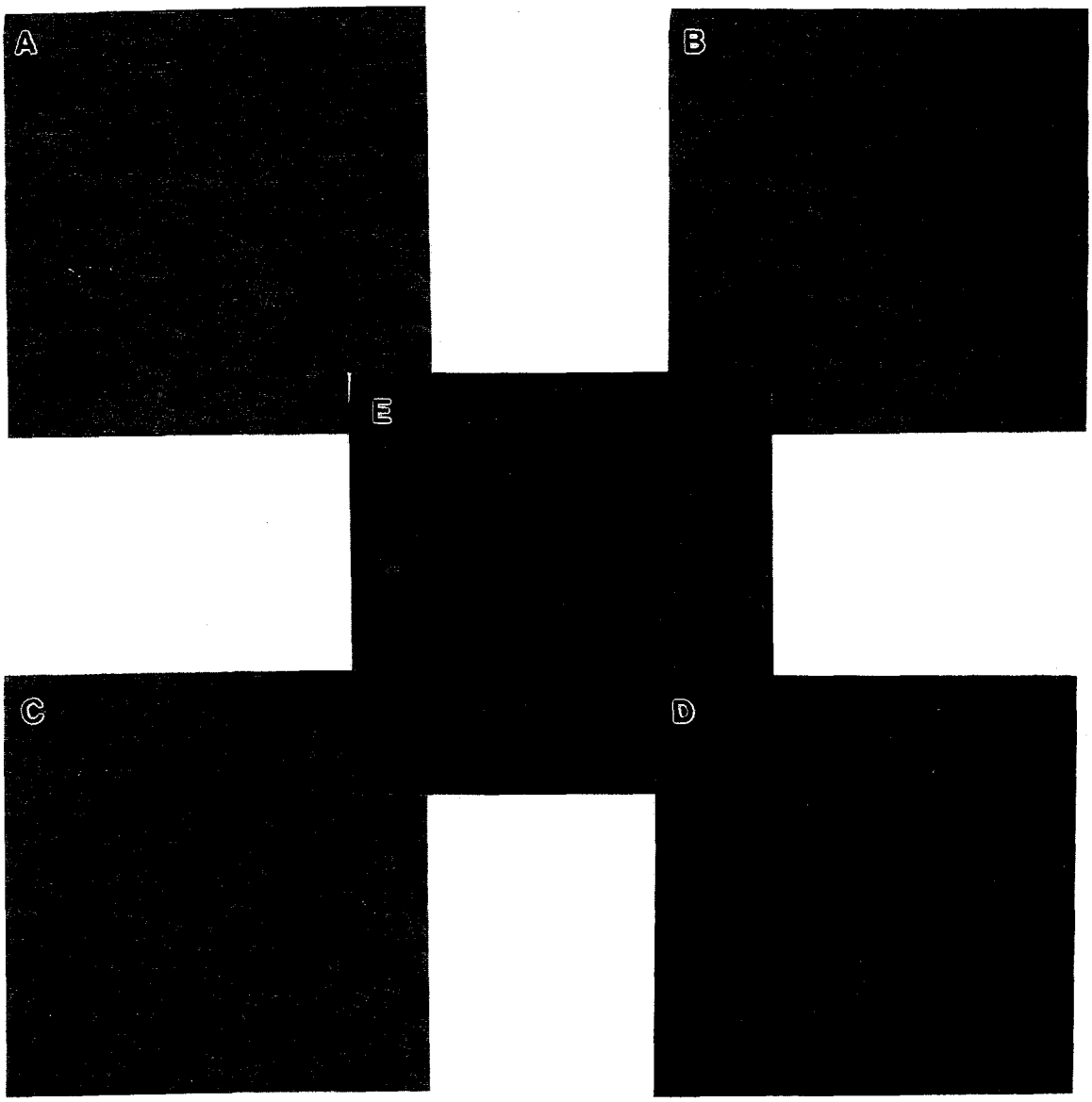

Figure III.3- Thresholding process for a 40% Al_2O_3-60% FeAl APS coating: a. coating b. coating with porosity highlighted, c. coating with alumina highlighted, d. coating with FeAl highlighted, and e. thresholding of the entire coating.

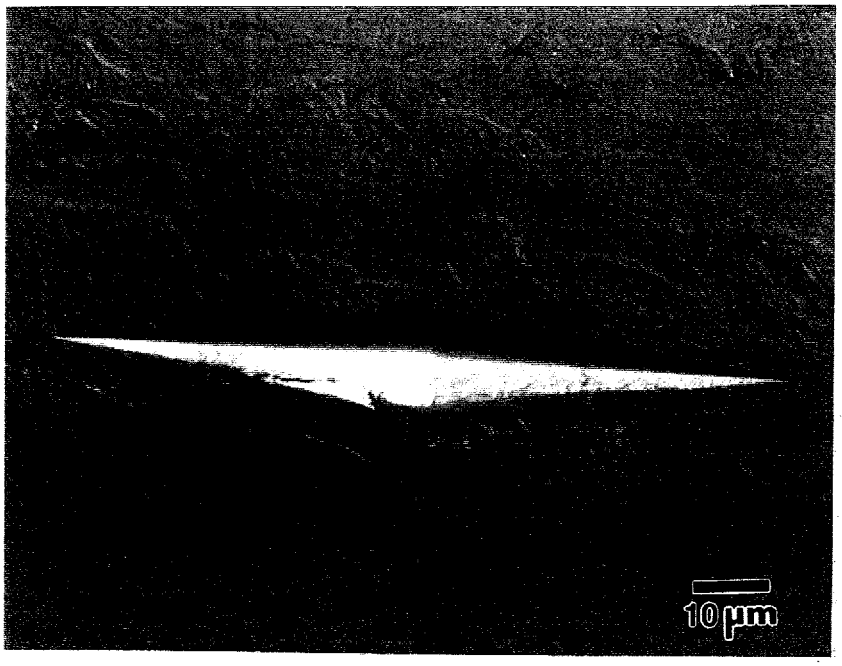

Figure III.4- Typical 300g Knoop indentation (25-45µm HVOF spayed FeAl).

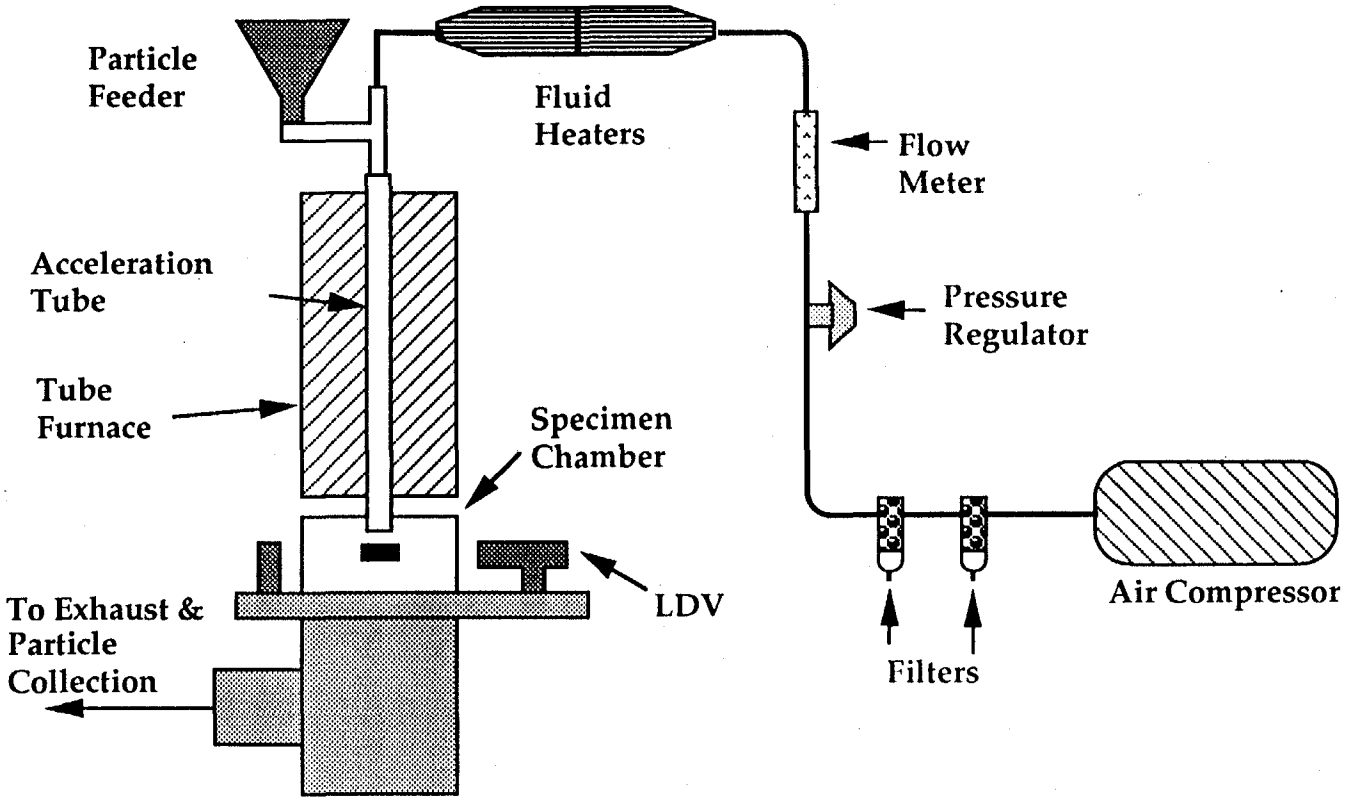

Figure III.5- Erosion tester schematic.

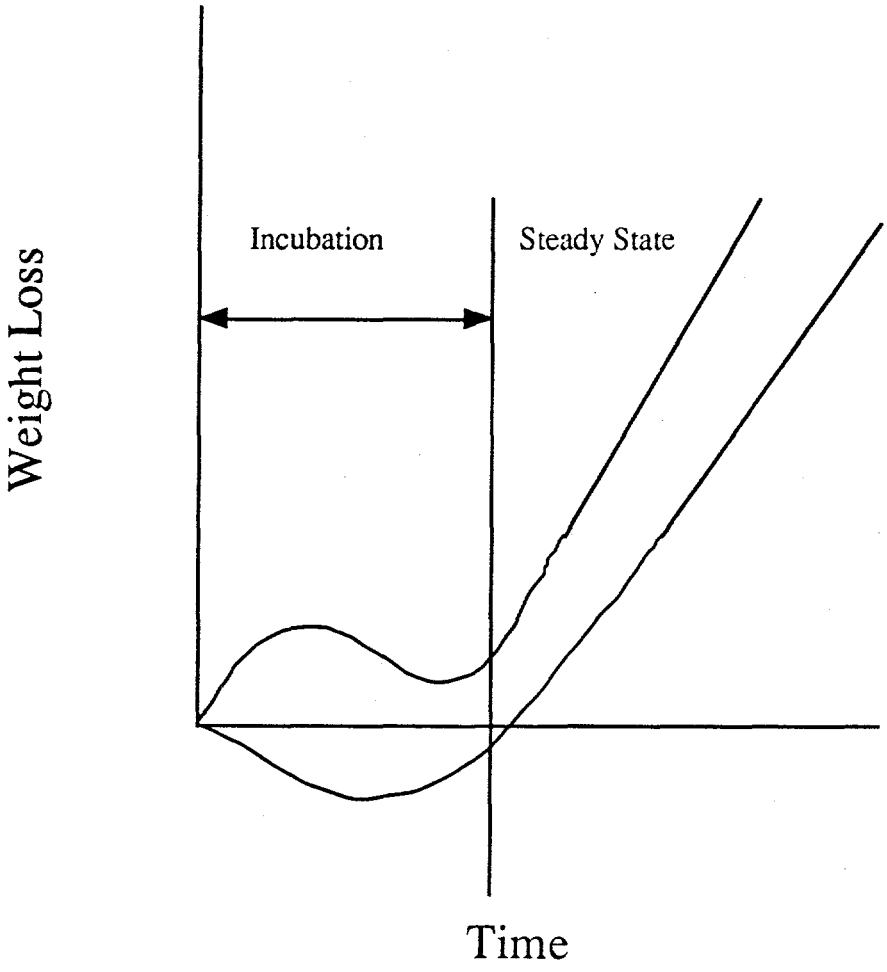

Figure III.6- Weight loss versus time showing steady state erosion regime.

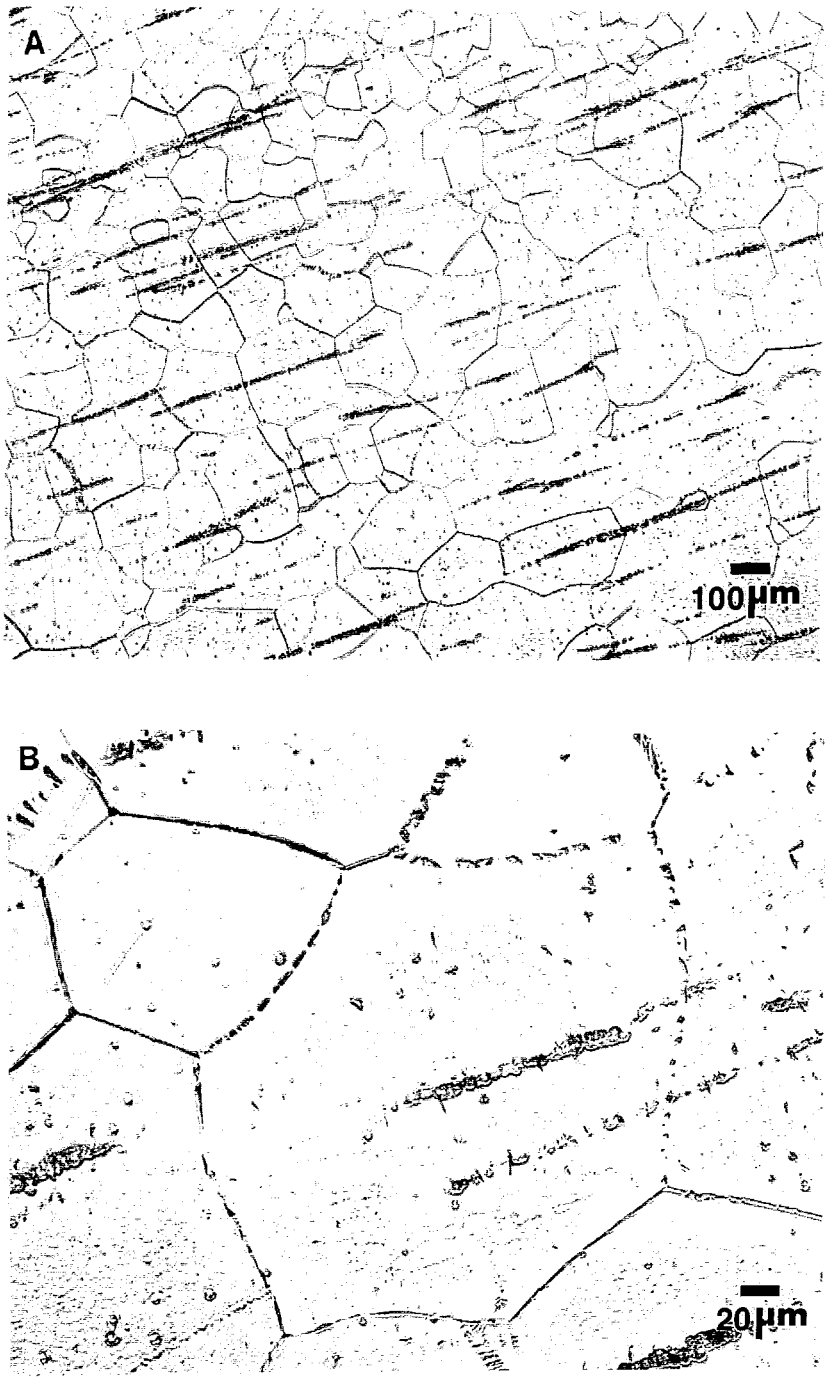

Figure IV.1- Wrought FeAl microstructures: a. 50x, b.250x.

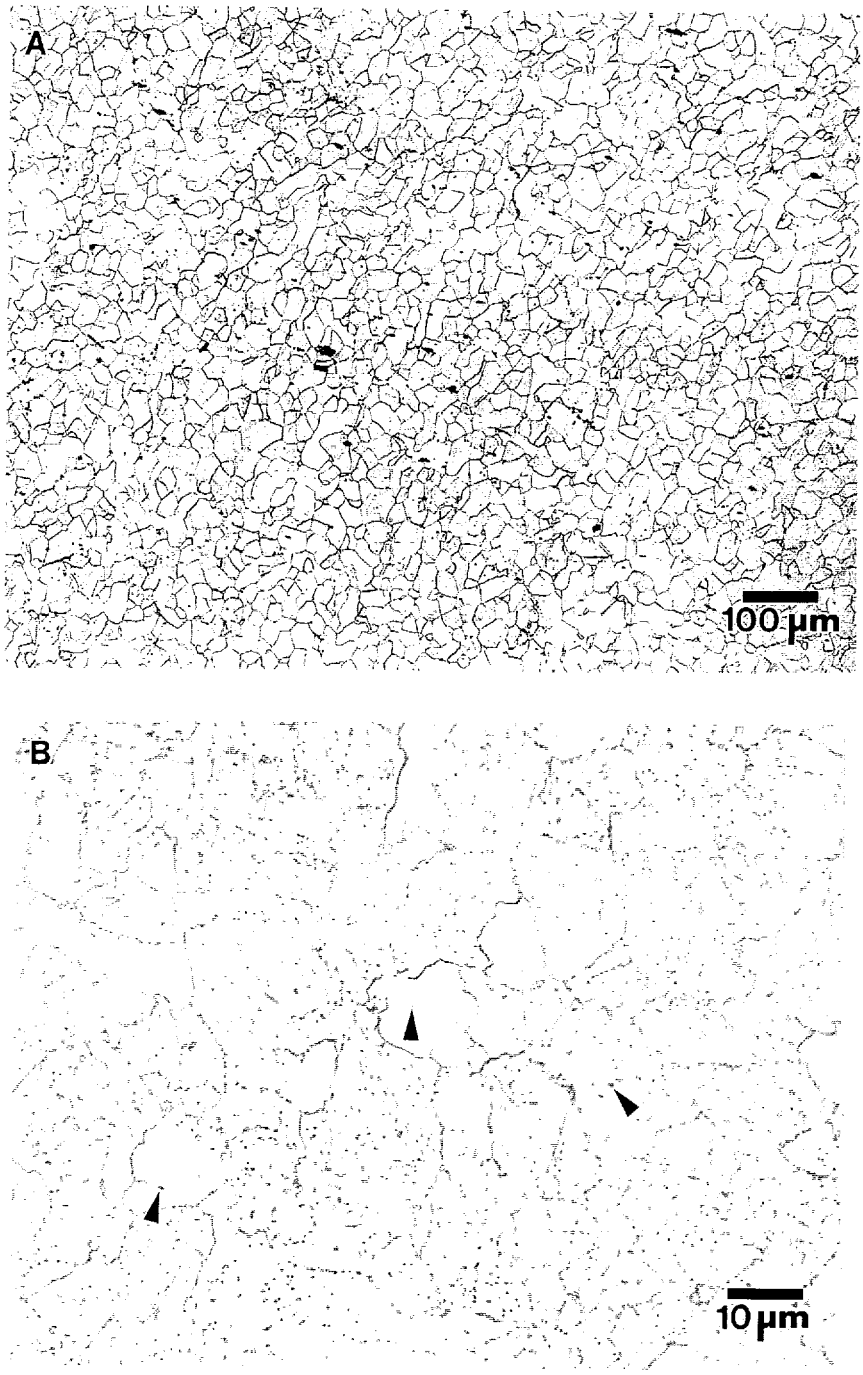

Figure IV.2- CrMo steel microstructures (T-11): a.100x, b.1000x.

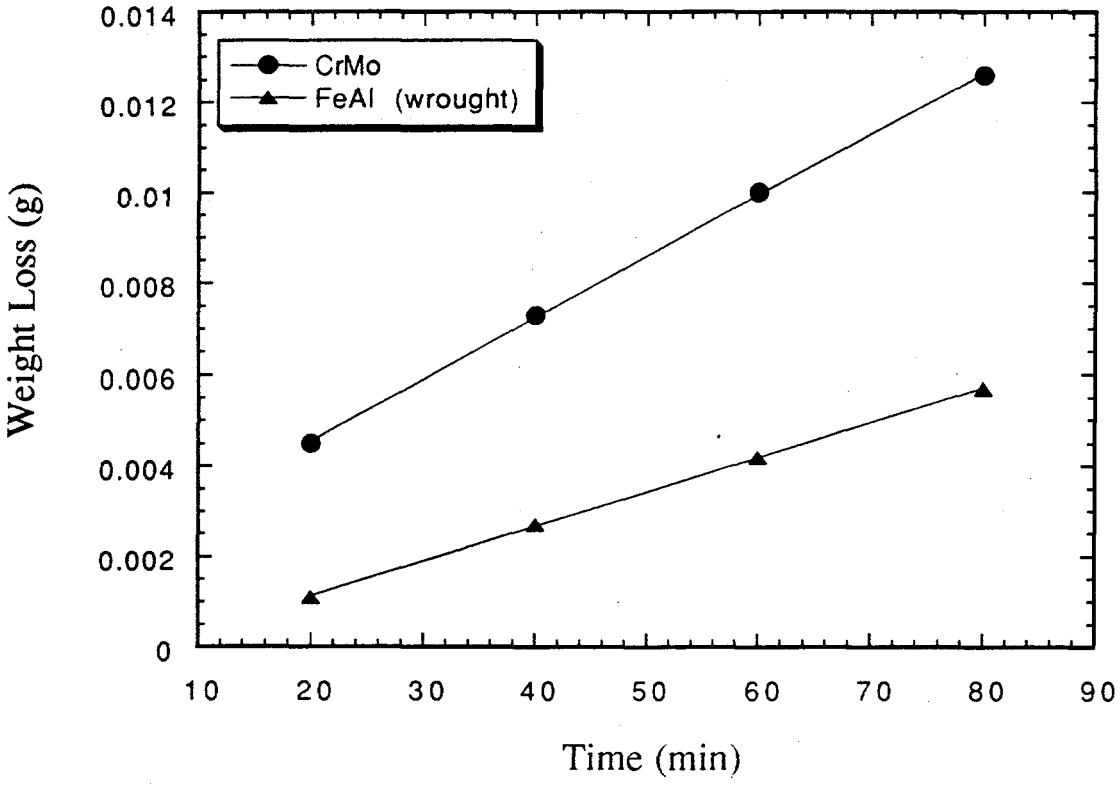

Figure IV.3- Weight loss versus time curves for CrMo steel and wrought FeAl, beginning time data was omitted to ensure accurate steady state erosion calculation.

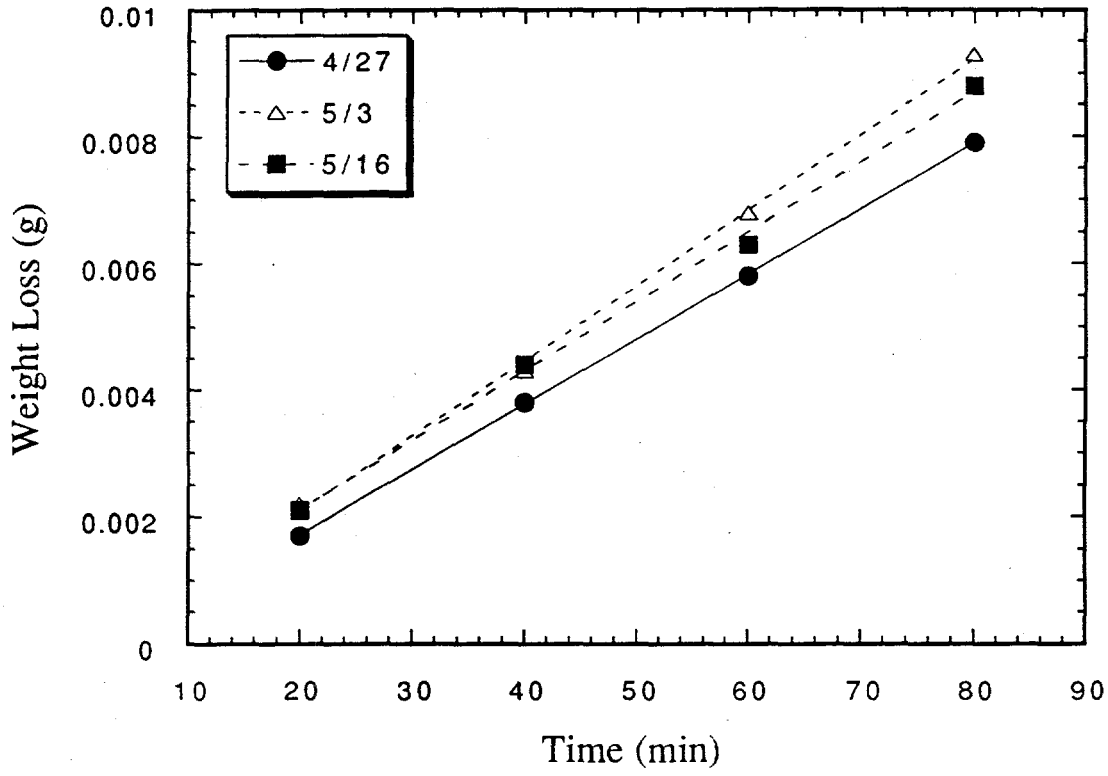

Figure IV.4- Weight loss versus time curves for CrMo steel on different days.

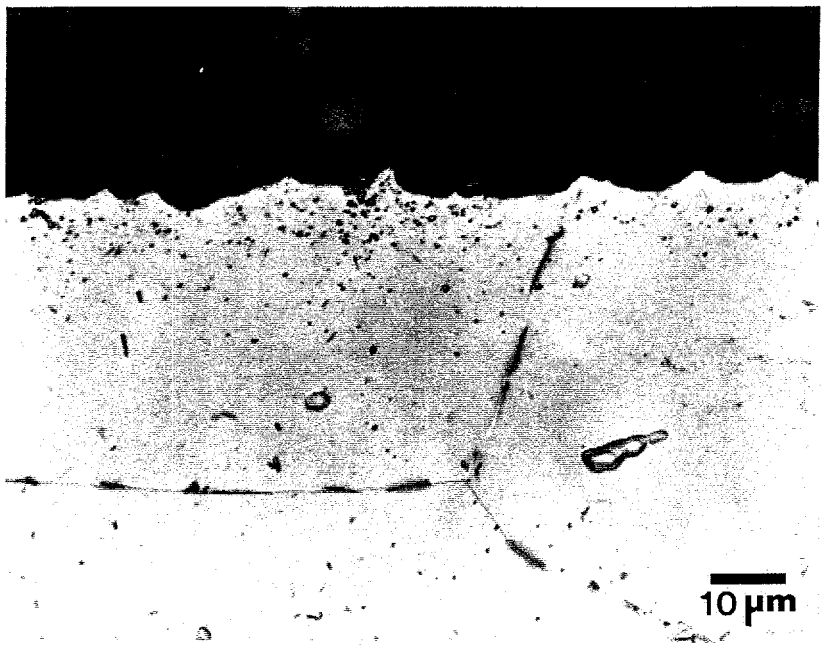

Figure IV.5- Ripple formation in the wrought FeAl alloy at 90° (1000x).

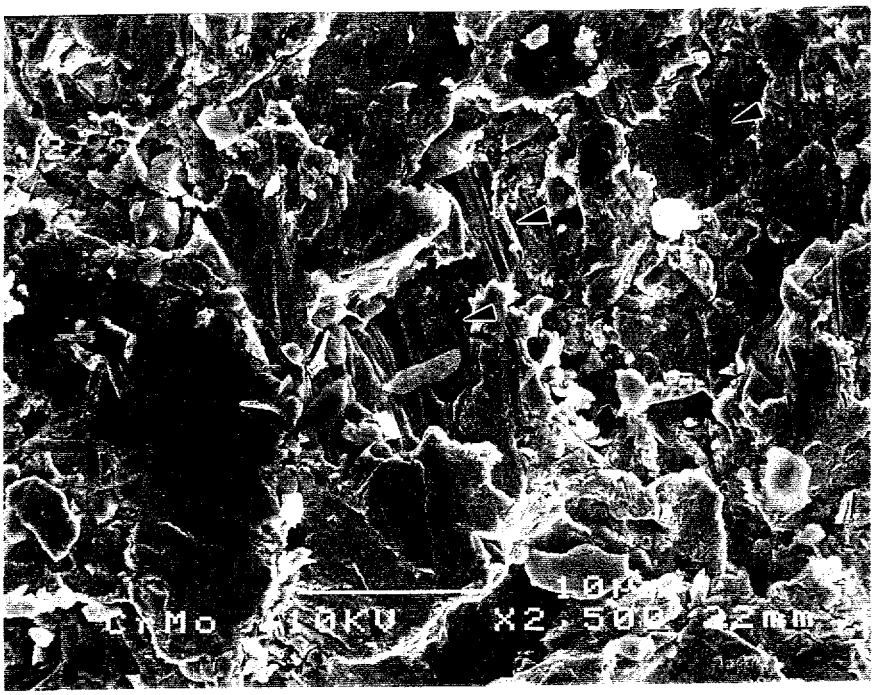

Figure IV.6- Erosion striations (arrows) due to ploughing in the CrMo steel at 30° (2500x).

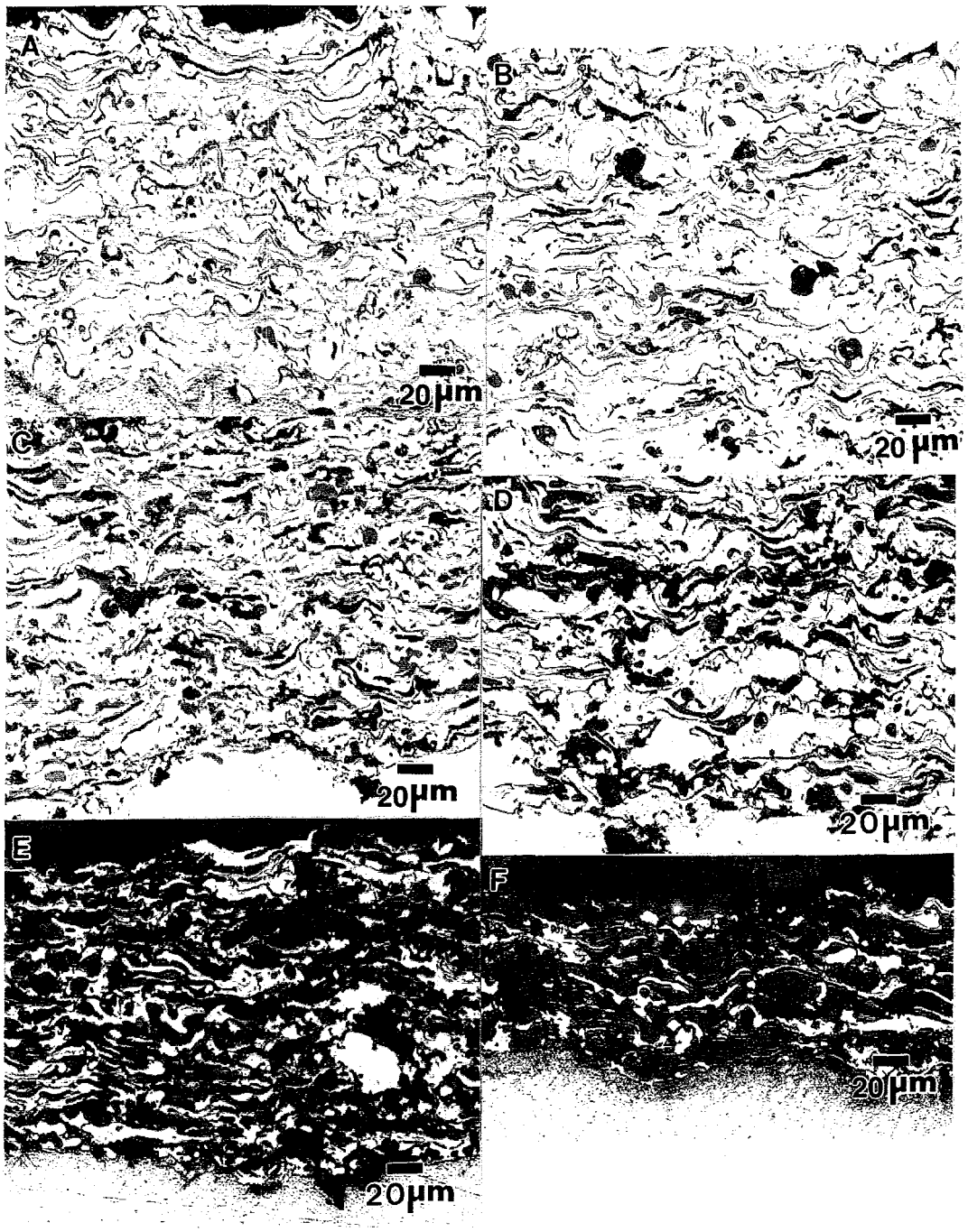

Figure IV.7-APS FeAl coating microstructures: a.0% Al_2O_3, b.10% Al_2O_3, c.20% Al_2O_3, d.40% Al_2O_3, e.60% Al_2O_3, and f.80% Al_2O_3 (250x).

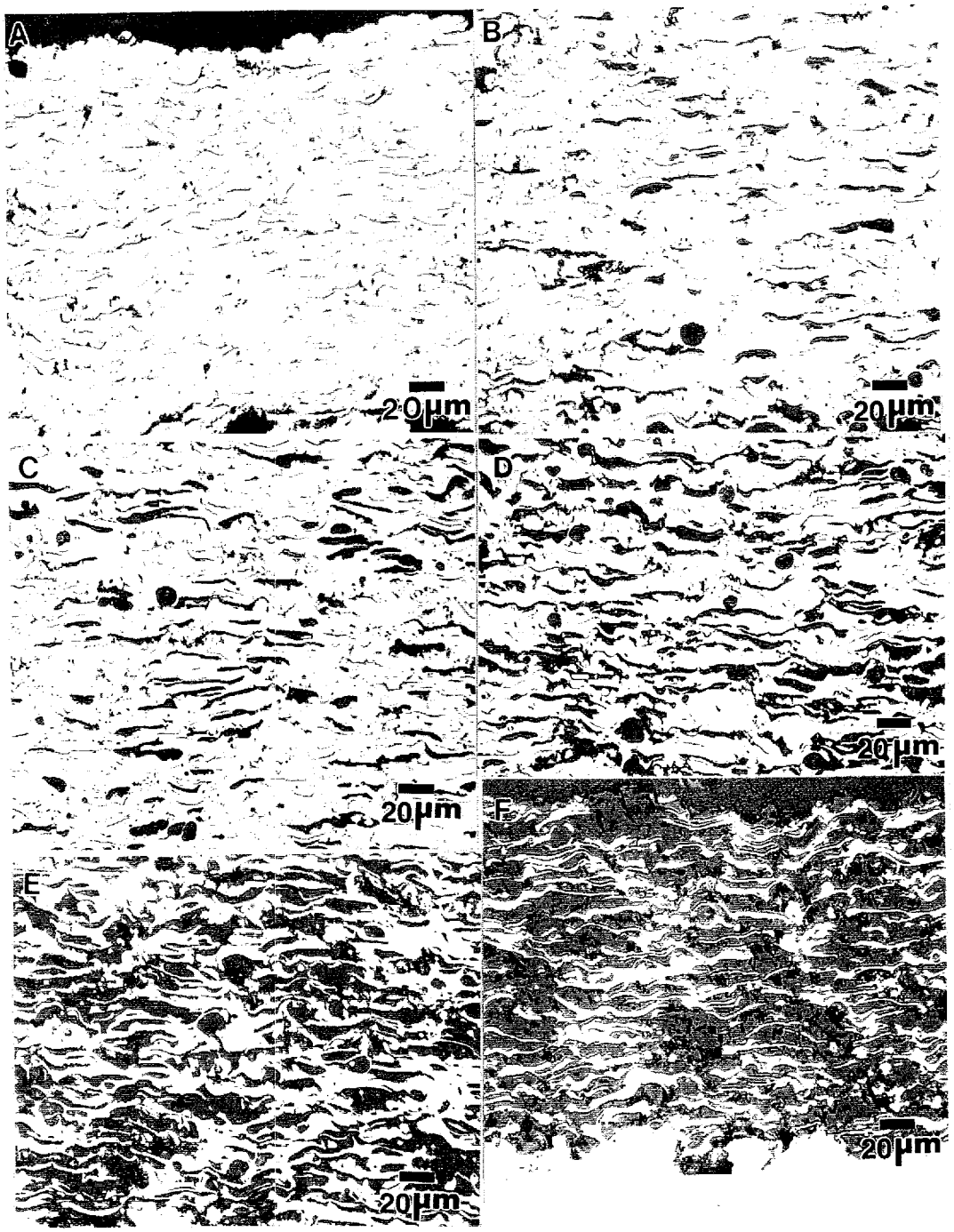

Figure IV.8- VPS FeAl (-25 μm) coating microstructures: a.0% Al_2O_3, b.10% Al_2O_3, c.20% Al_2O_3, d.40% Al_2O_3, e.60% Al_2O_3, and f.80% Al_2O_3 (250x).

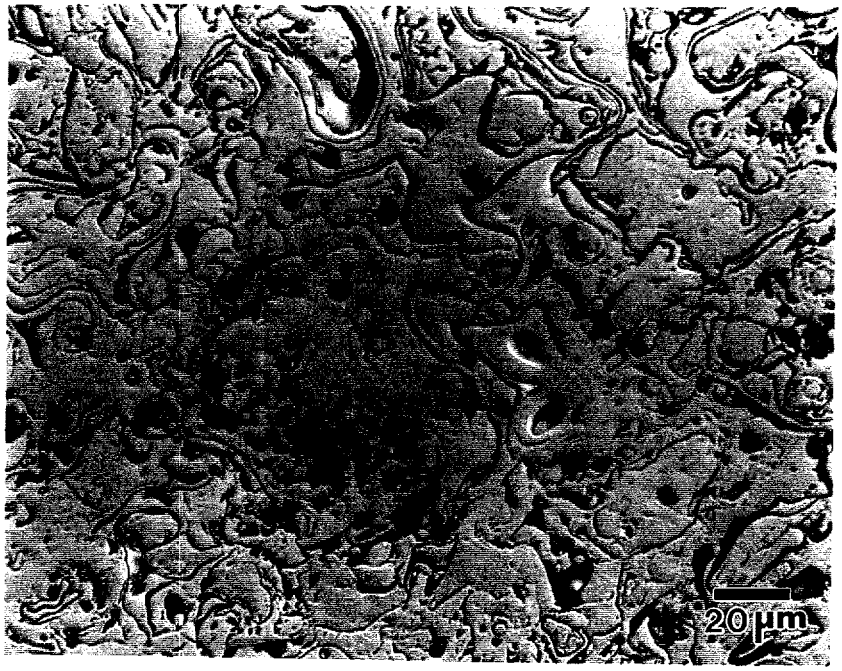

Figure IV.9- APS FeAl planar section (500x).

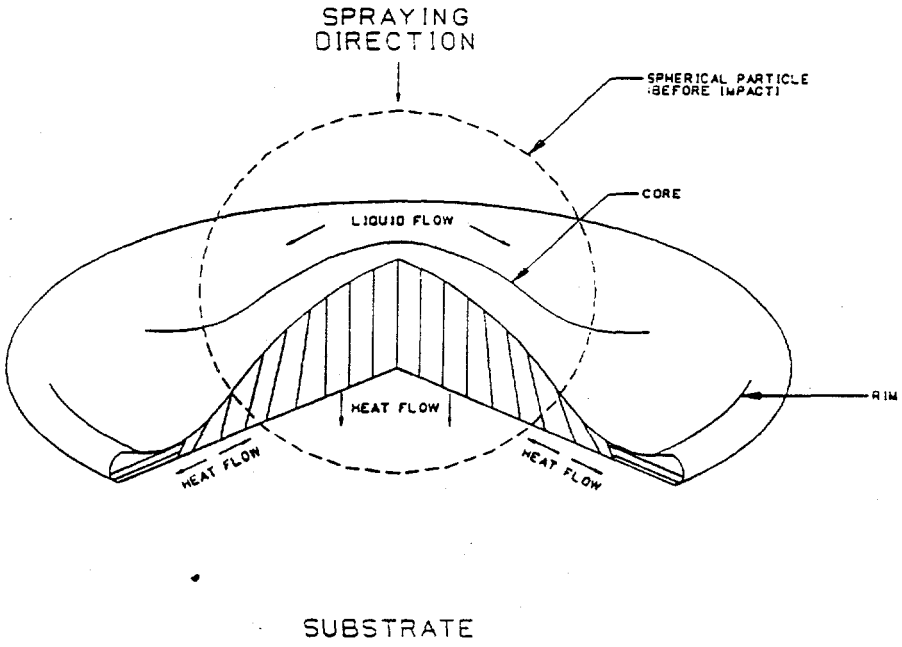

Figure IV.10- Directional cooing in splats leading to columnar grain formation (**40**).

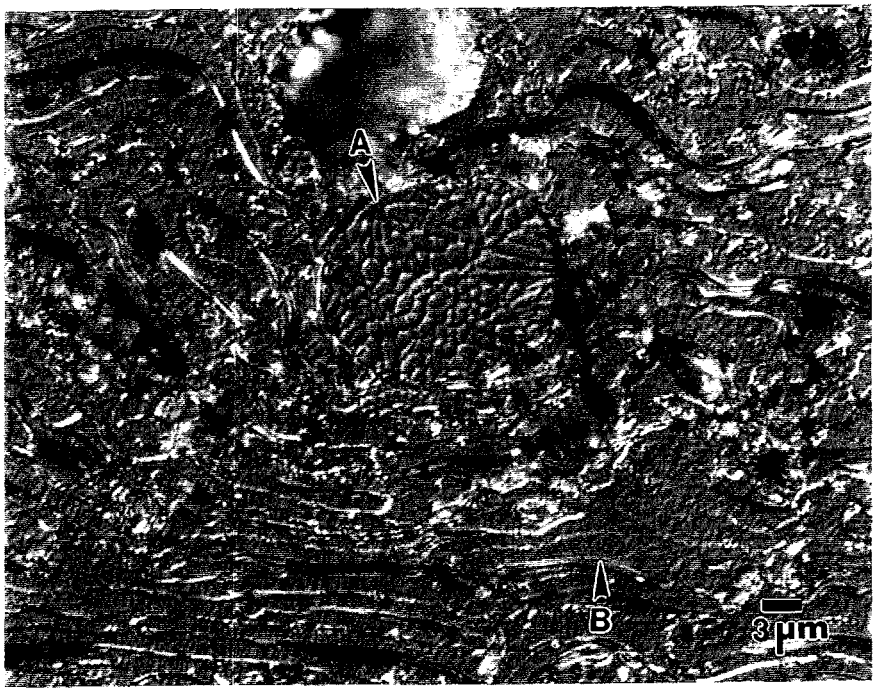

Figure IV.11- 100% FeAl -25 μm VPS coating, etched: a.unmelted particle, b. splat dendrites (1500x).

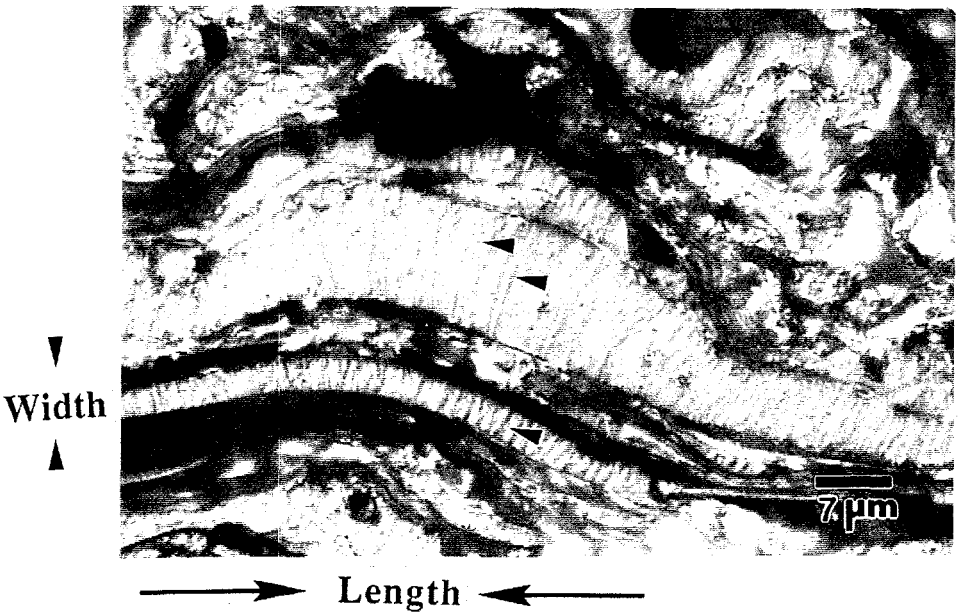

Figure IV.12- 90% FeAl - 10% Al_2O_3 +25µm VPS coating, etched: arrows indicate columnar structure (1600x). Note: the aspect ratio ofa typical splat, leading to long particles parallel to the substrate interface: L/W = 2.75"/0.25" = aspect ratio of 11.

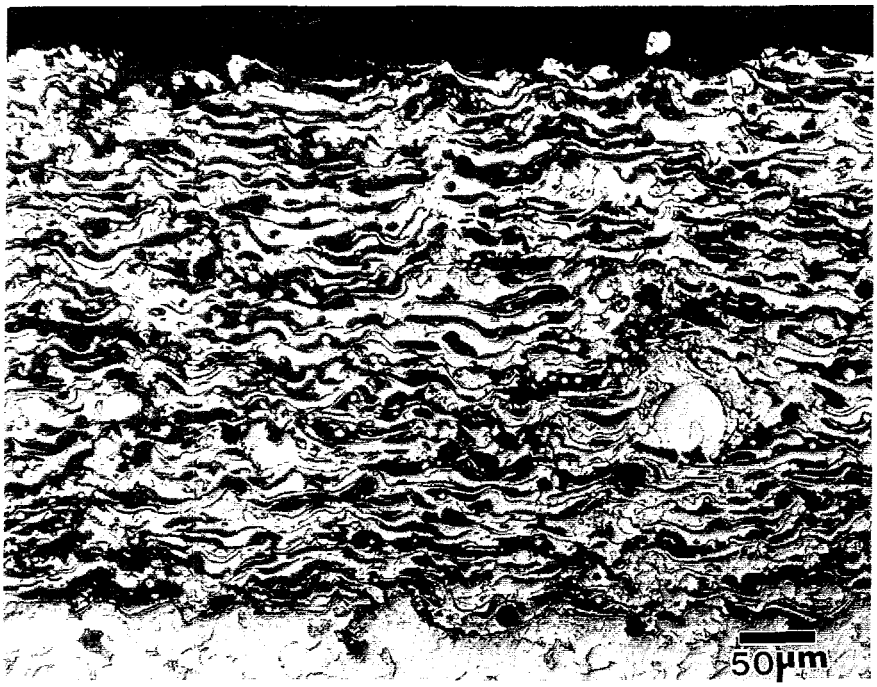

Figure IV.13- VPS FeAl coating heat treated @ 600°C for 96 hours (200x).

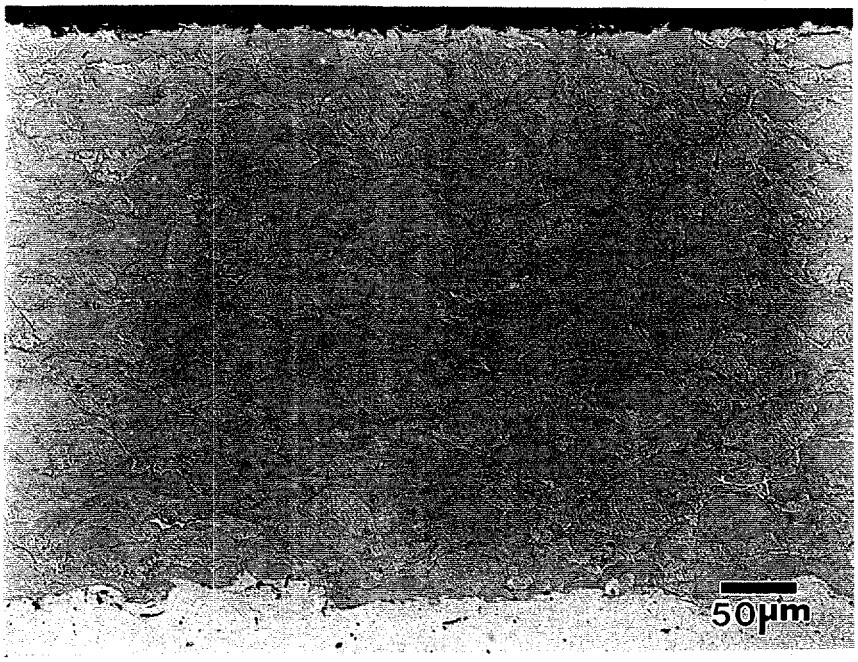

Figure IV.14- FeAl HVOF (+25 µm) coating (200x).

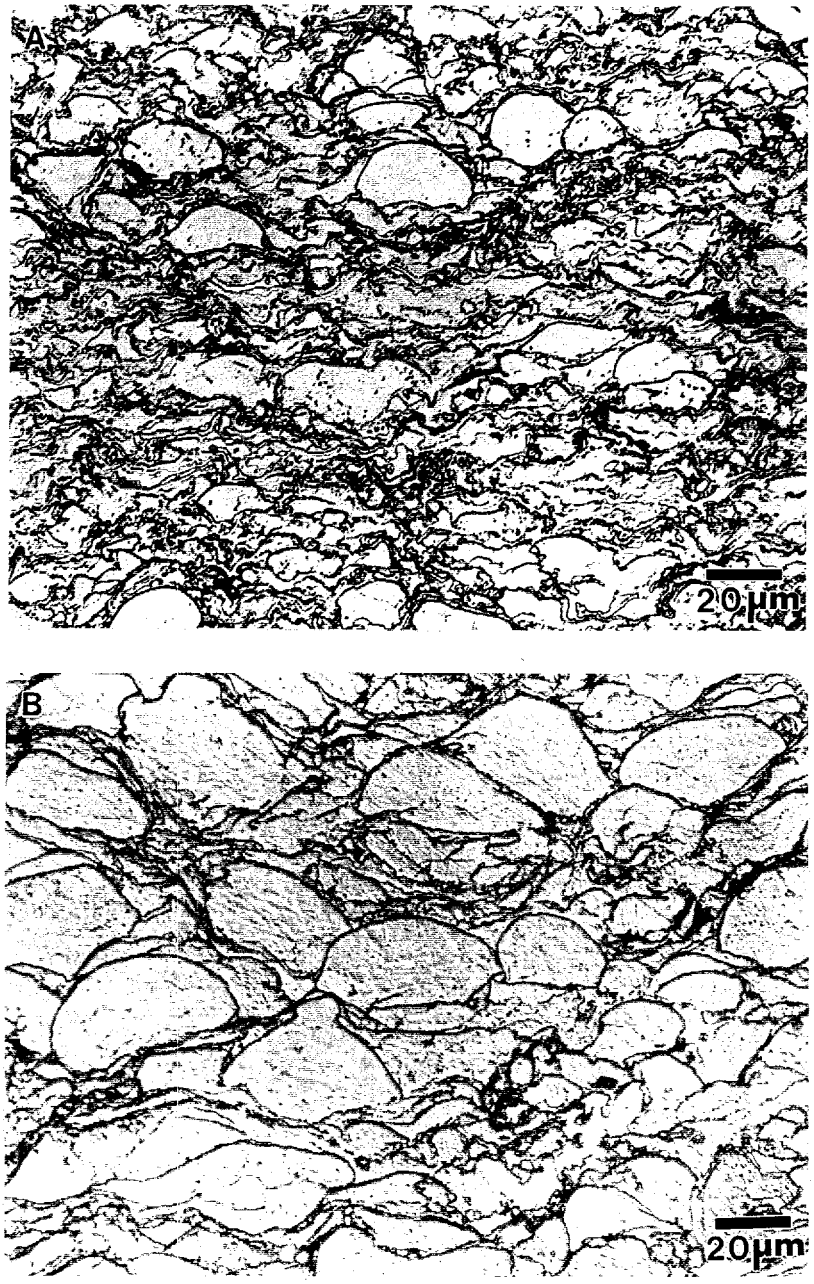

Figure IV.15- FeAl HVOF coating, etched: a.-25 µm, b.+25 µm (500x).

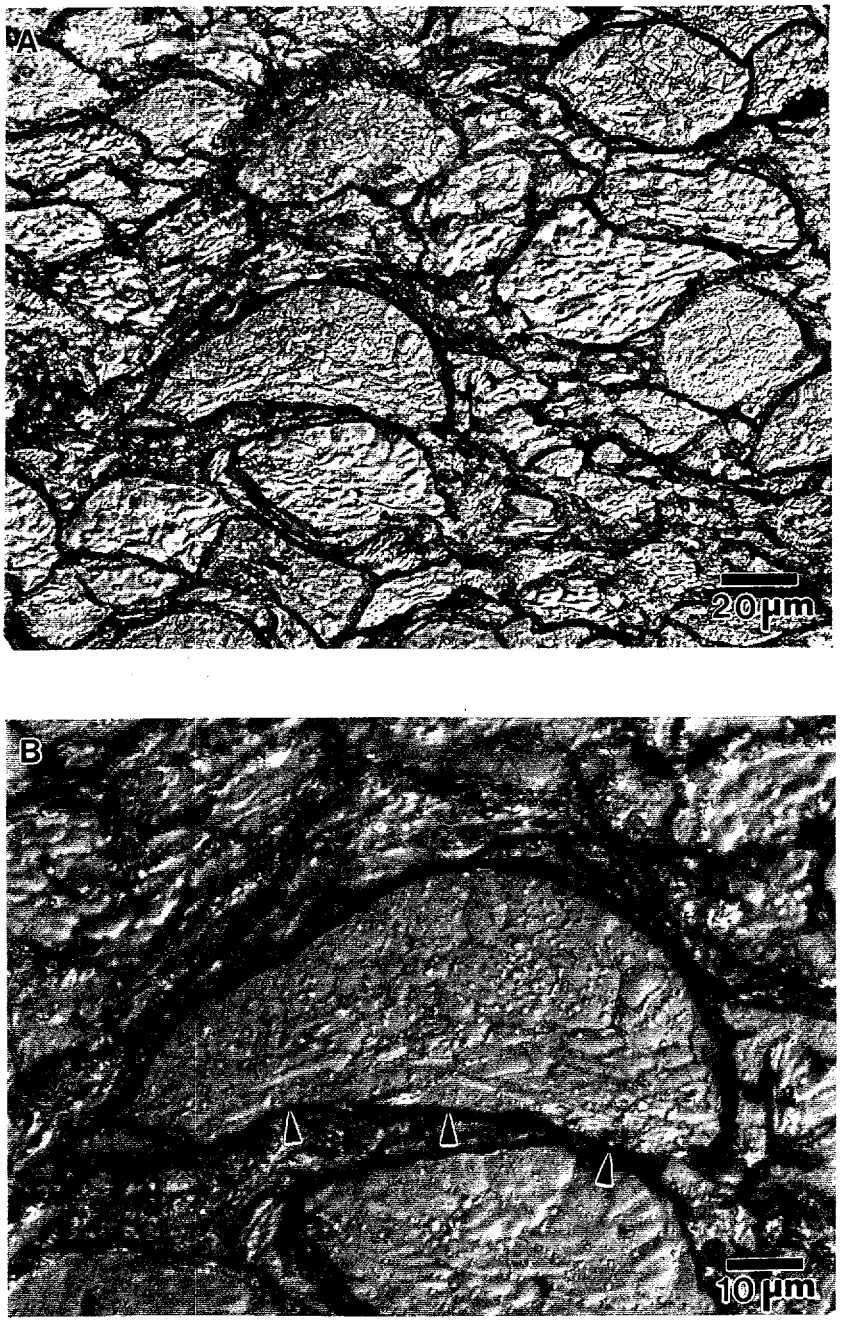

Figure IV.16- FeAl HVOF +25µm coating, etched: a.500x, b.1500x(arrows indicate deformation at base of unmelted particle).

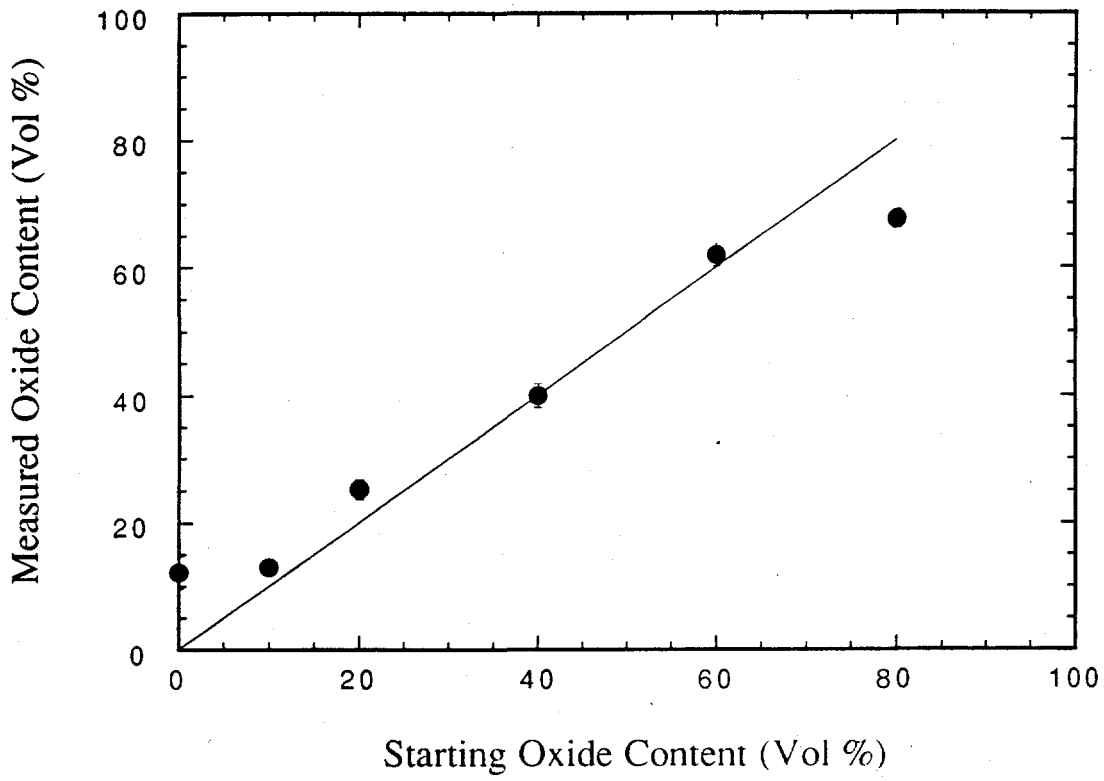

Figure IV.17- Measured oxide content versus the starting Al_2O_3 content in the VPS,+25μm Fe/Al alloy coatings.

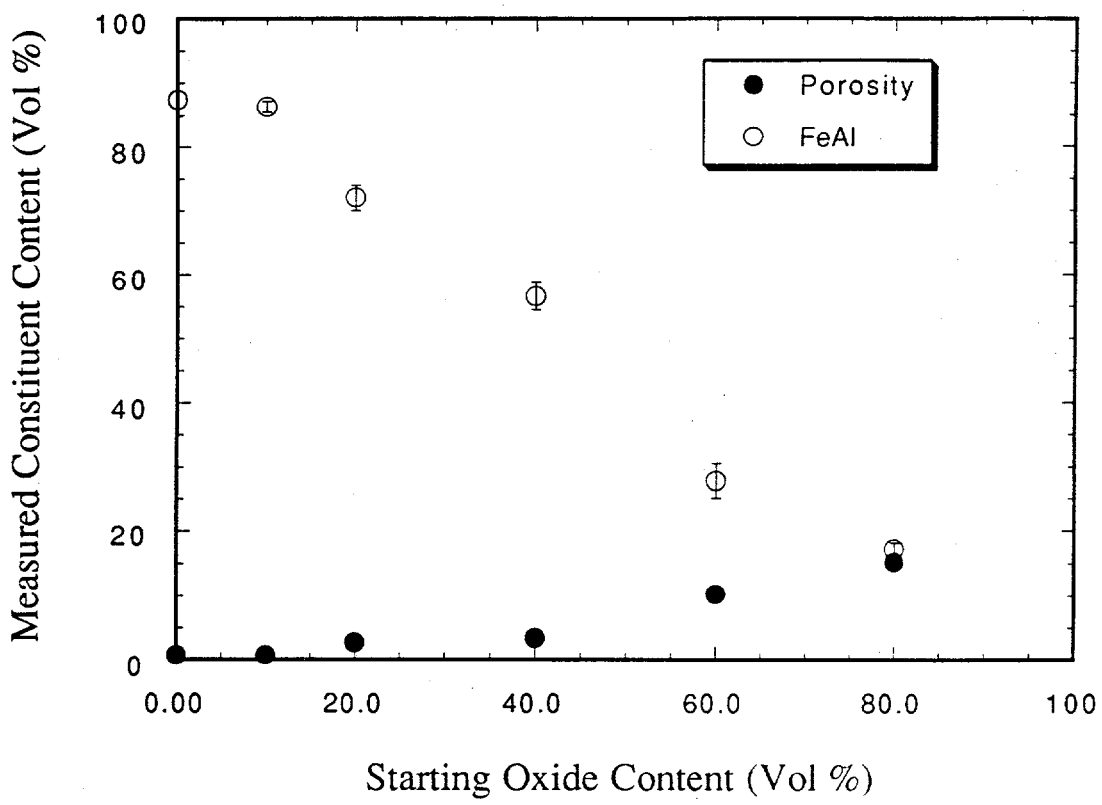

Figure IV.18- Measured porosity and FeAl content versus the starting Al_2O_3 content in the VPS, +25μm Fe/Al alloy coatings.

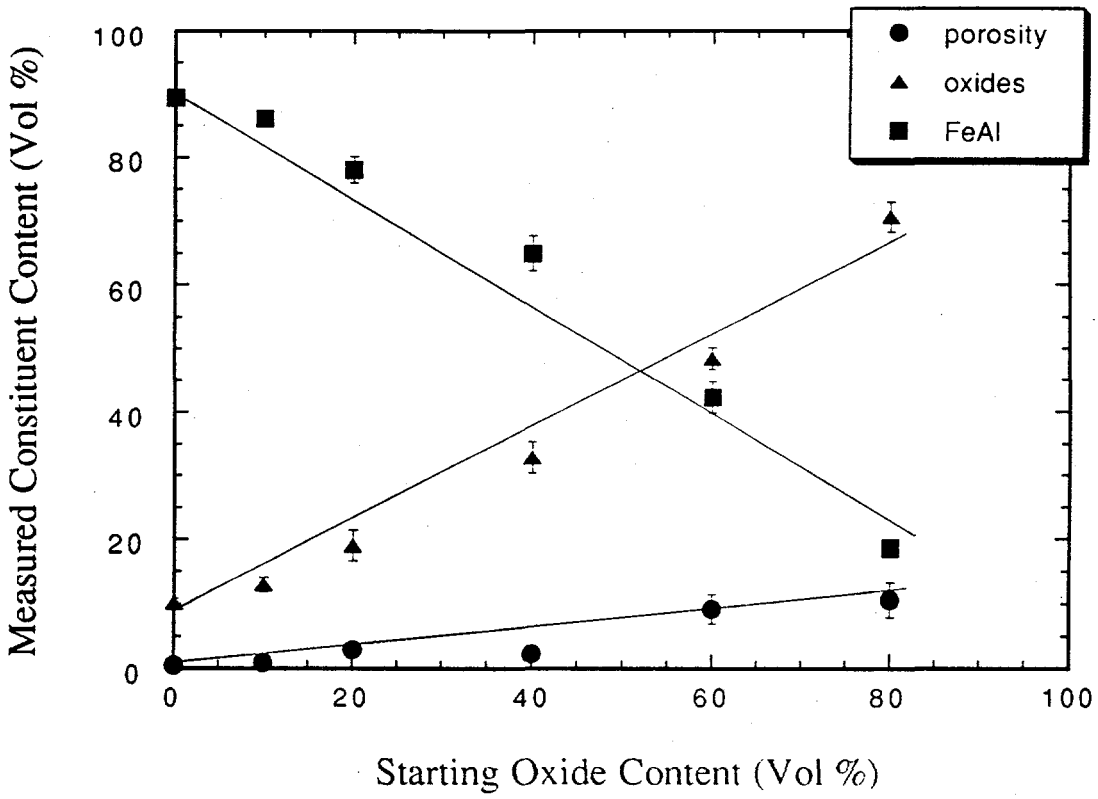

Figure IV.19- Measured constituent content versus the starting Al_2O_3 content in the VPS, -25μm Fe/Al alloy coatings.

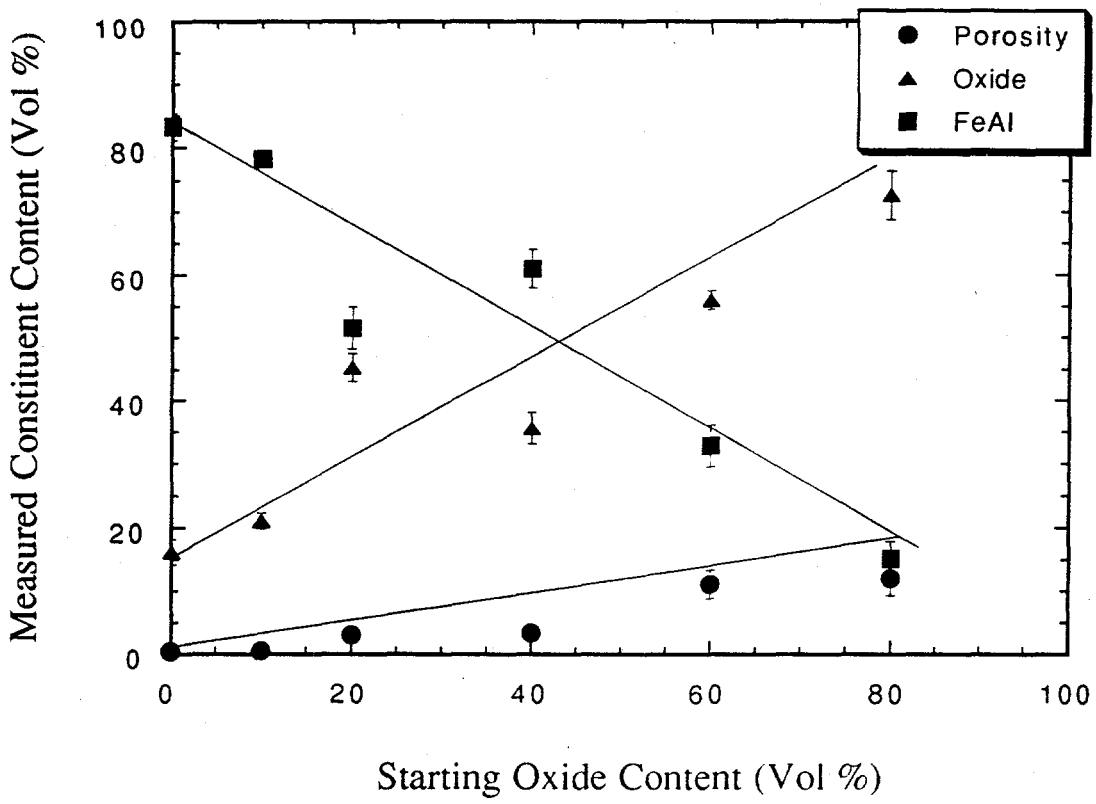

Figure IV.20- Measured constituent content versus the starting Al_2O_3 content in the APS Fe/Al alloy coatings.

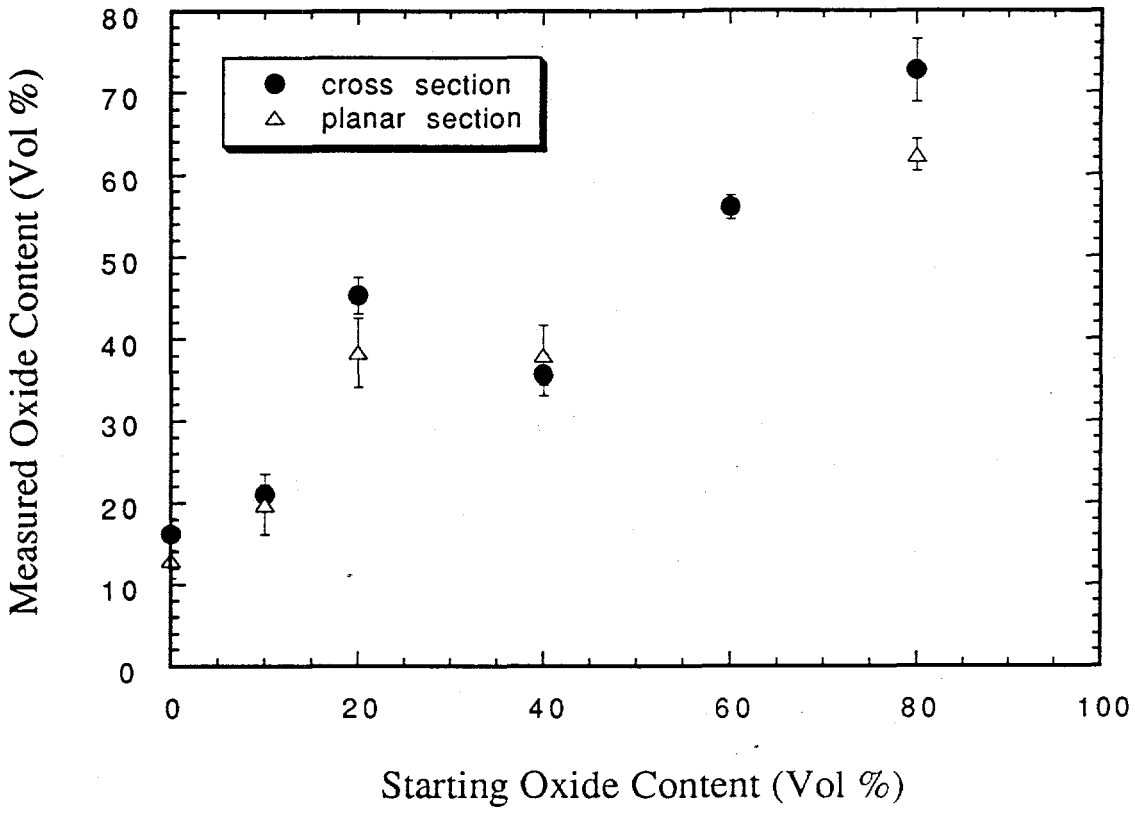

Figure IV.21- Measured oxide content versus starting Al_2O_3 content for both planar and cross sections in the APS Fe/Al alloy coatings.

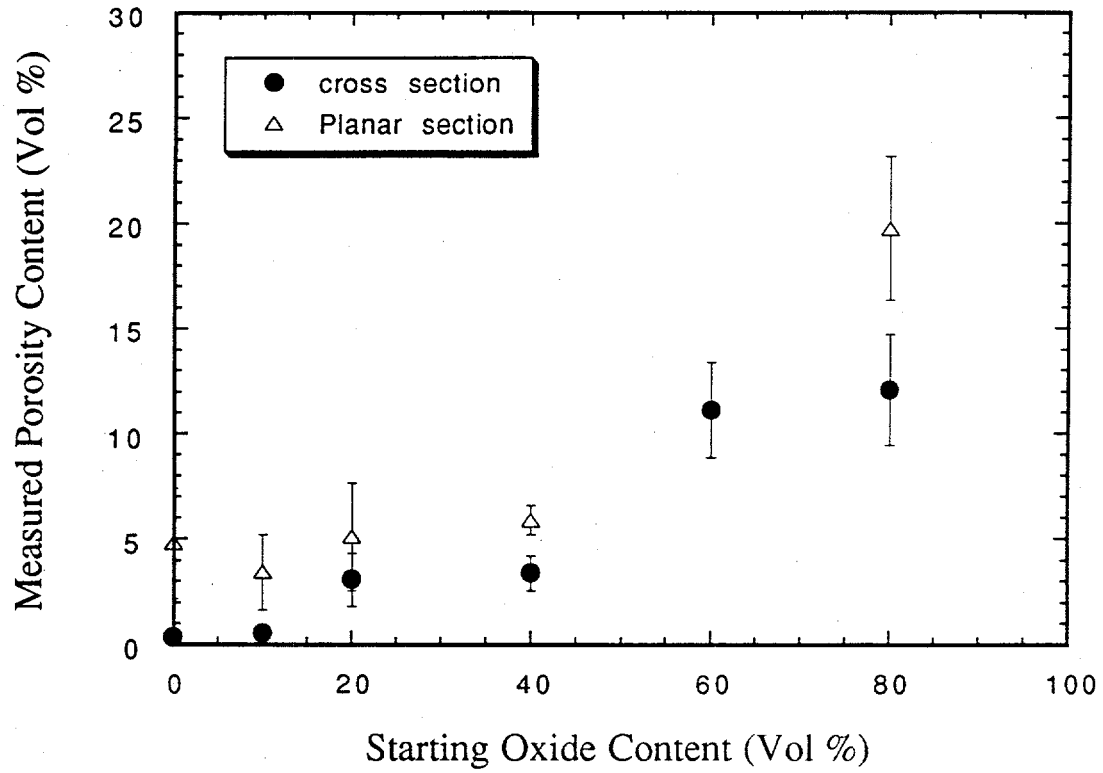

Figure IV.22- Measured porosity versus starting Al_2O_3 content for both planar and cross sections in the APS Fe/Al alloy coatings.

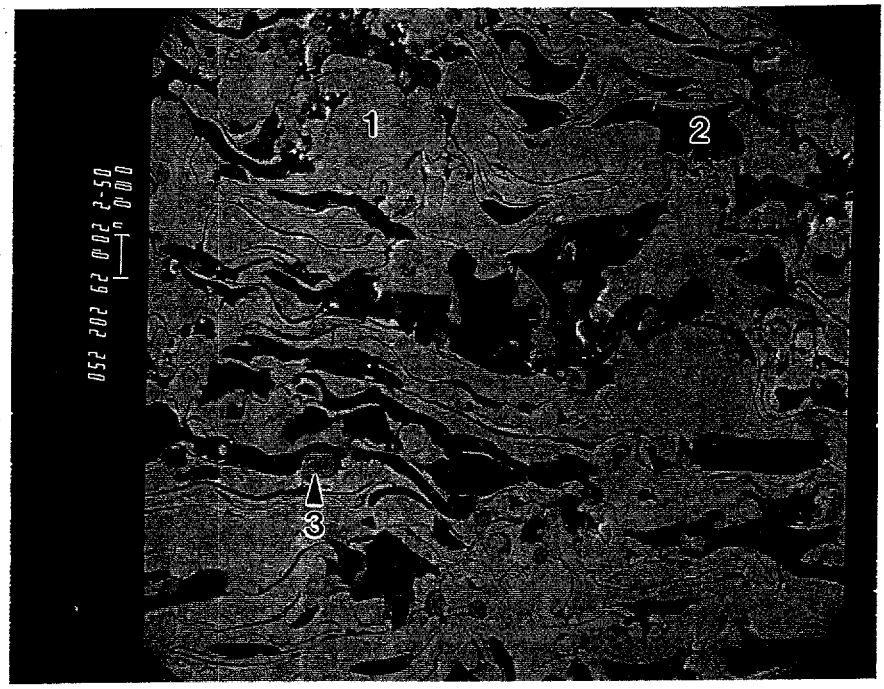

Figure IV.23- 40% Al_2O_3- 60% Fe/Al alloy APS coating, BSE (500x).

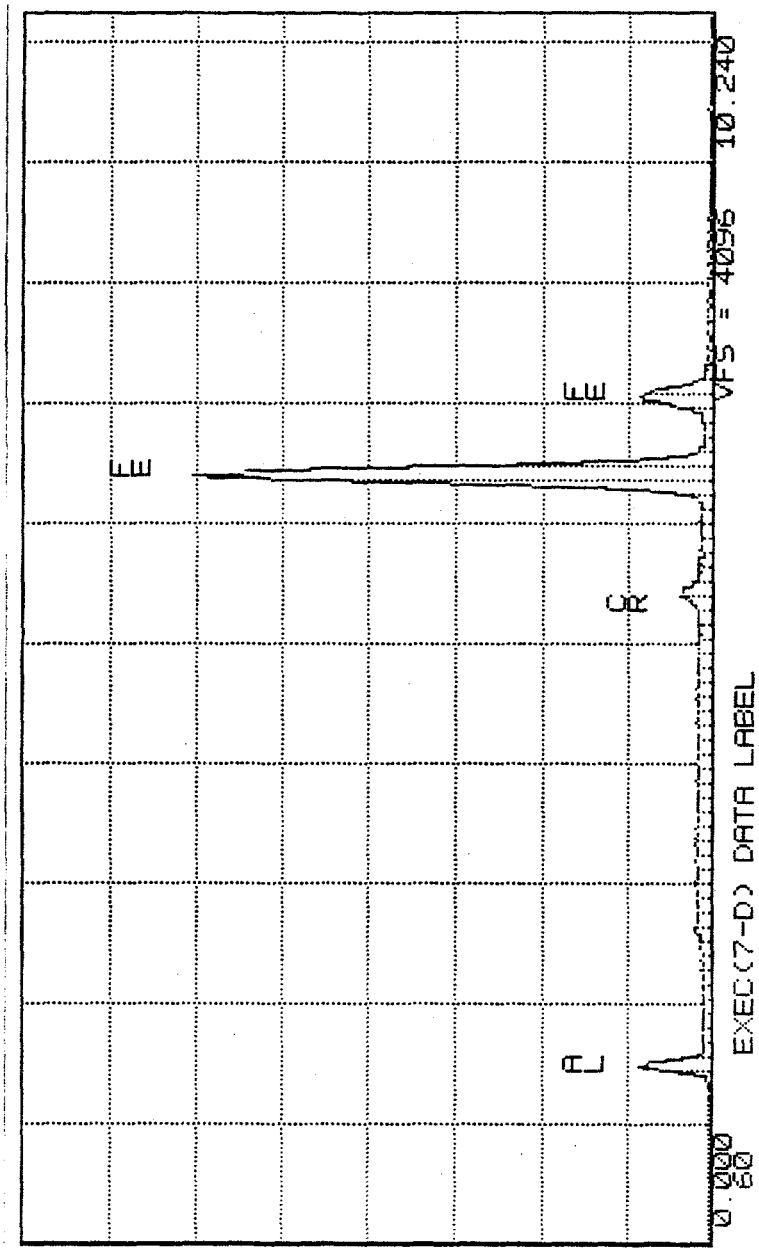

Figure IV.24 EDS spectra for phase 1 (white) in figure IV.23.

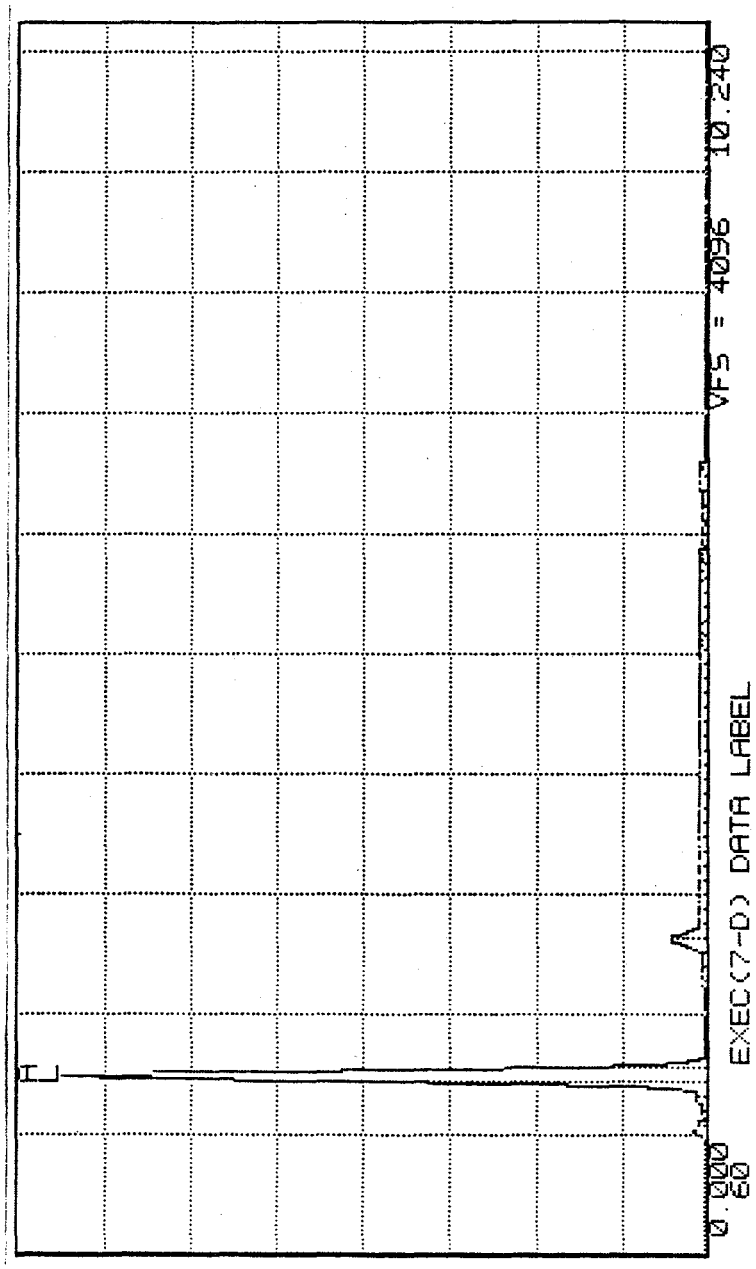

Figure IV.25 EDS spectra for phase 2 (dark gray) in figure IV.23.

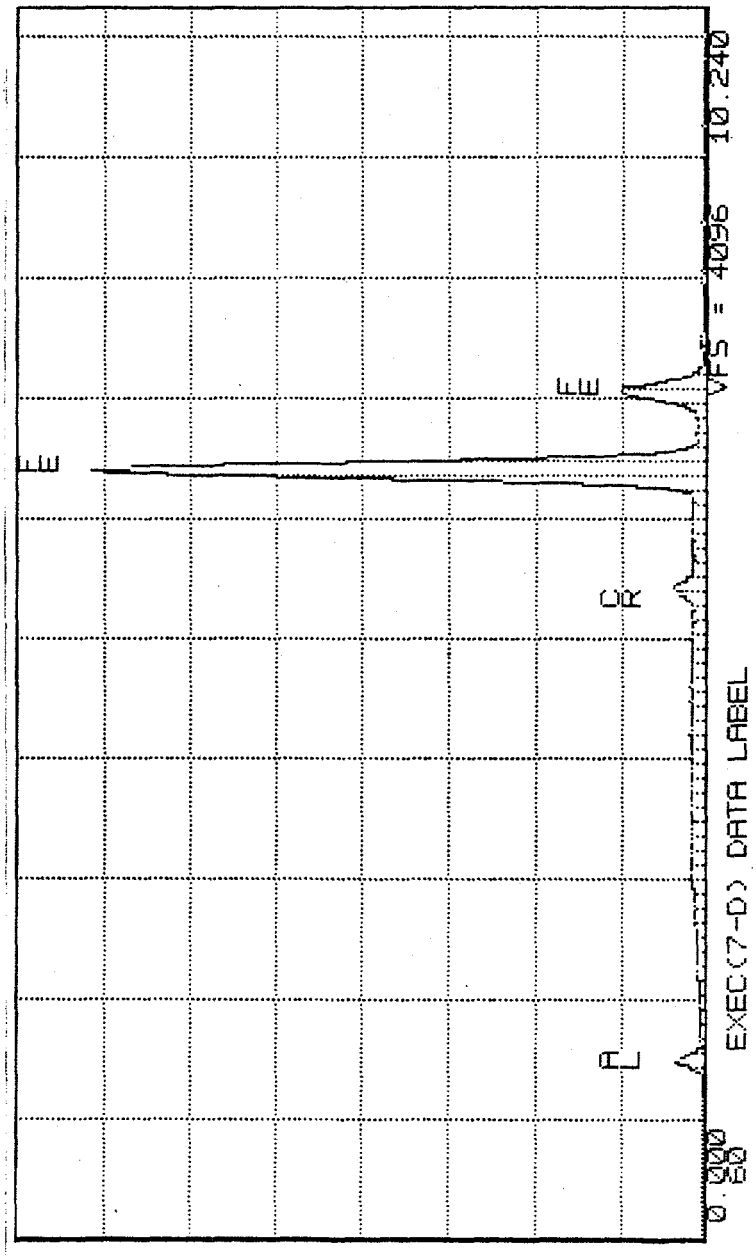

Figure IV.26 EDS spectra for phase 3 (light gray) in figure IV.23.

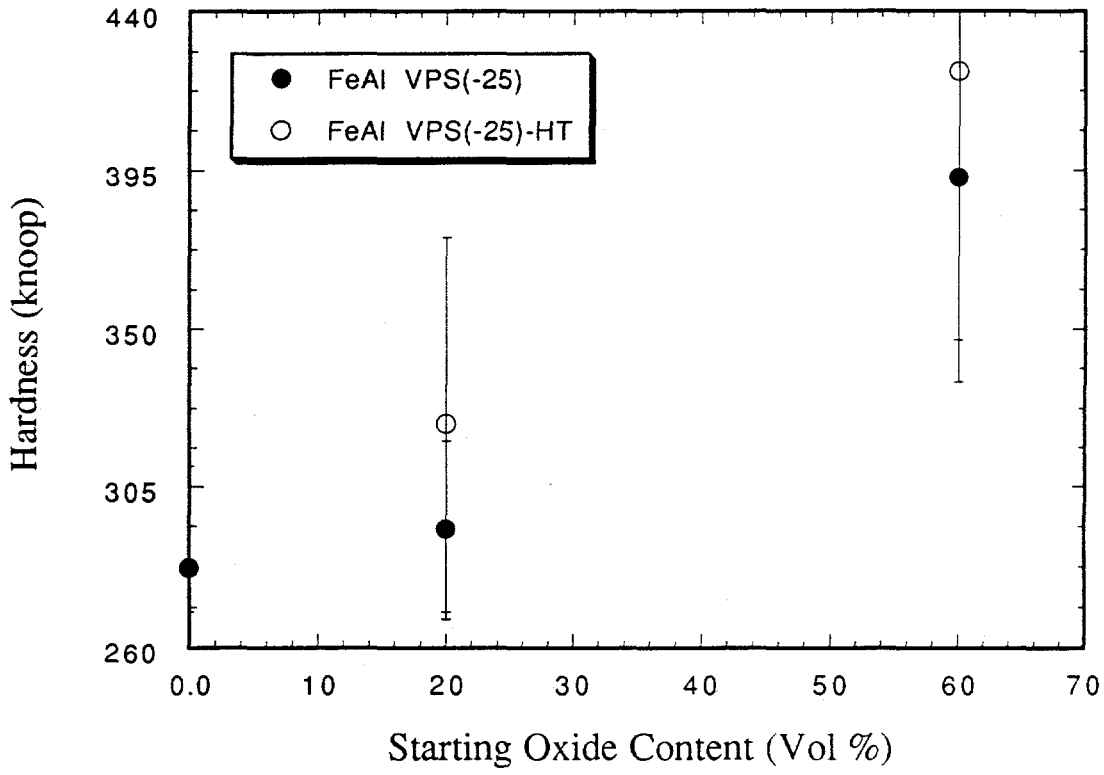

Figure IV.27- Knoop hardness readings for plasma FeAl-Al_2O_3 -25μm VPS cermets before and after heat treatment @ 600°C for 96 hours (note: the 0% alumina samples have the same hardness values before and after heat treatment).

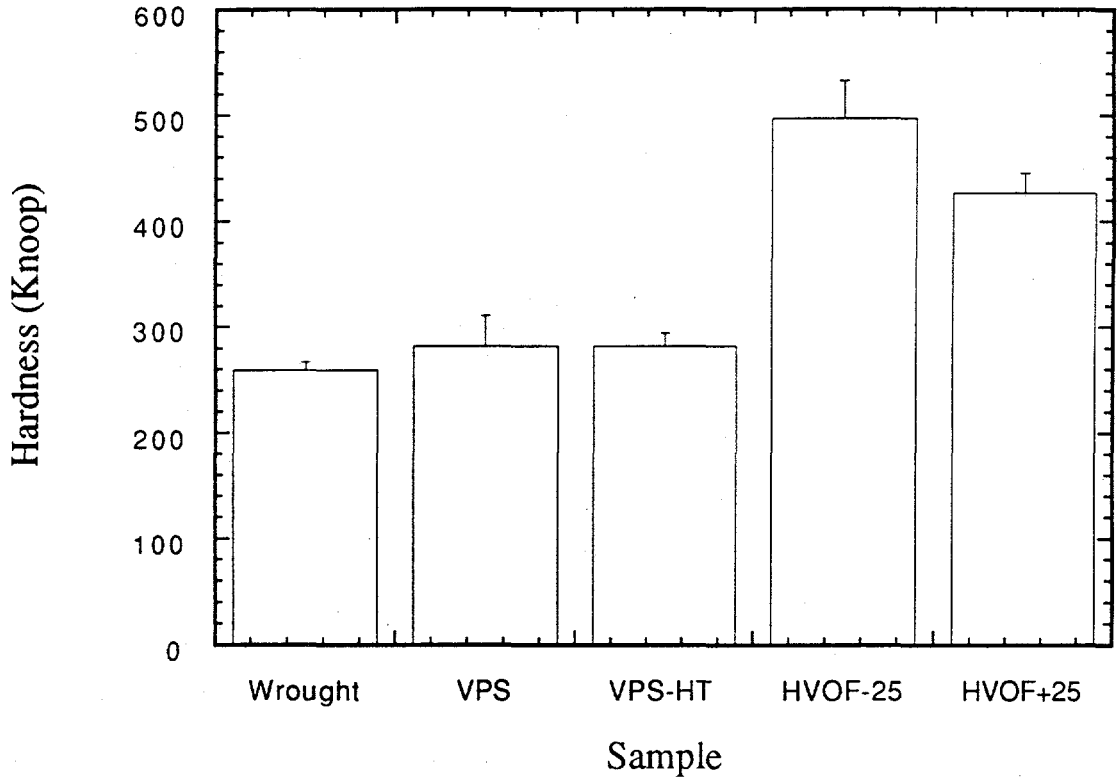

Figure IV.28- Knoop Hardness values for various FeAl materials (the lines at the top of each bar represent the standard deviation of each value).

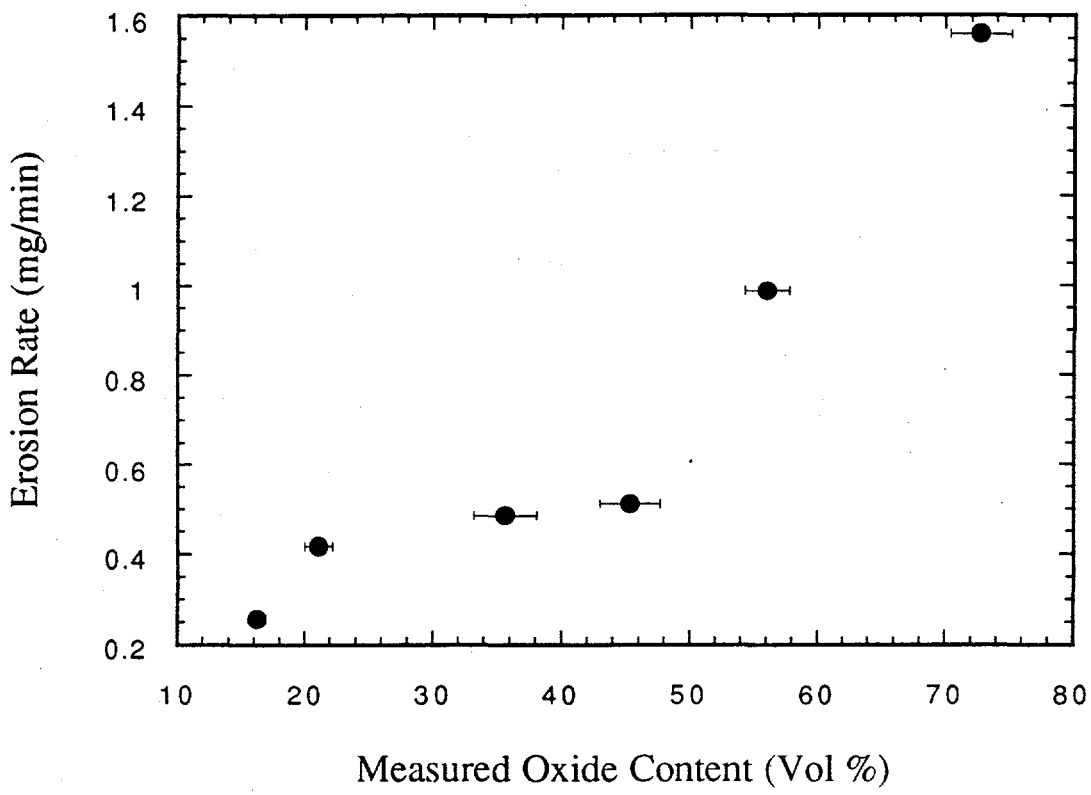

Figure IV.29 Erosion rate versus measured oxide content for the APS FeAl alloy coatings (90°).

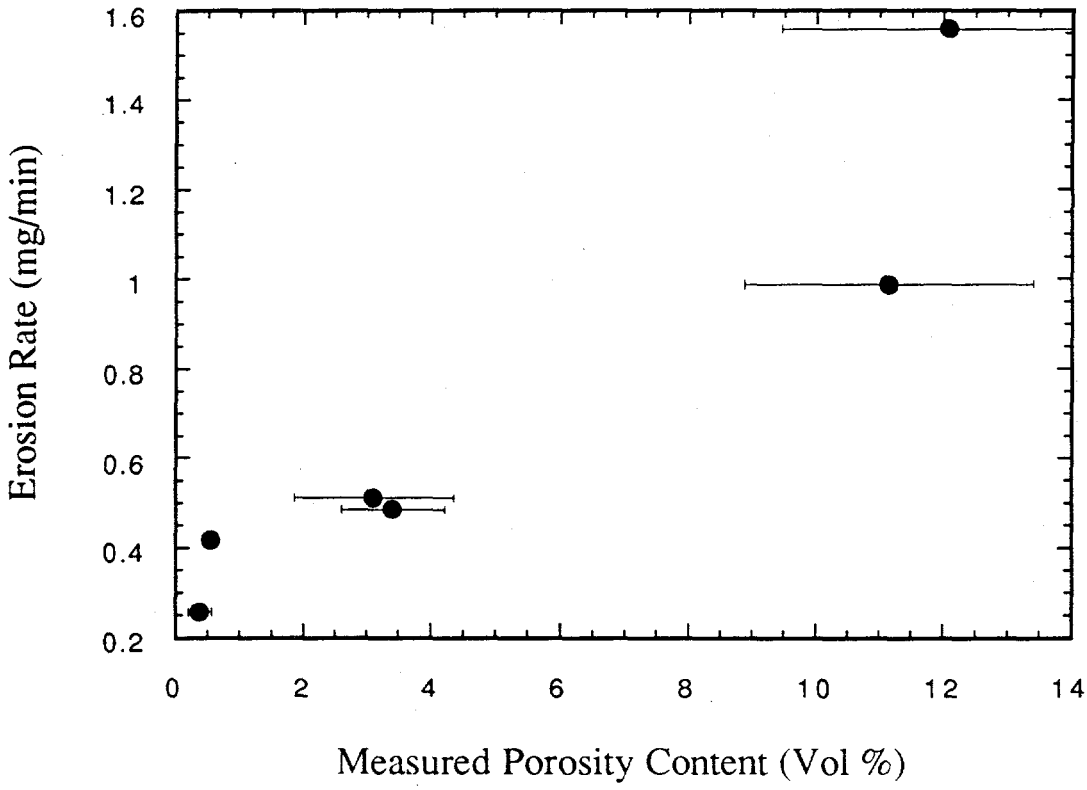

Figure IV.30- Erosion rate versus measured porosity for for the APS FeAl alloy coatings (90°).

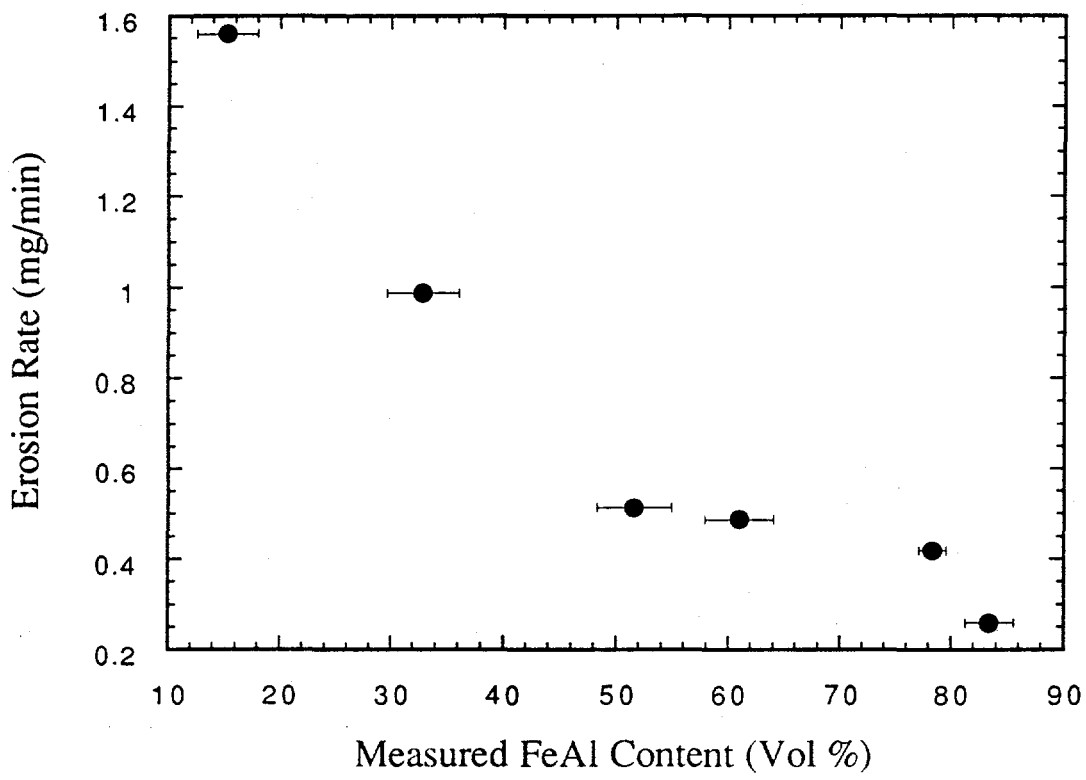

Figure IV.31- Erosion rate versus measured FeAl content for for the APS FeAl alloy coatings (90°).

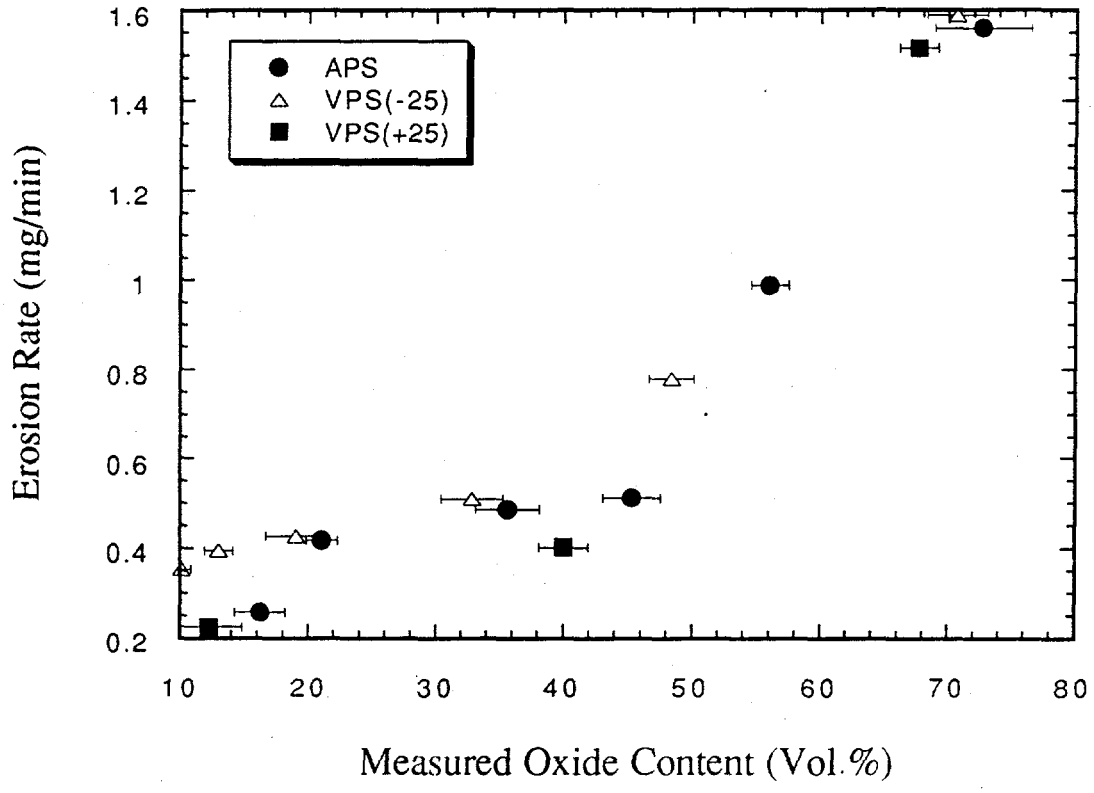

Figure IV.32- Erosion rate versus measured oxide content for all of the plasma FeAl alloy coatings (90°).

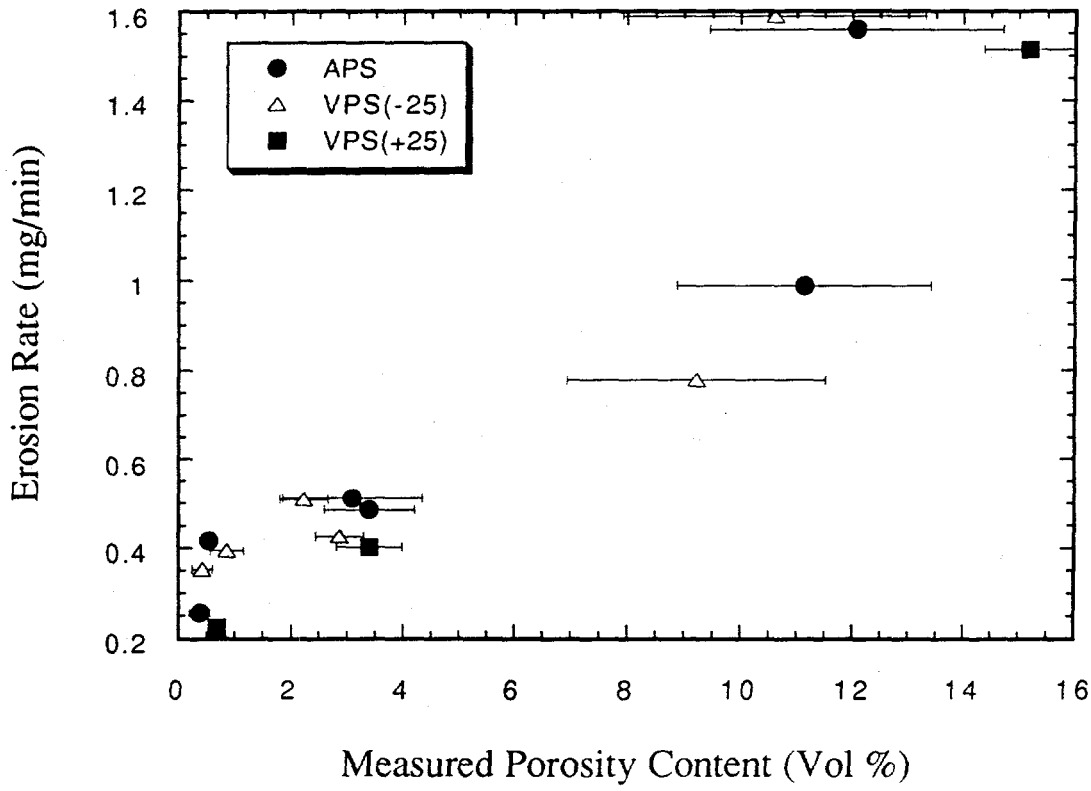

Figure IV.33- Erosion rate versus measured porosity content for all of the plasma FeAl alloy coatings (90°).

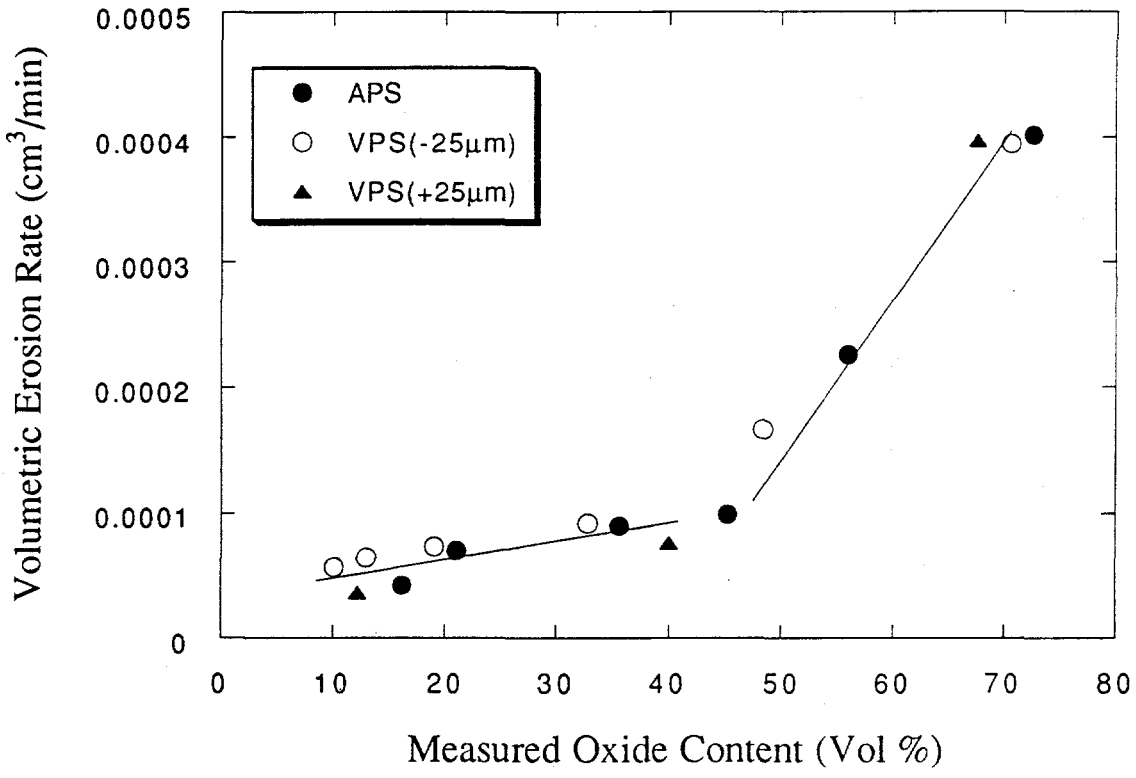

Figure IV.34 Volumetric erosion rate versus measured oxide content for all of the plasma Fe/Al alloy coatings (90°).

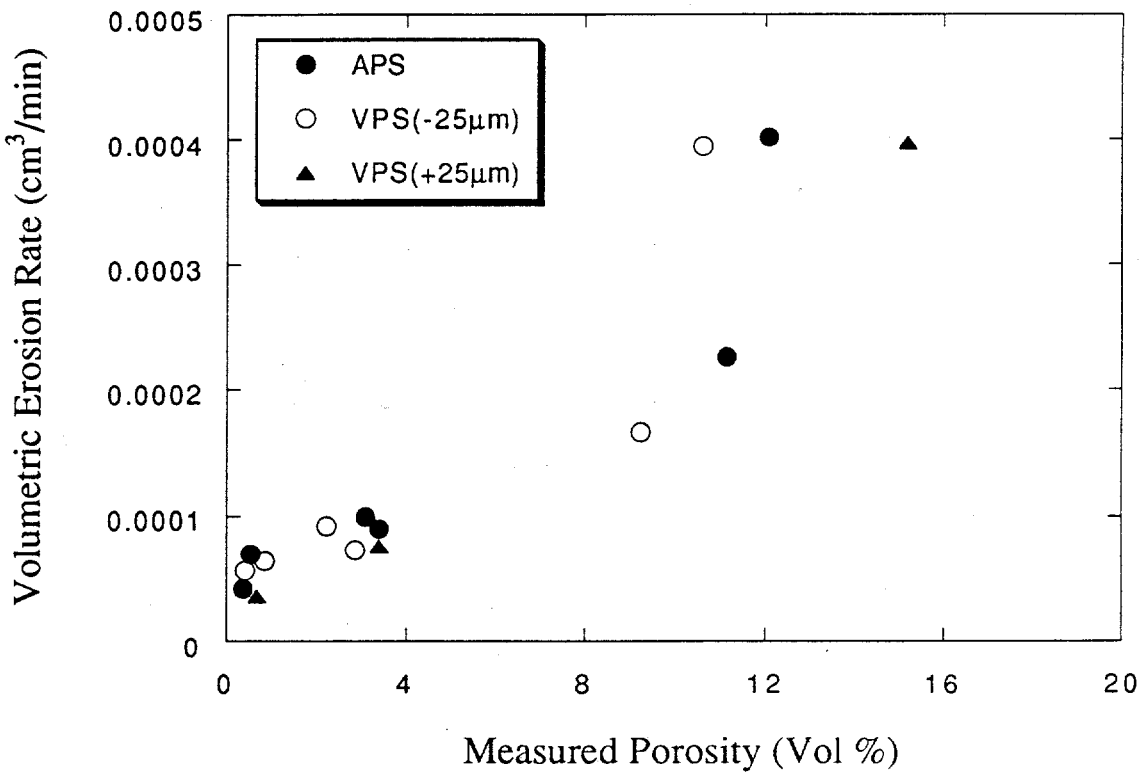

Figure IV.35- Volumetric erosion rate versus measured porosity for all of the plasma Fe/Al alloy coatings (90°).

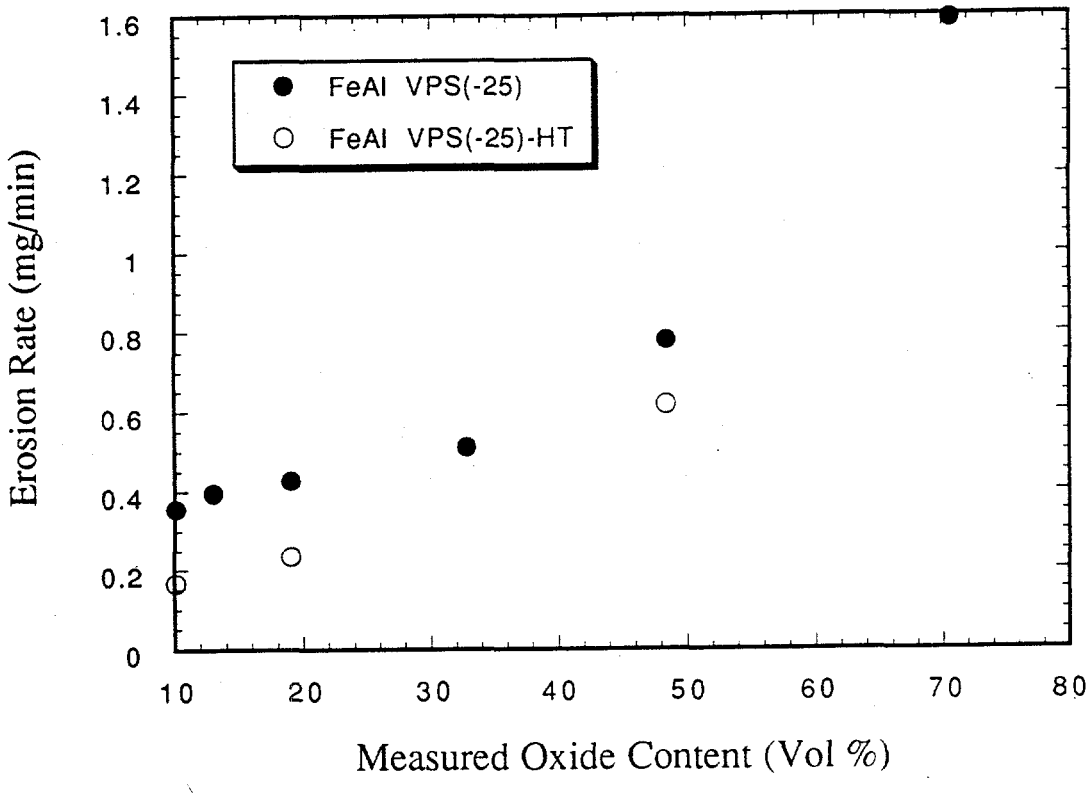

Figure IV.36- Erosion rate versus measured oxide content for VPS, -25μm plasma coatings before and after heat treatment @ 600°C for 96 hours (90°).

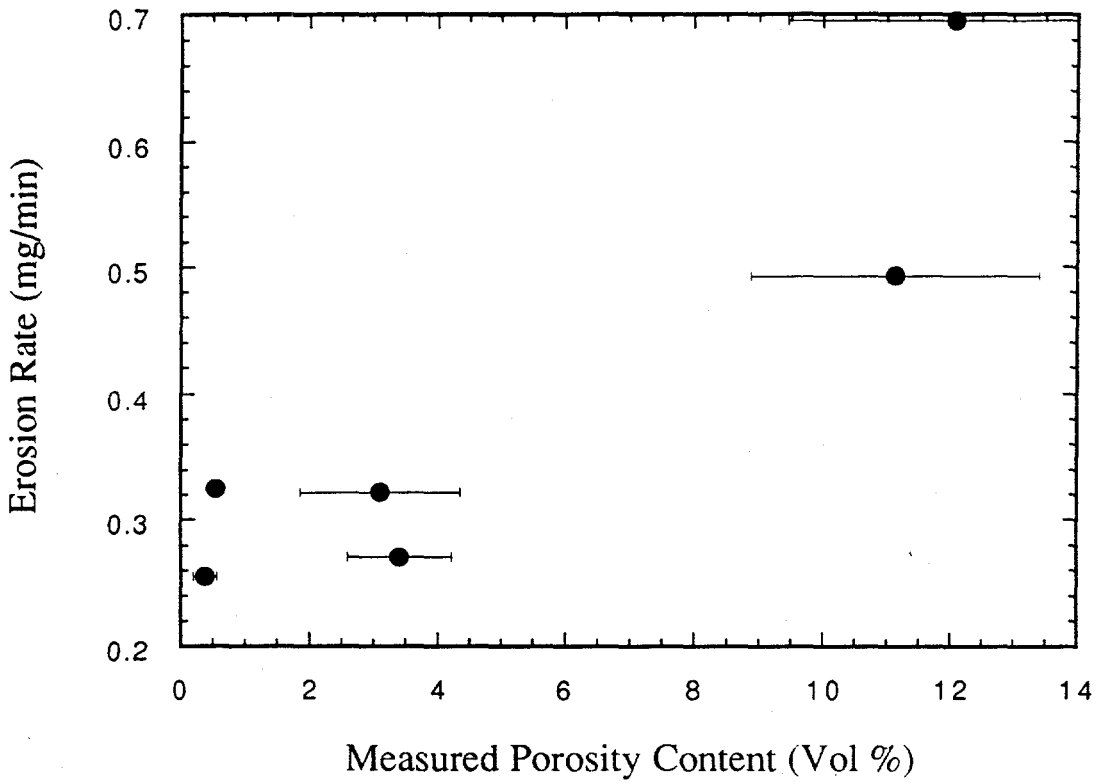

Figure IV.37- Erosion rate versus measured porosity for APS FeAl alloy coatings (30°).

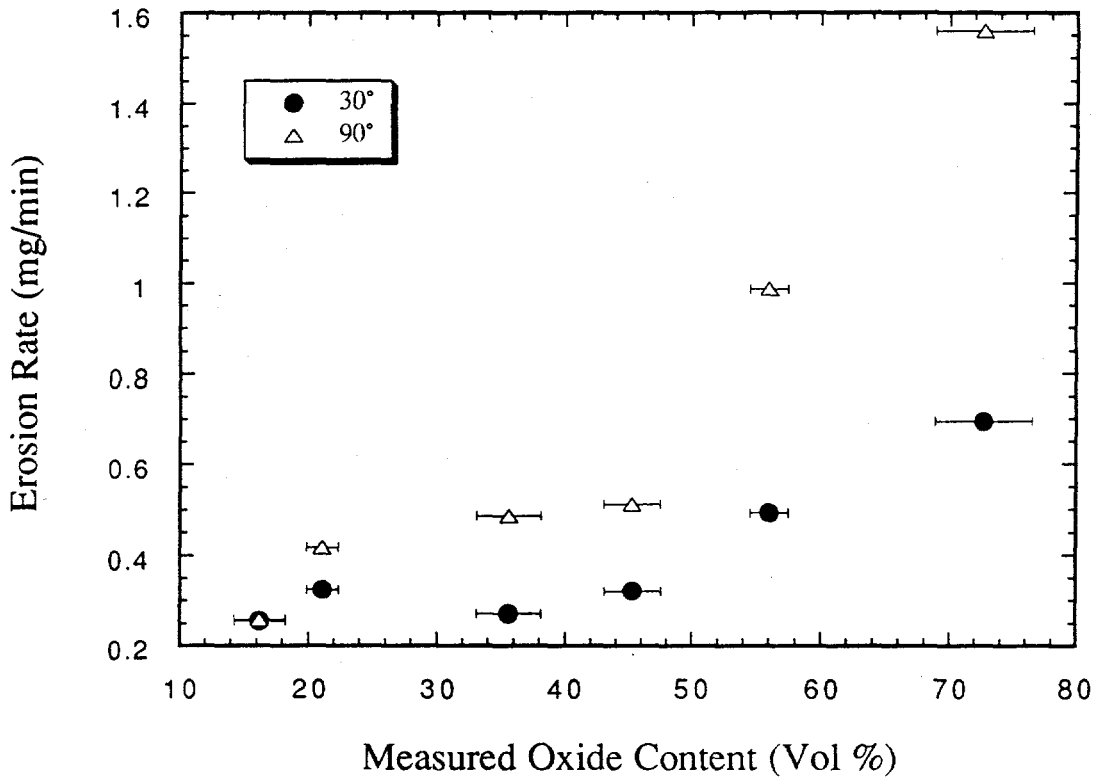

Figure IV.38- Erosion rate versus measured oxide content for APS FeAl alloy coatings (30° & 90°).

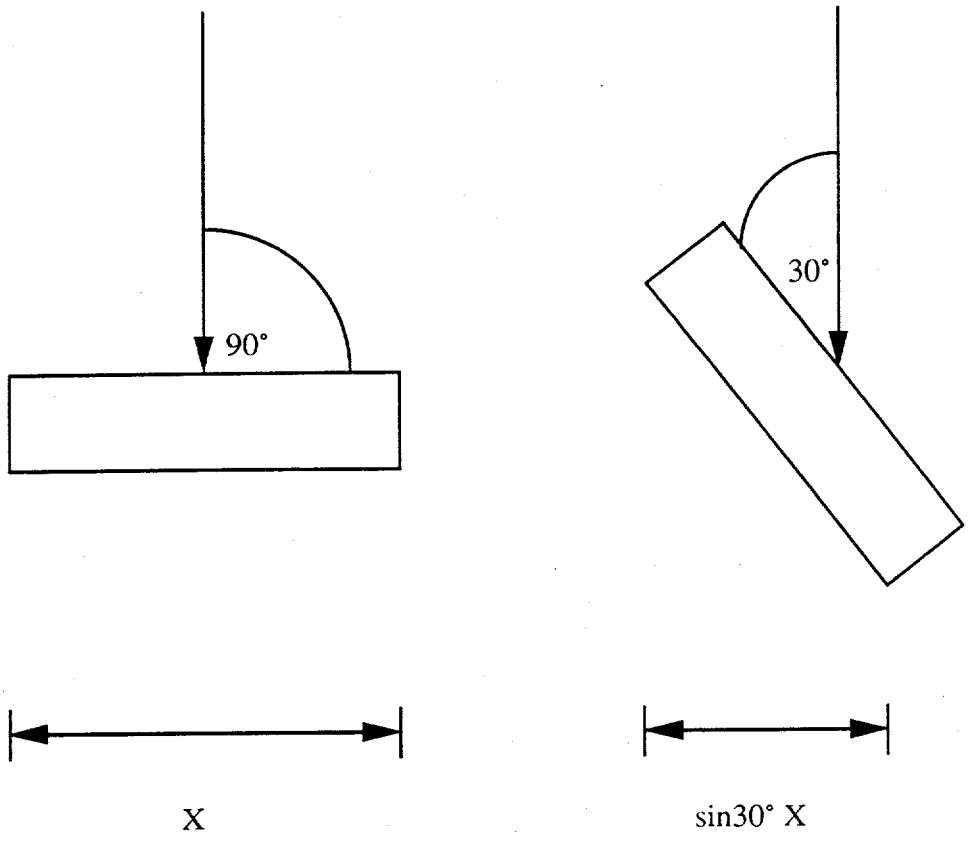

Figure IV.39- difference in exposed area at 30° and 90° impact angles.

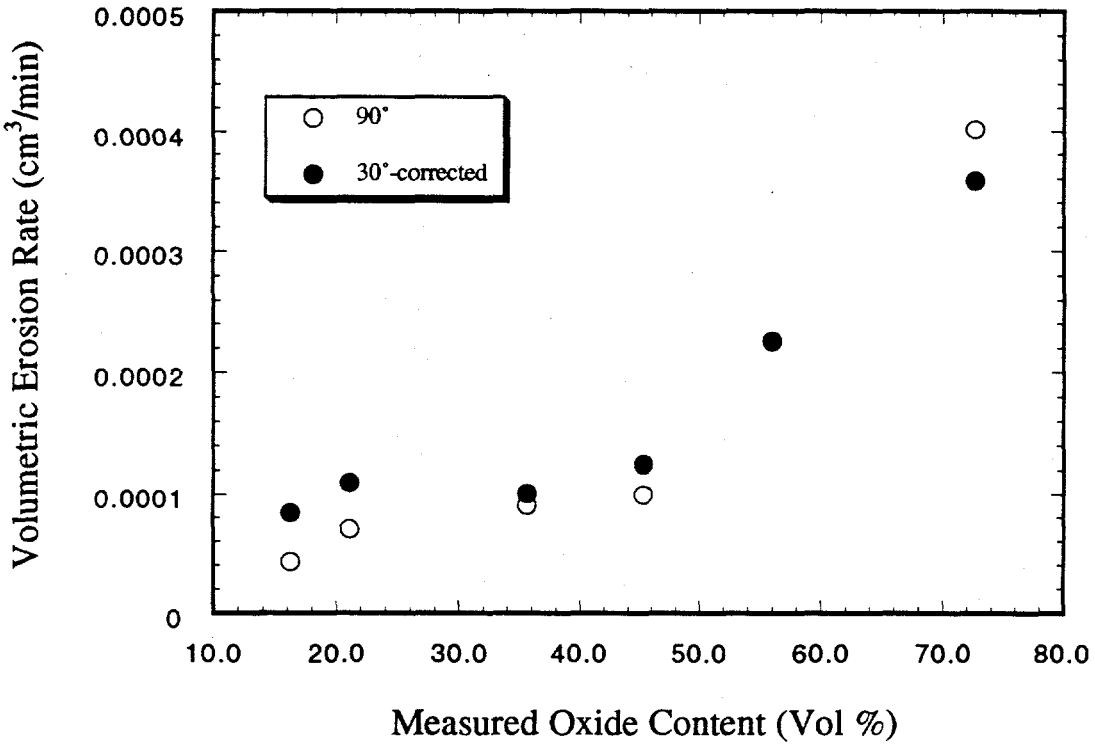

Figure IV.40- Volumetric erosion rate versus measured oxide content for APS FeAl alloy coatings with corrected 30° data (30° and 90°).

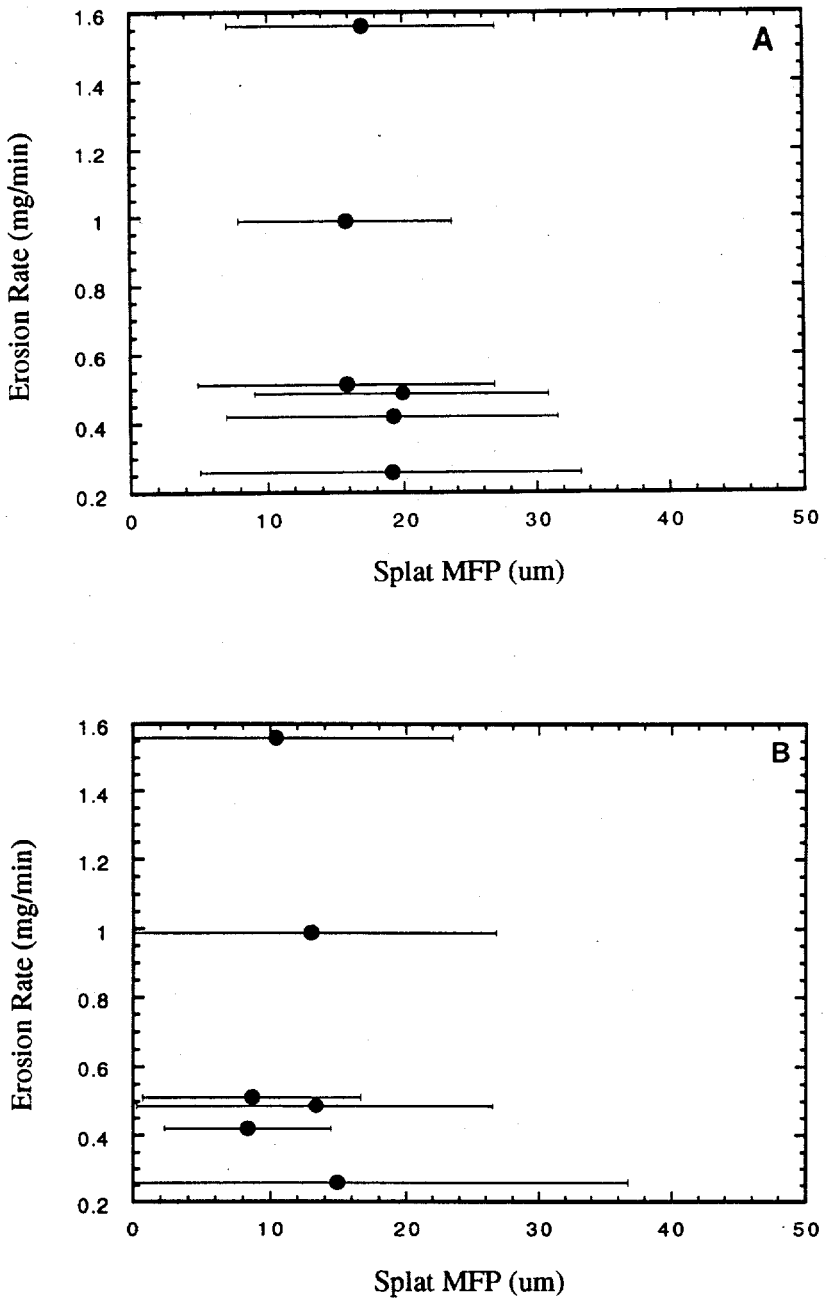

Figure IV.41- Erosion rate versus splat MFP for APS Fe/Al alloy coatings: a.planar, b.cross section (90°).

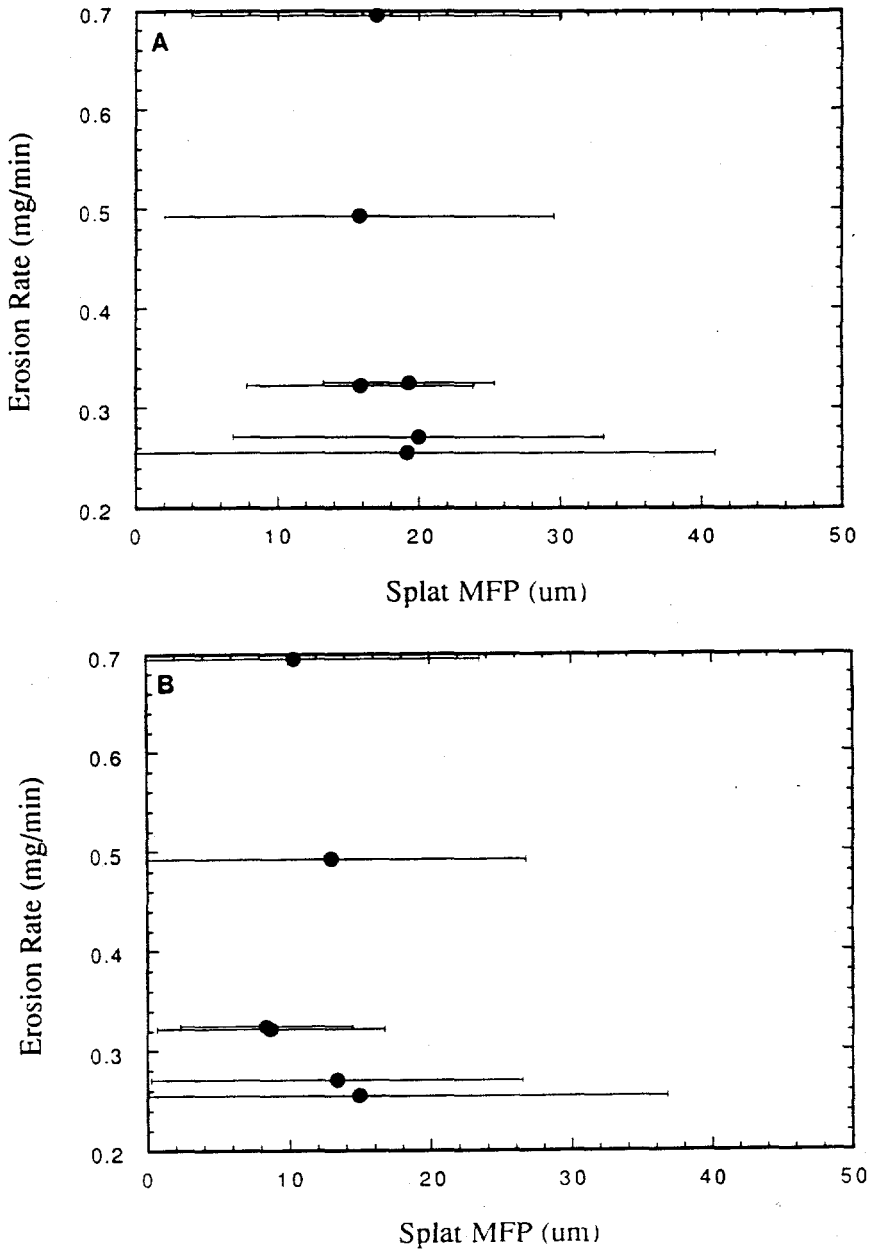

Figure IV.42- Erosion rate versus splat MFP for APS Fe/Al coatings: a.planar, b.cross section (30°).

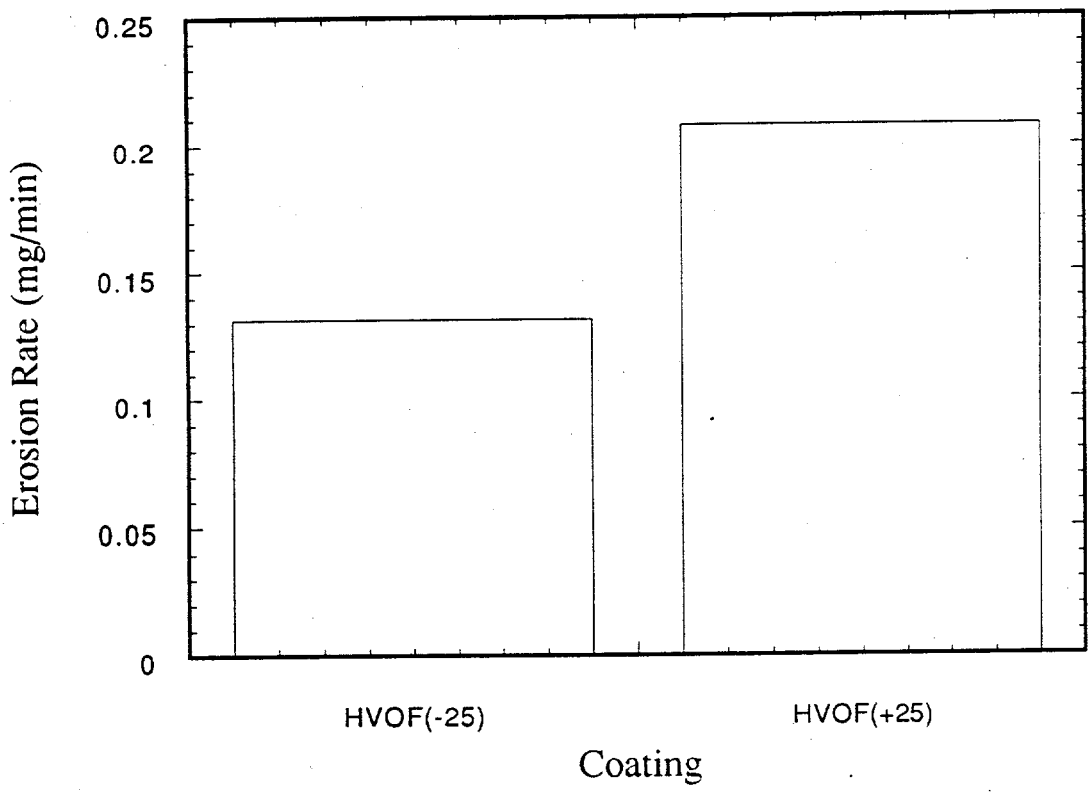

Figure 43- Erosion rate data for the HVOF Fe/Al coatings, both -25μm and +25 μm (90°).

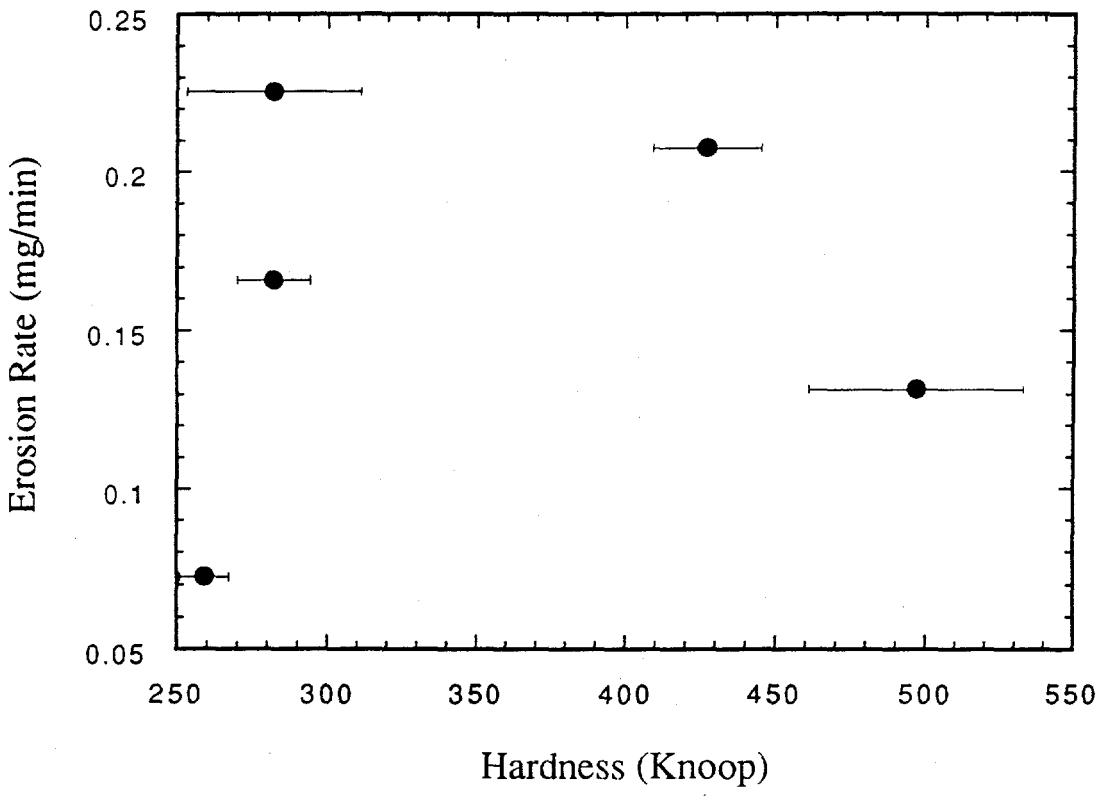

Figure IV.44- Erosion rate versus measured knoop hardness values for VPS, HVOF, VPS-HT, and wrought Fe/Al alloy materials (90°).

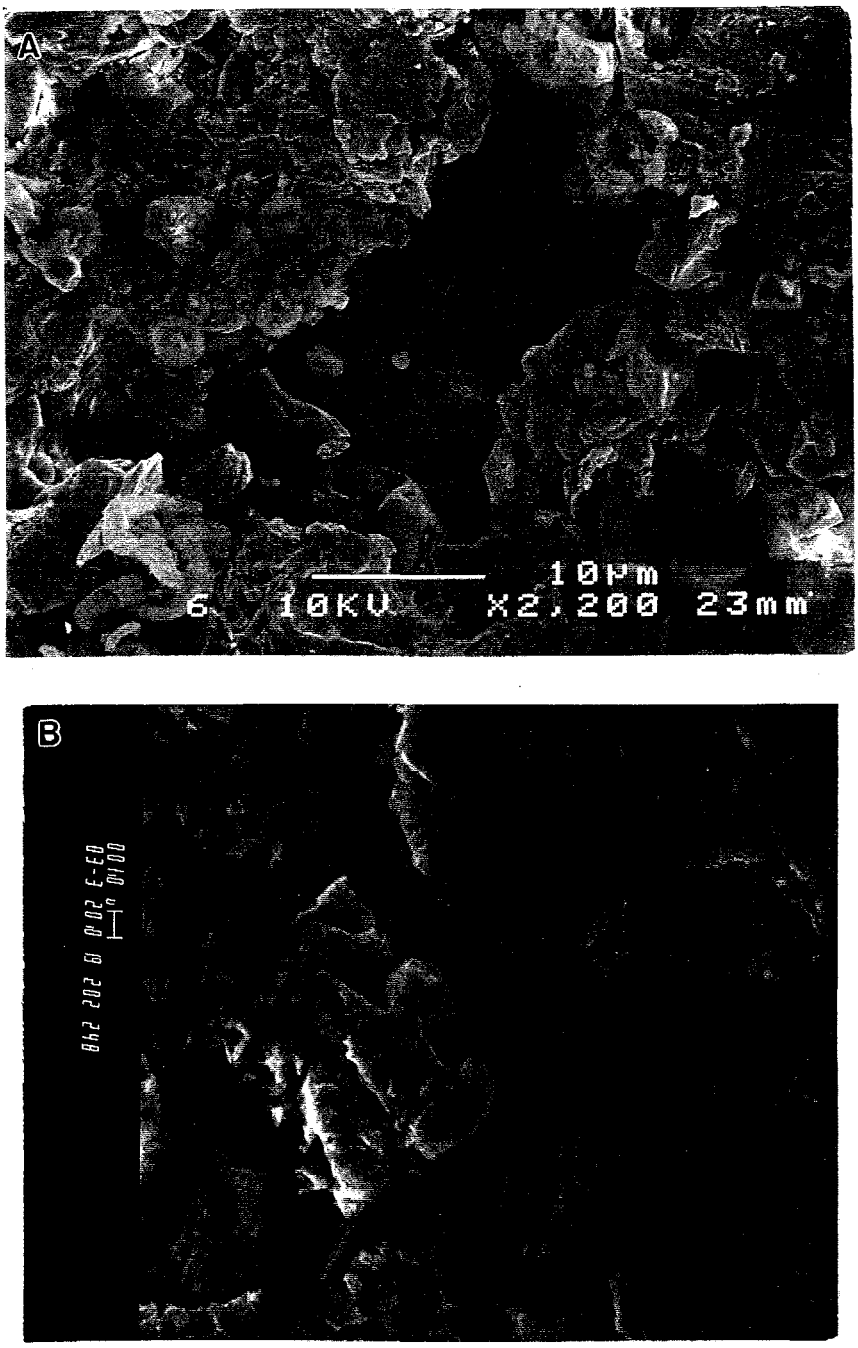

Figure IV.45- Missing splats in APS Fe/Al alloy coatings: 60% Al_2O_3 (30°), B. 60% Al_2O_3 (90°).

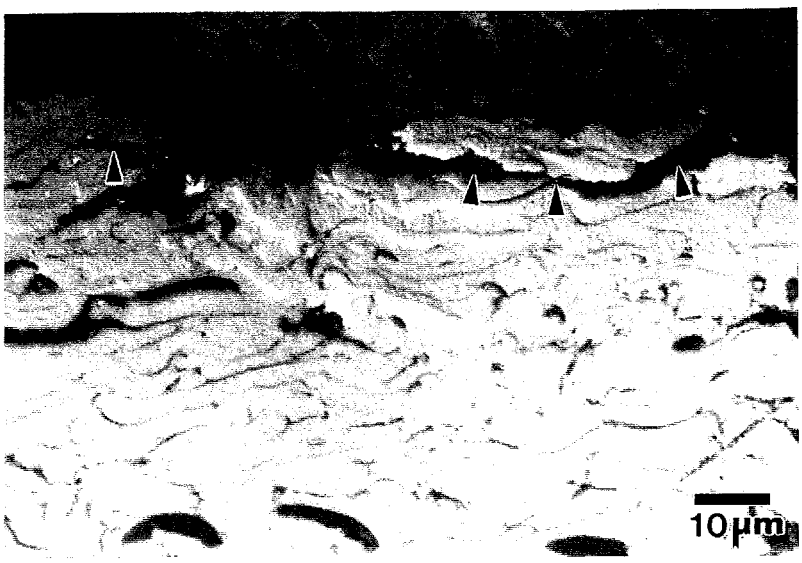

Figure IV.46- Splat debonding in a 10% Al_2O_3 -90% FeAl VPS +25µm coating (90°), arrows indicate splat delamination sites.

Figure IV.47- Surface cracking of alumina in a 40% Al_2O_3 - 60% FeAl VPS +25µm coating (90°), arrows indicate cracked alumina.

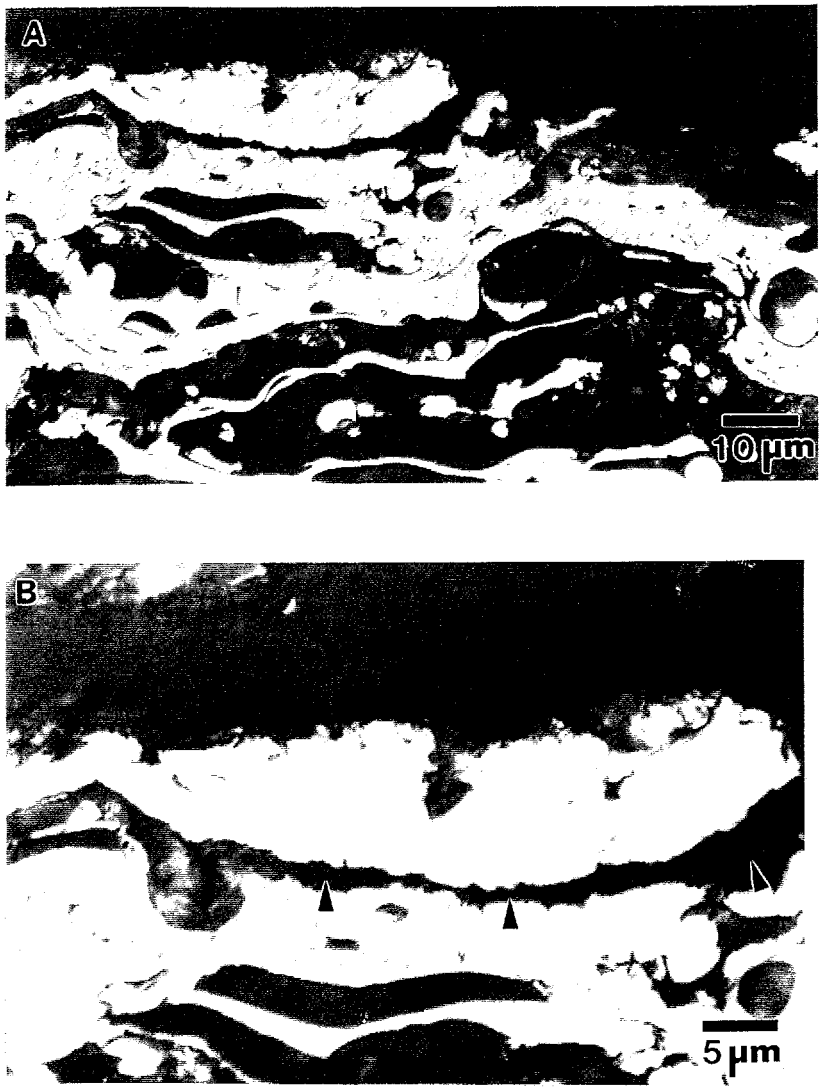

Figure IV.48- Undercutting of FeAl matrix via alumina cracking in a 60% Al_2O_3-40% FeAl VPS +25µm coating (90°): a. coating, b. individual partially delaminated splat, arrows indicate missing oxide which has lead to splat delamination.

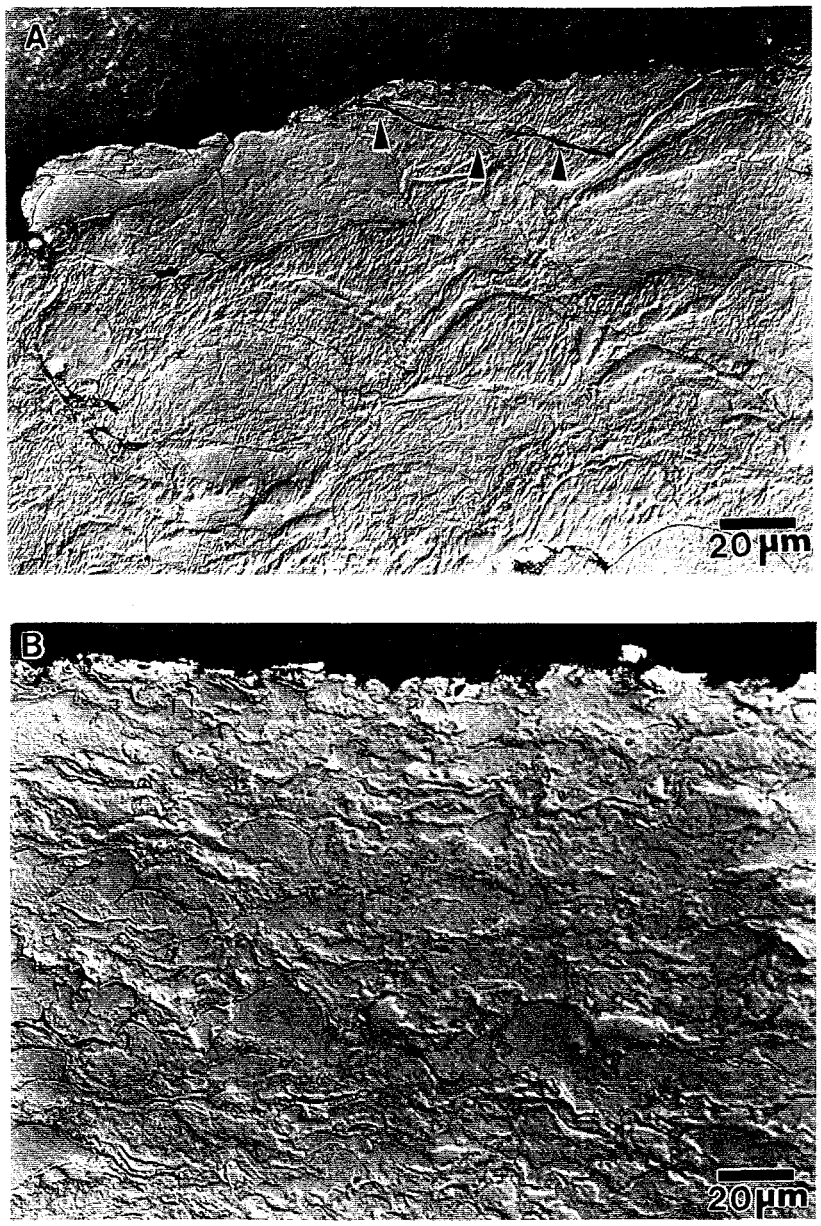

Figure IV.49- a.Cracking along splat boundaries in a 100% HVOF FeAl +25µm coating (90°), arrows indicate splat interface cracks, b. Lack of cracking along splat boundaries in a 100% HVOF FeAl -25µm coating (90°).

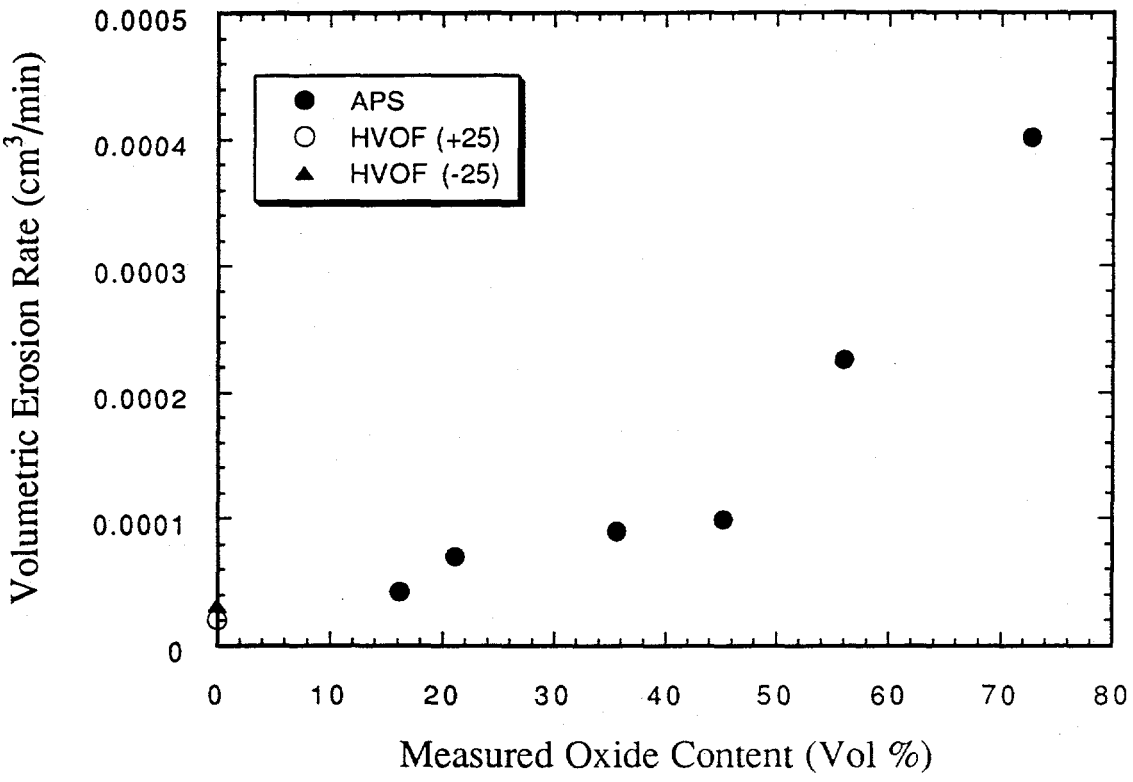

Figure IV.50- Comparison of FeAl alloy HVOF and FeAl alloy plasma coatings (90° erosion data).

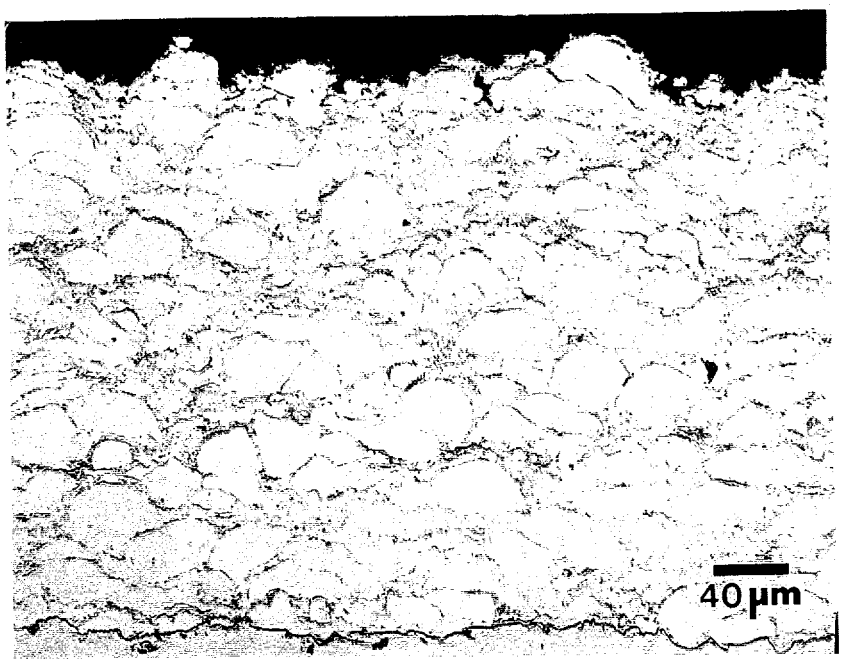

Figure IV.51- FeCrAlY HVOF coating with 75psi gun chamber pressure (500x).

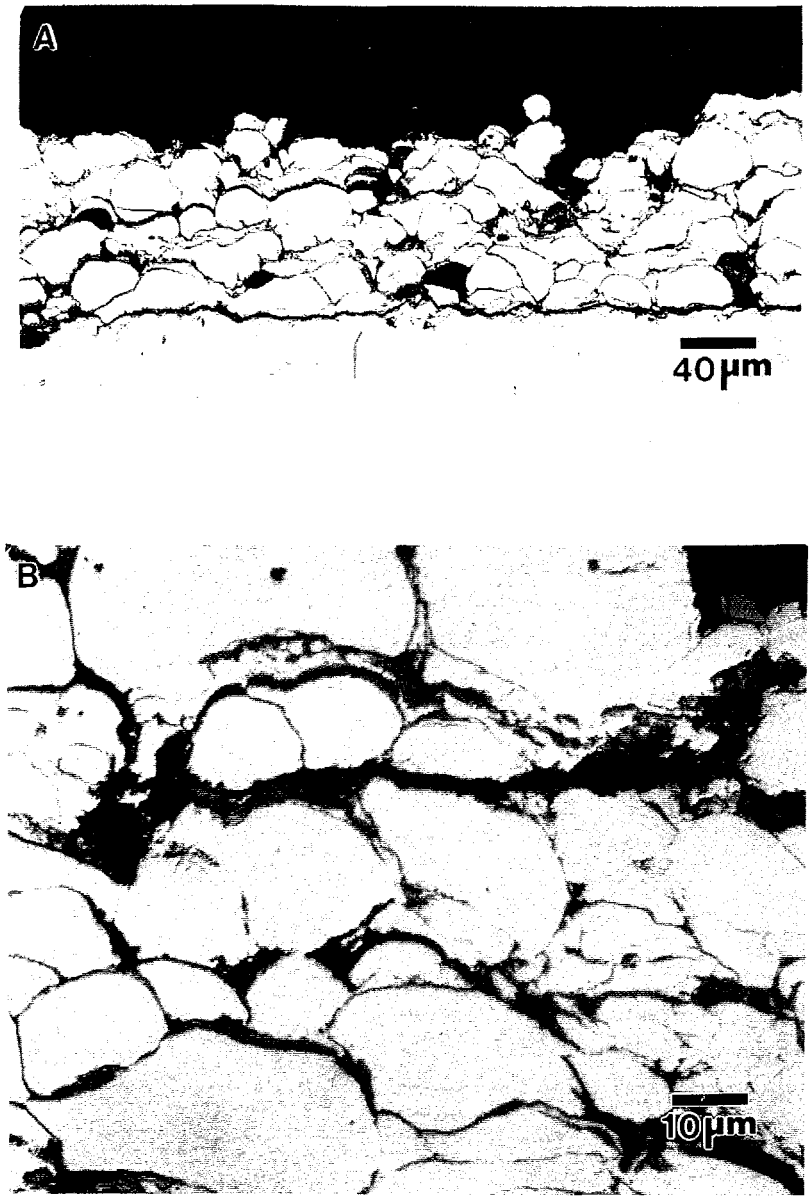

Figure IV.52- FeCrAlY HVOF coating with 99psi gun chamber pressure: a.250x, b.1000x(Nomarski).

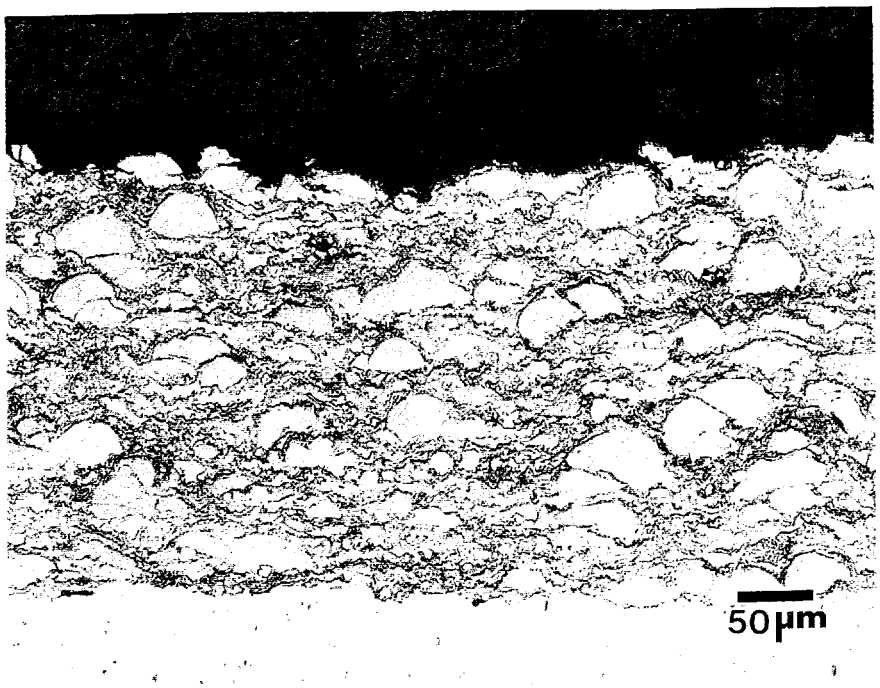

Figure IV.53- 90% FeCrAlY-10% Cr_3C_2 HVOF coating before Murakami's (200x).

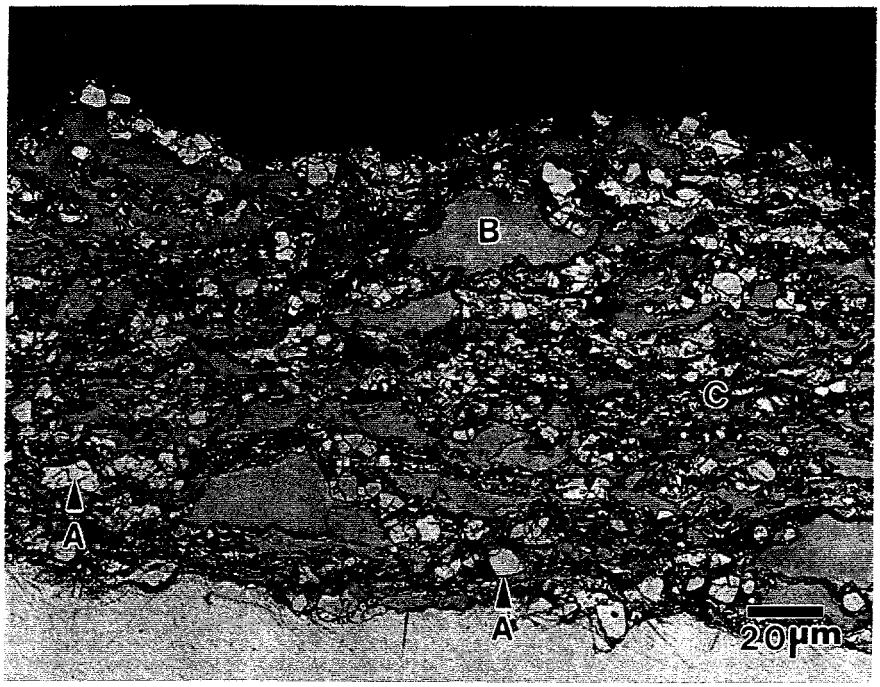

Figure IV.54- 80% FeCrAlY-20% Cr_3C_2 HVOF coating after Murakami's (500x): a.carbides, b. FeCrAlY matrix, and c. oxides.

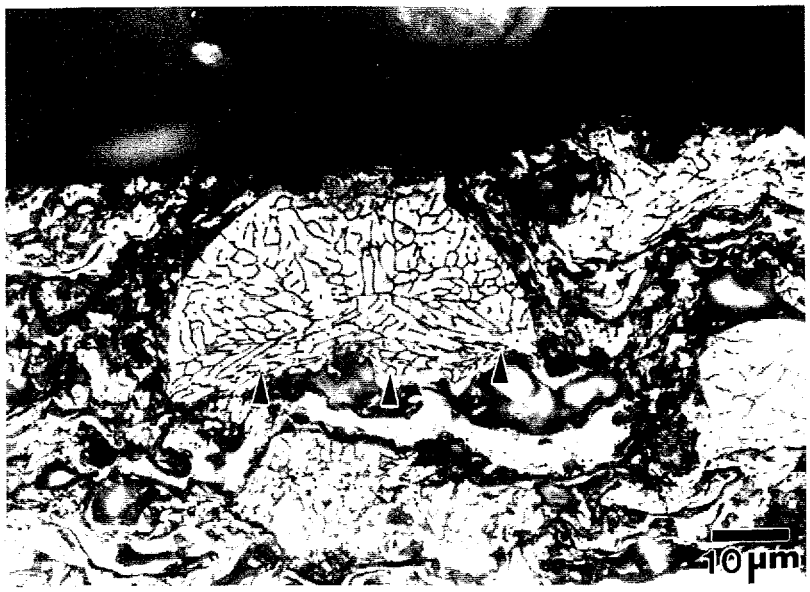

Figure IV.55- 60% FeCrAlY-40% Cr_3C_2 HVOF, etched (1000x), arrows indicate deformation of the unmelted particle.

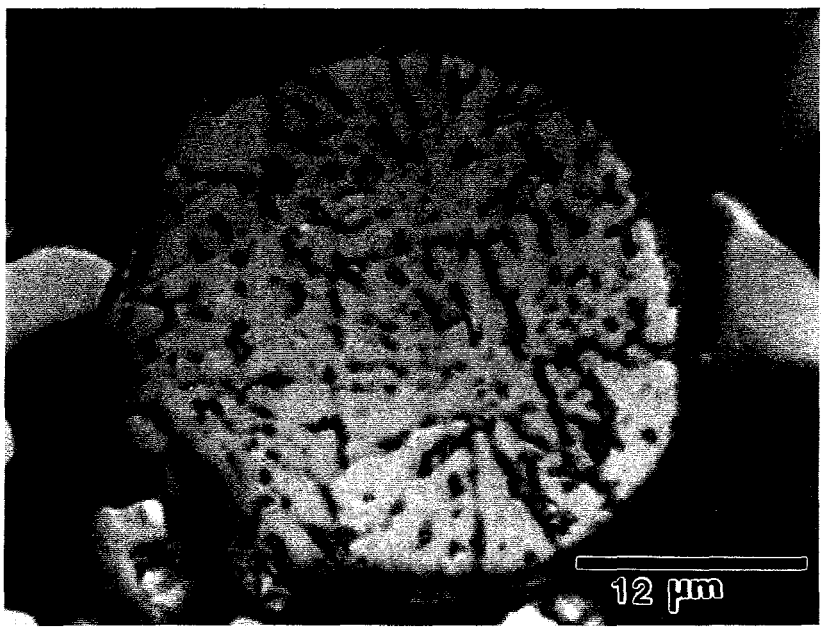

Figure IV.56- Starting FeCrAlY powder microstructure.

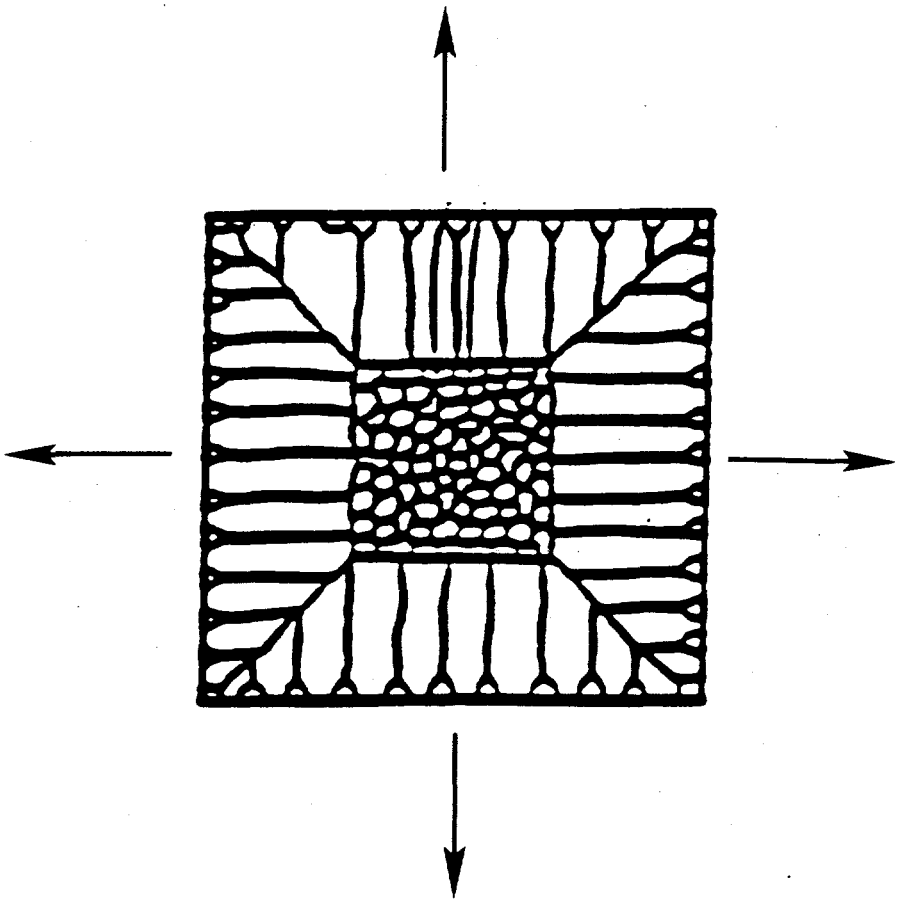

Figure IV.57- Casting schematic showing the columnar grain formation parallel to the heat flow, arrows indicate heat flow.

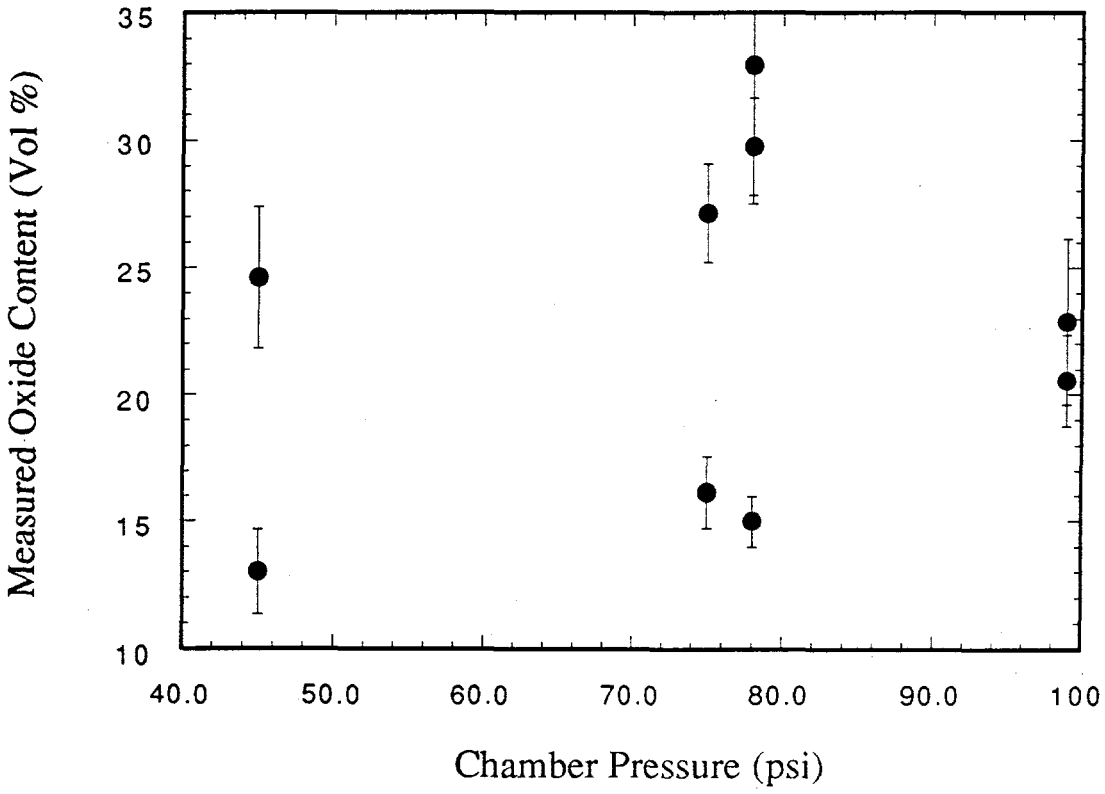

Figure IV.58- HVOF chamber pressure versus the measured oxide content in the FeCrAlY HVOF coatings.

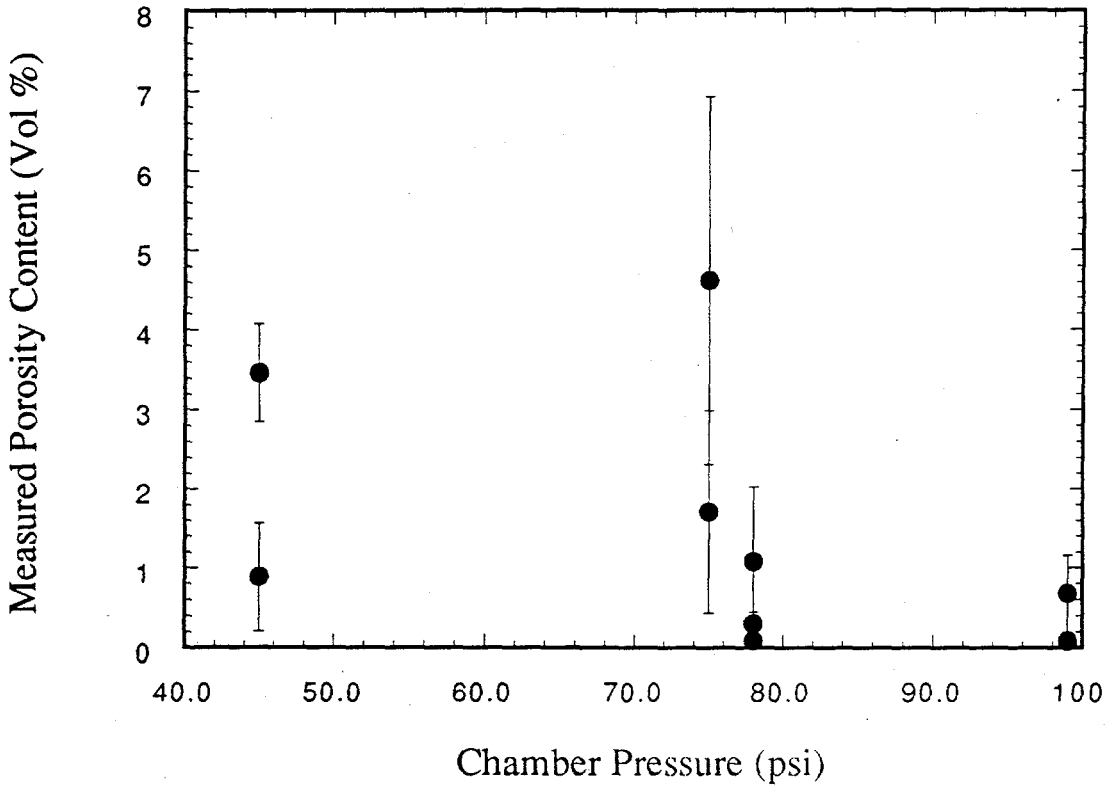

Figure IV.59 HVOF chamber pressure versus the measured porosity in the FeCrAlY HVOF coatings.

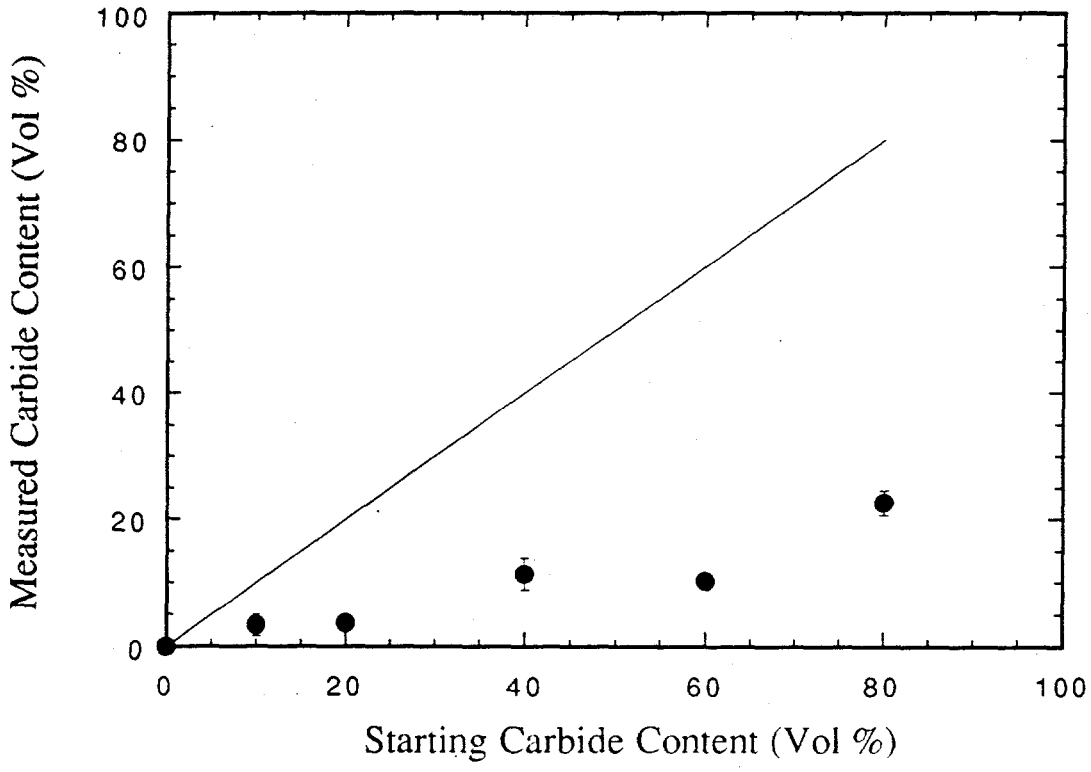

Figure IV.60- Measured carbide content versus the starting Cr_3C_2 content in the FeCrAlY-Cr_3C_2 HVOF coatings.

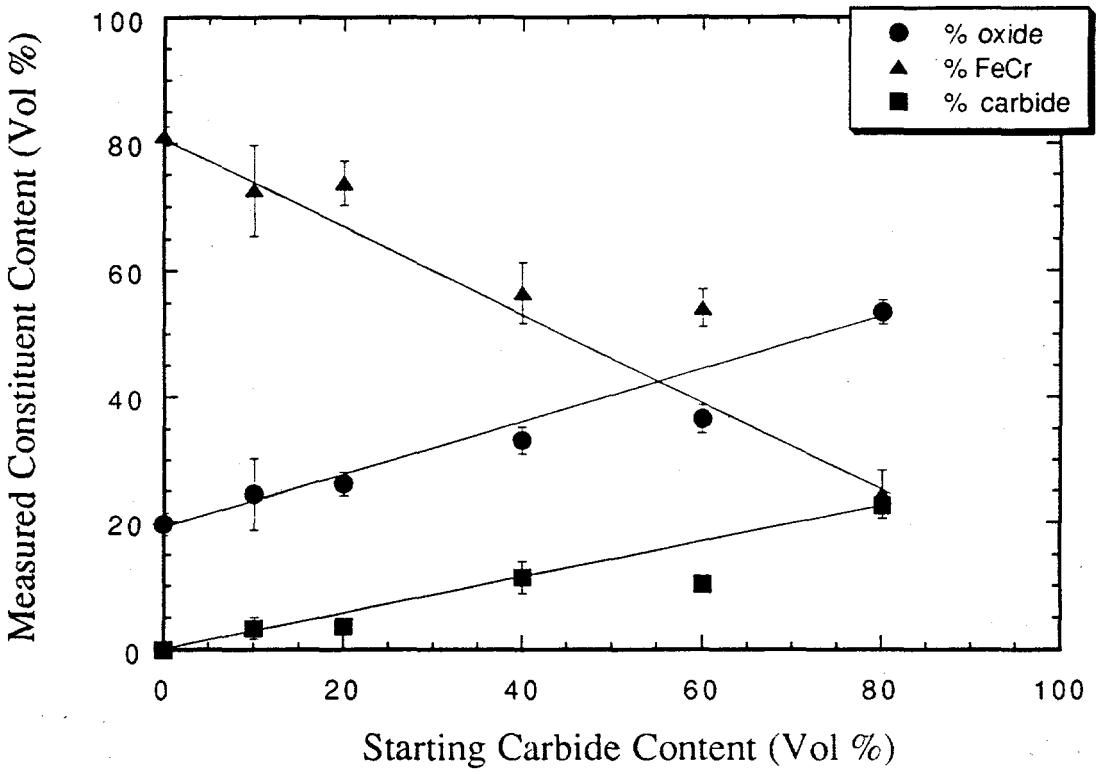

Figure IV.61- Measured constituent content versus the starting Cr_3C_2 content in the FeCrAlY-Cr_3C_2 HVOF coatings.

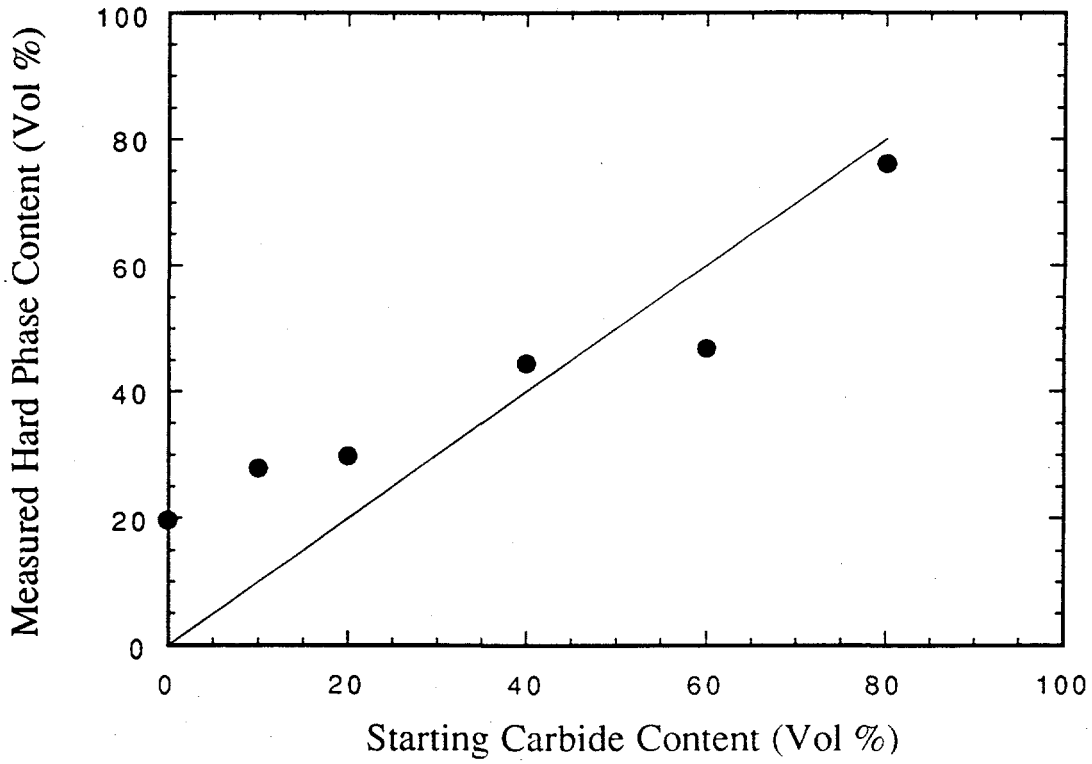

Figure IV.62- Measured hard phase (oxides and carbides) content versus the starting Cr_3C_2 content in the FeCrAlY-Cr_3C_2 HVOF coatings.

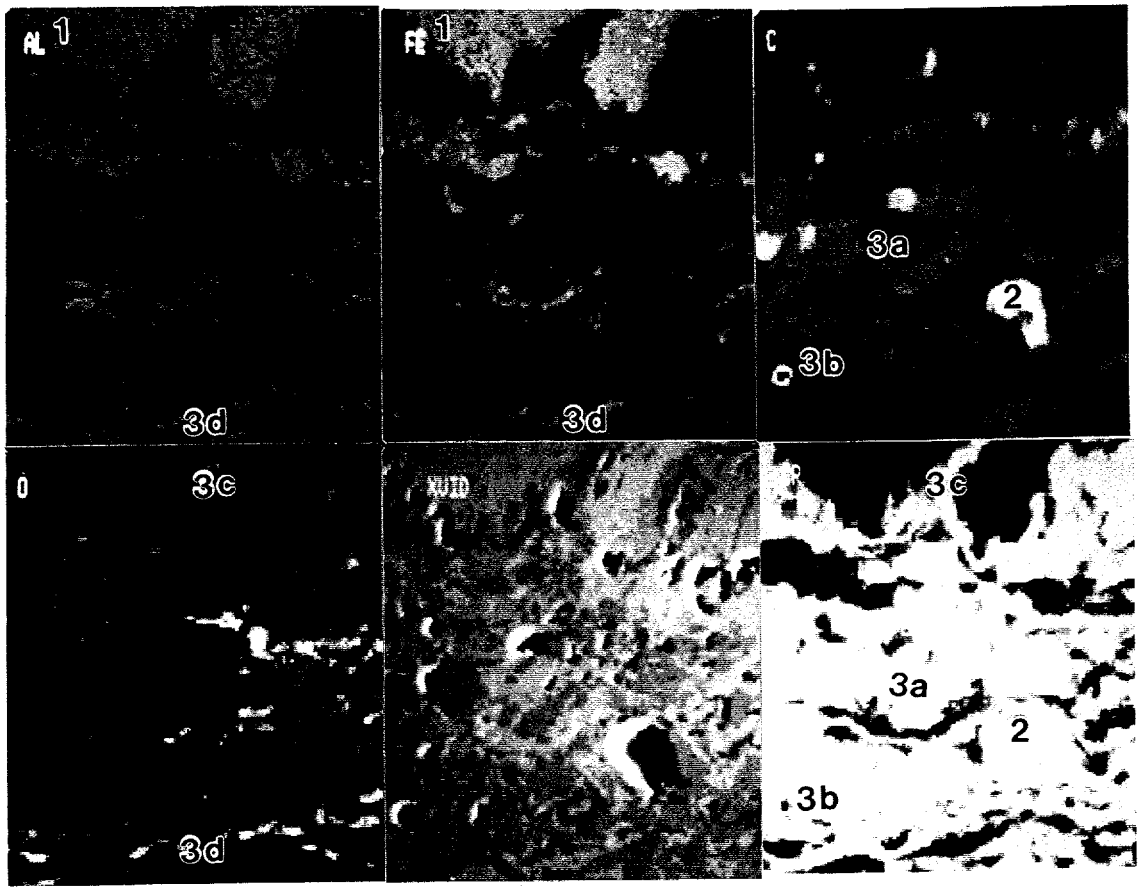

Figure IV.63- EDS/WDS dot map for 80% Cr_3C_2-20% FeCrAlY coating (1500x): 1. matrix, 2. Cr_3C_2, 3a. Cr_7C_3, 3b. $Cr_{23}C_6$, 3c. CrO, 3d. various Fe and possible Al oxides.

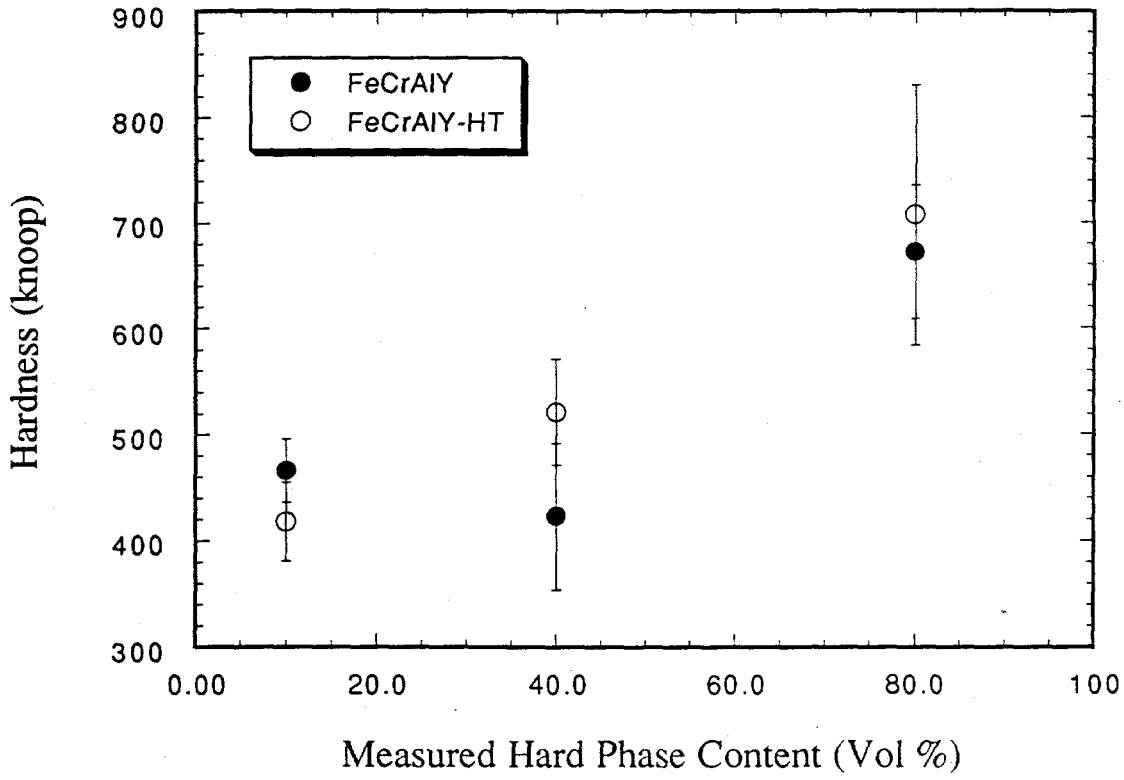

Figure IV.64 Knoop hardness data versus the measured hard phase content for the FeCrAlY-Cr_3C_2 HVOF coatings prior to and after heat treatment @ 600°C for 96 hours.

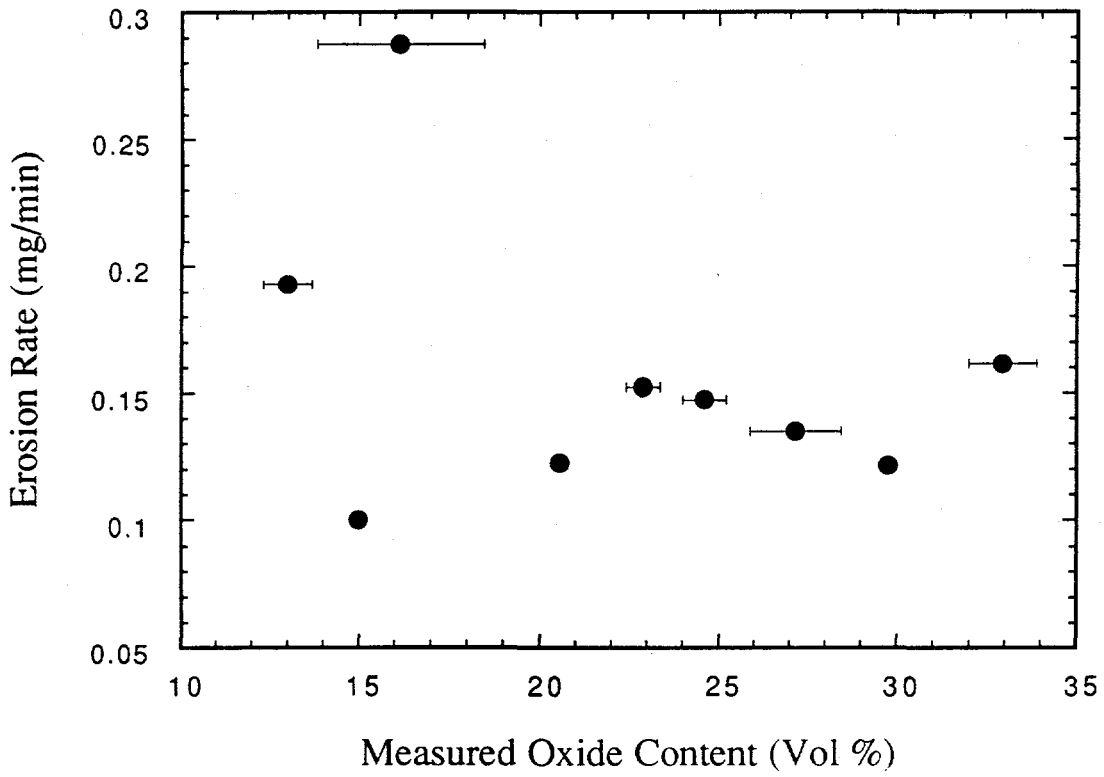

Figure IV.65- Erosion rate versus measured oxide content for the 100% FeCrAlY HVOF coatings (90°).

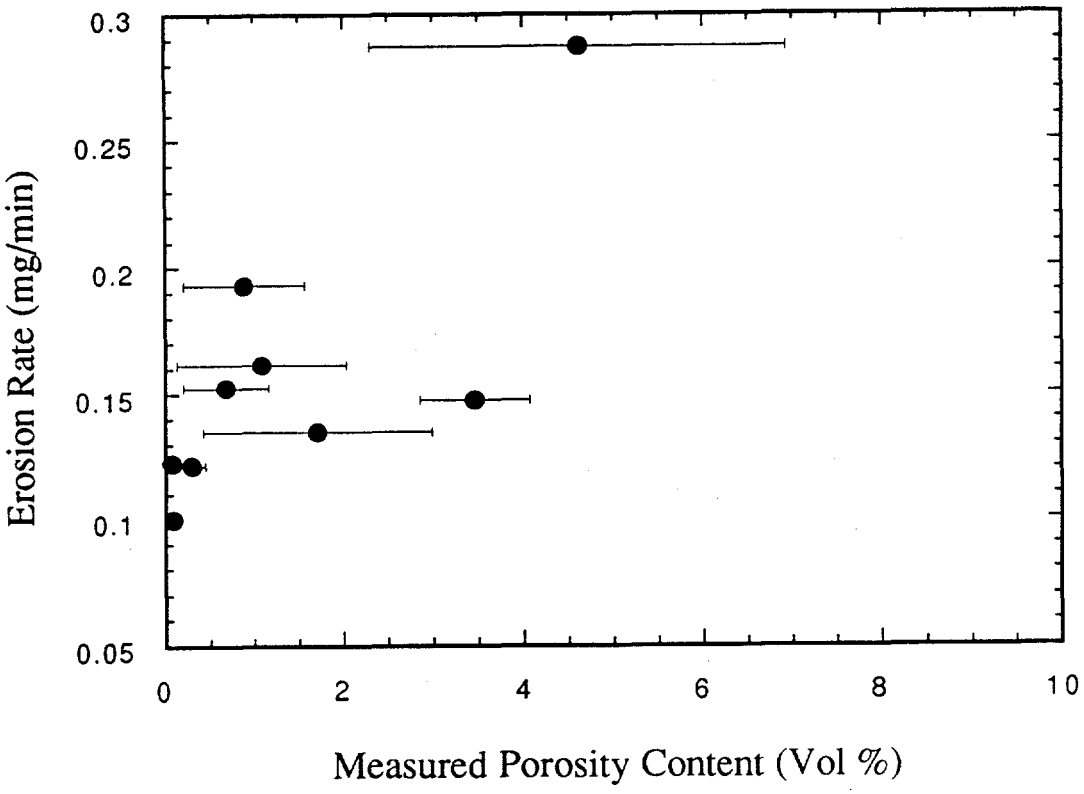

Figure IV.66- Erosion rate versus measured porosity for the 100% FeCrAlY HVOF coatings (90°).

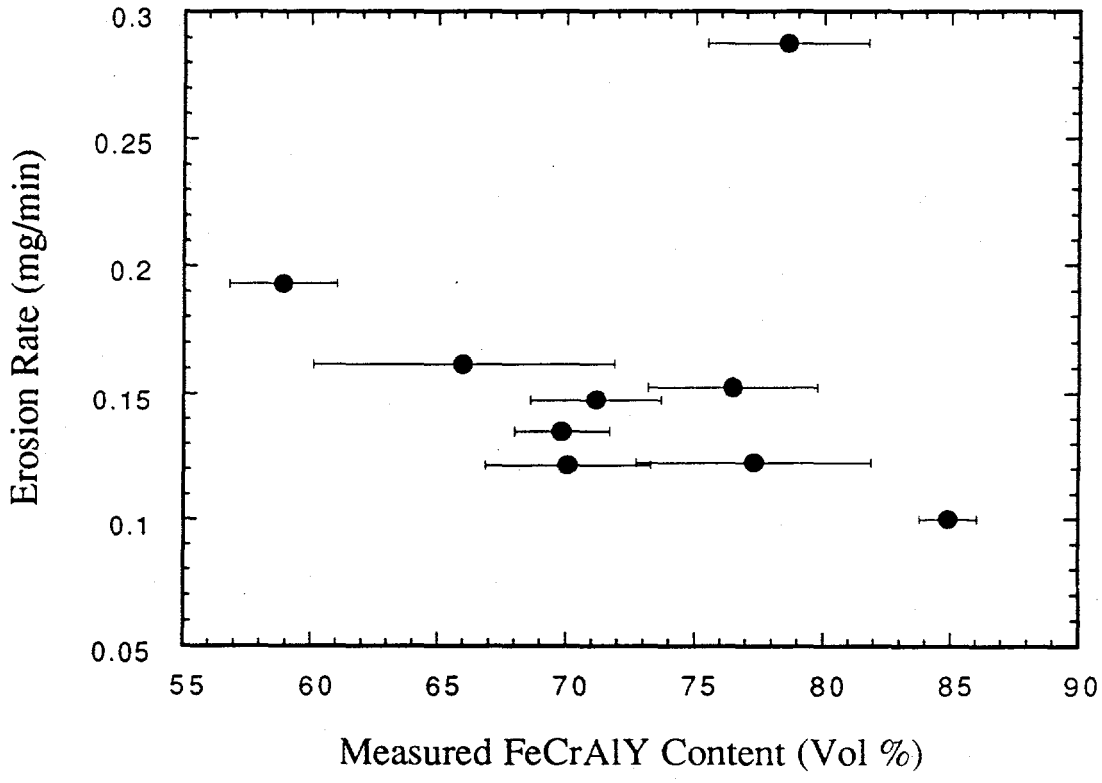

Figure IV.67- Erosion rate versus measured FeCrAlY content for the 100% FeCrAlY HVOF coatings (90°).

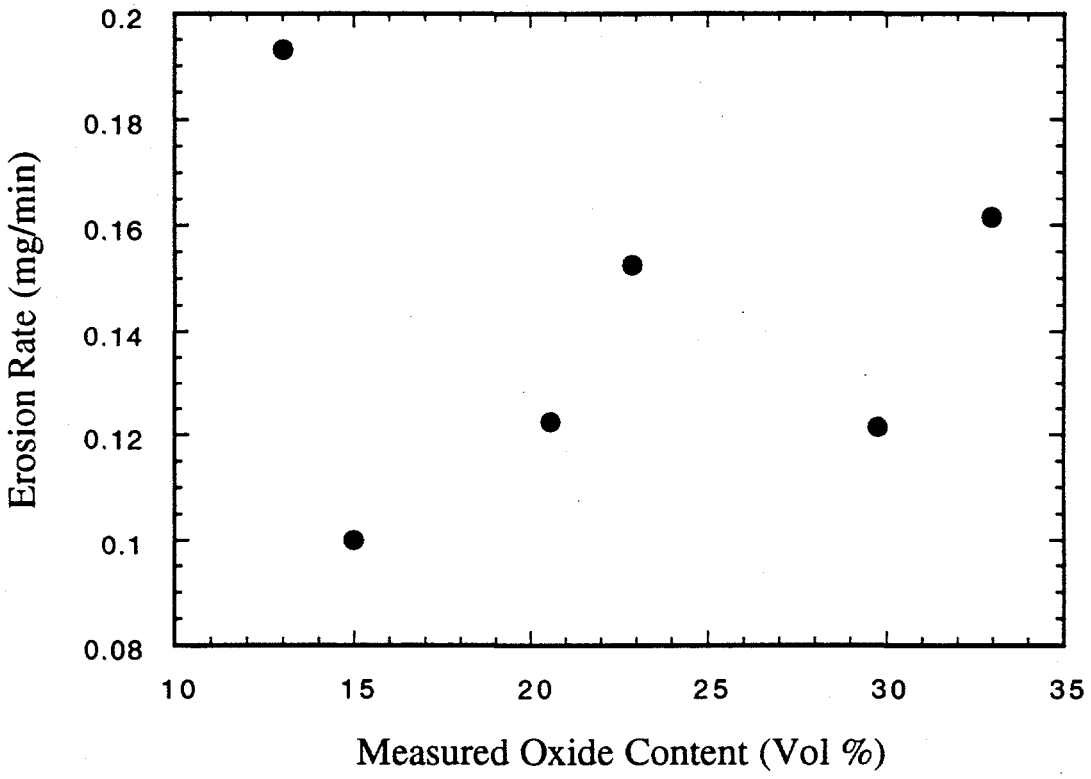

Figure IV.68- Erosion rate versus measured oxide content for the dense (<1% porosity) 100% FeCrAlY HVOF coatings (90°).

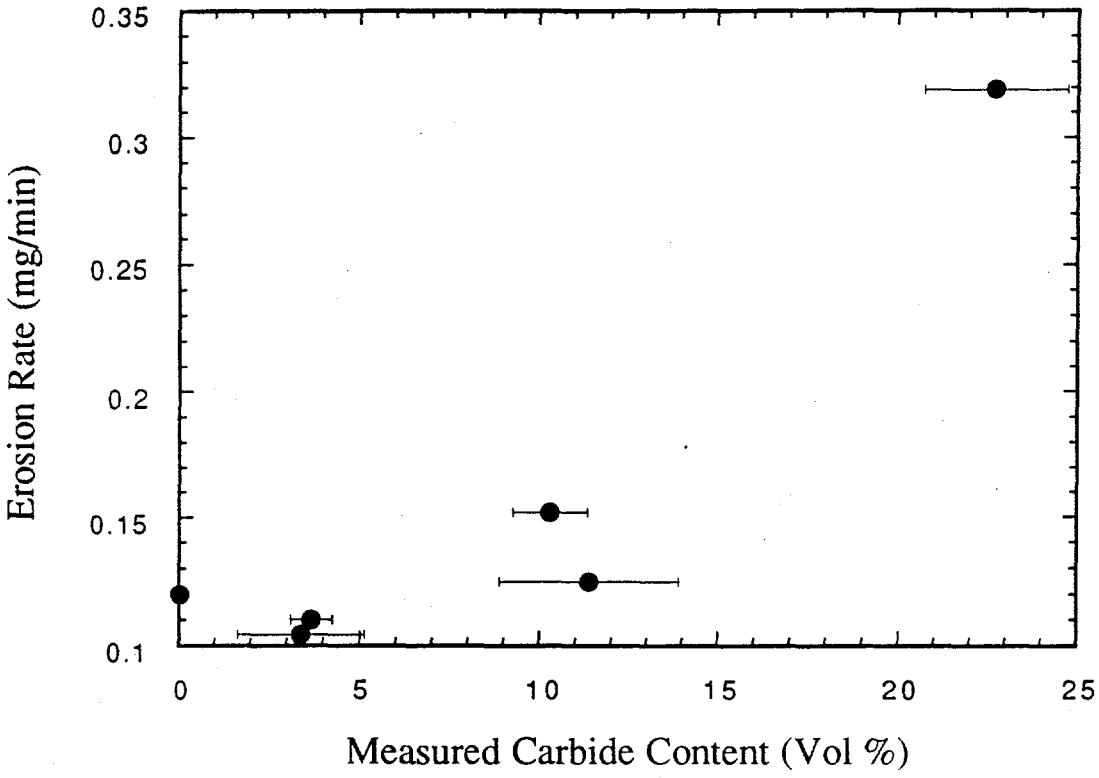

Figure IV.69 Erosion rate versus measured carbide content for the FeCrAlY-Cr_3C_2 HVOF coatings (90°).

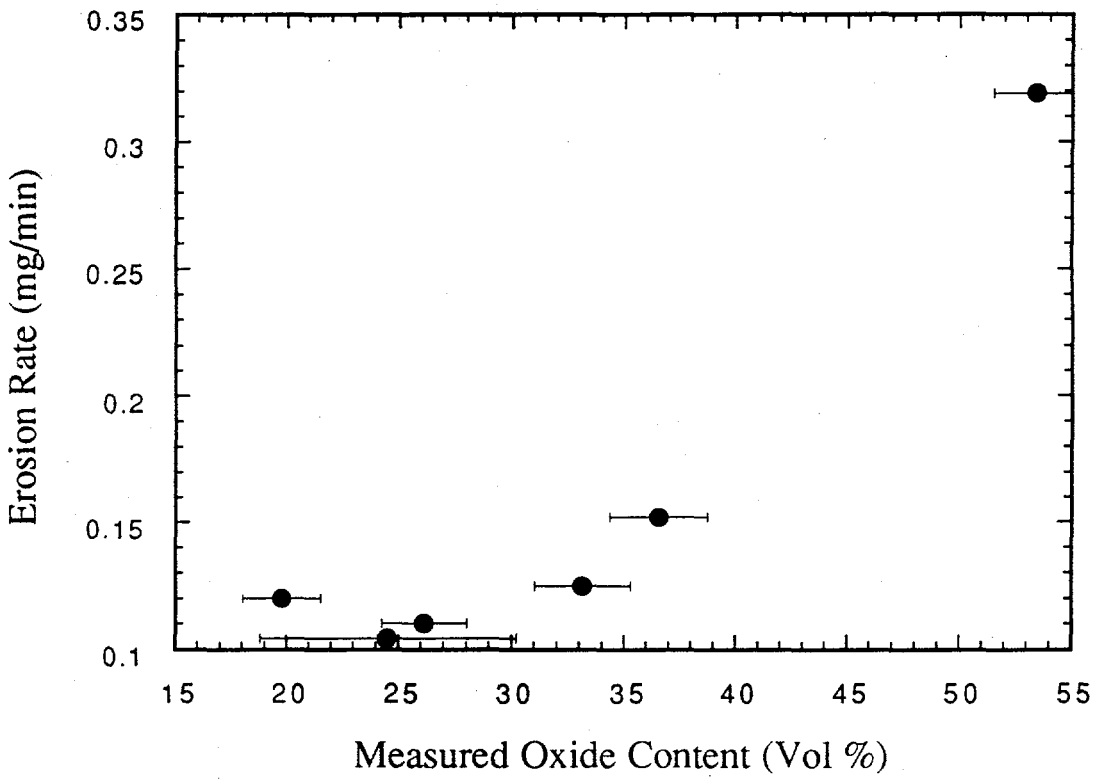

Figure IV.70- Erosion rate versus measured oxide content for the FeCrAlY-Cr_3C_2 HVOF coatings (90°).

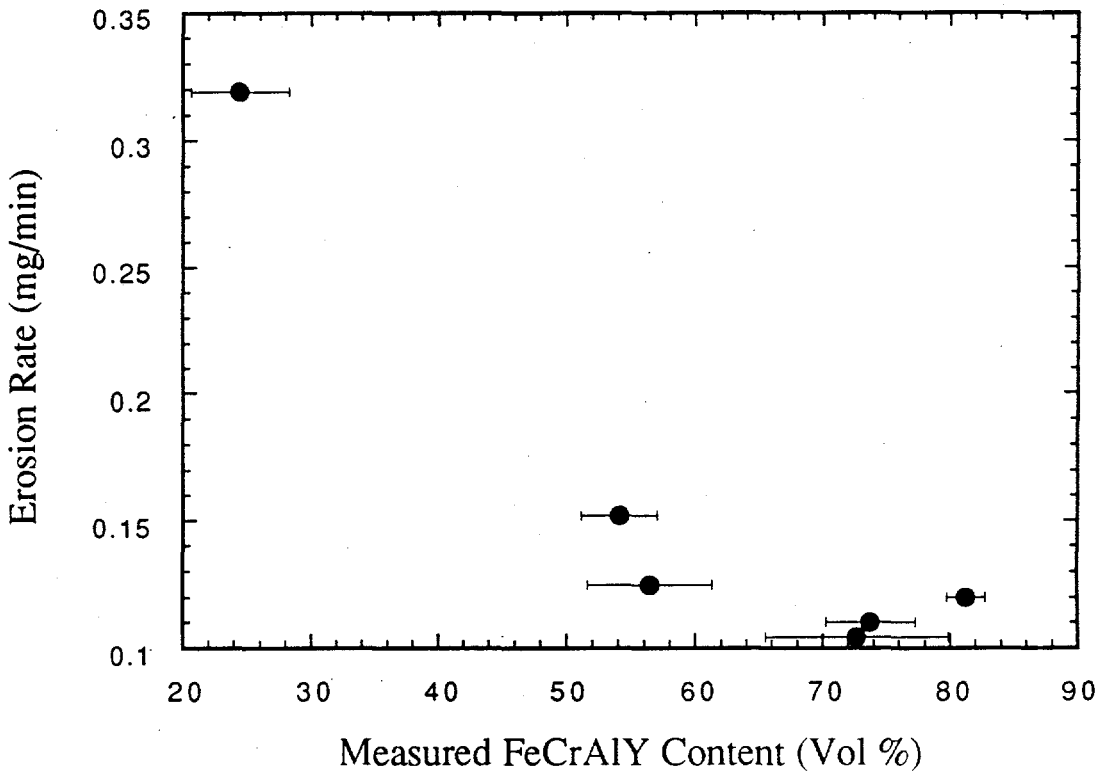

Figure IV.71- Erosion rate versus measured FeCrAlY content for the FeCrAlY-Cr_3C_2 HVOF coatings (90°).

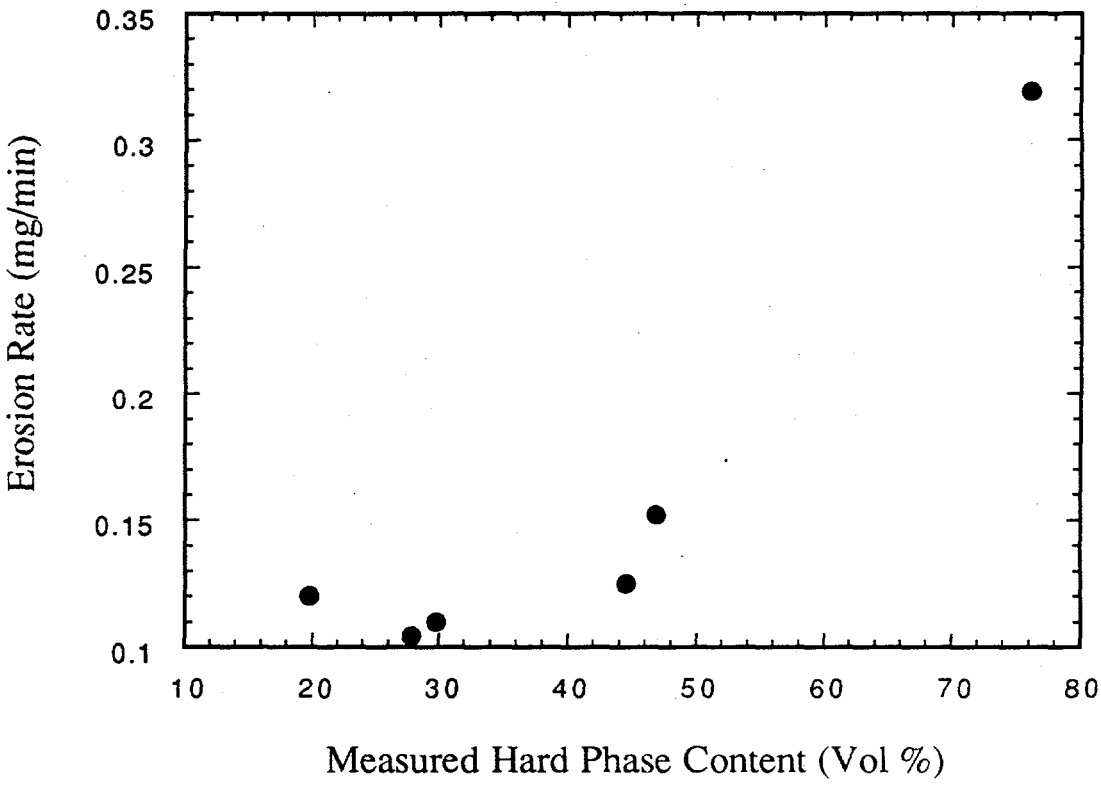

Figure IV.72- Erosion rate versus measured hard phase content (oxides and carbides) for the FeCrAlY-Cr_3C_2 HVOF coatings (90°).

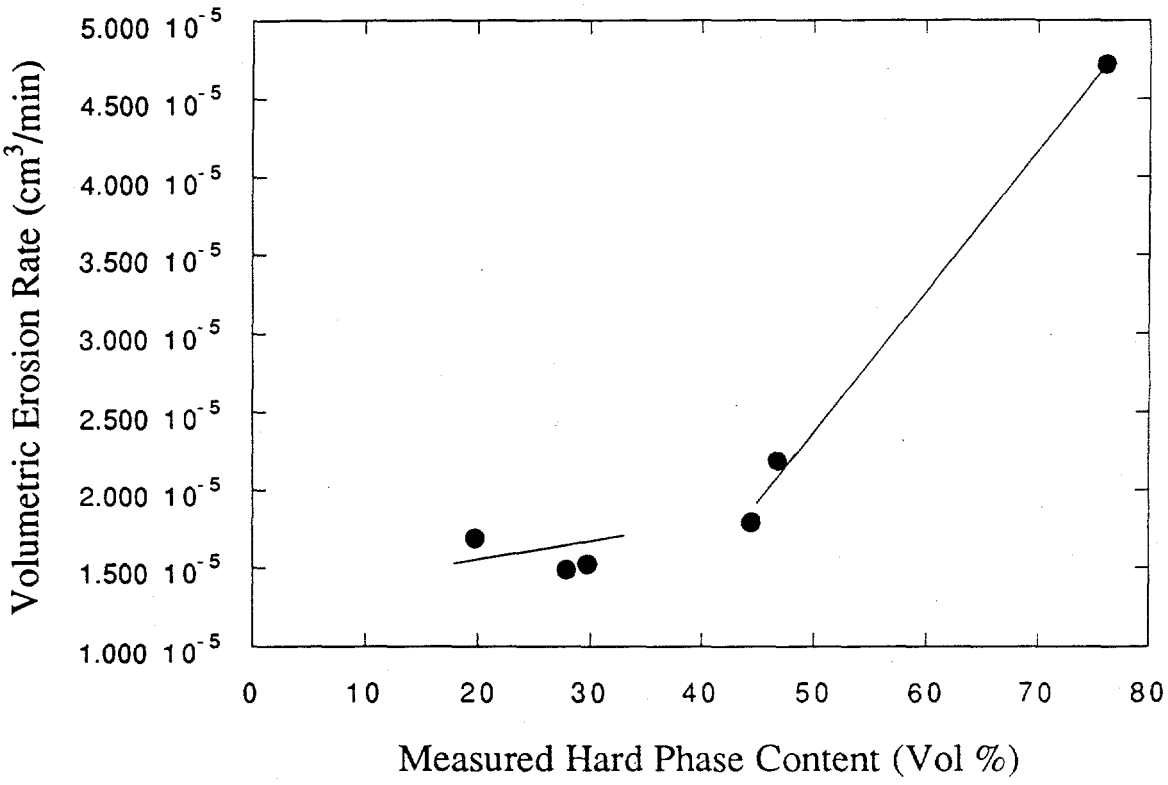

Figure IV.73- Volumetric erosion rate versus measured hard phase (oxides and carbides) content for the FeCrAlY-Cr_3C_2 HVOF coatings (90°).

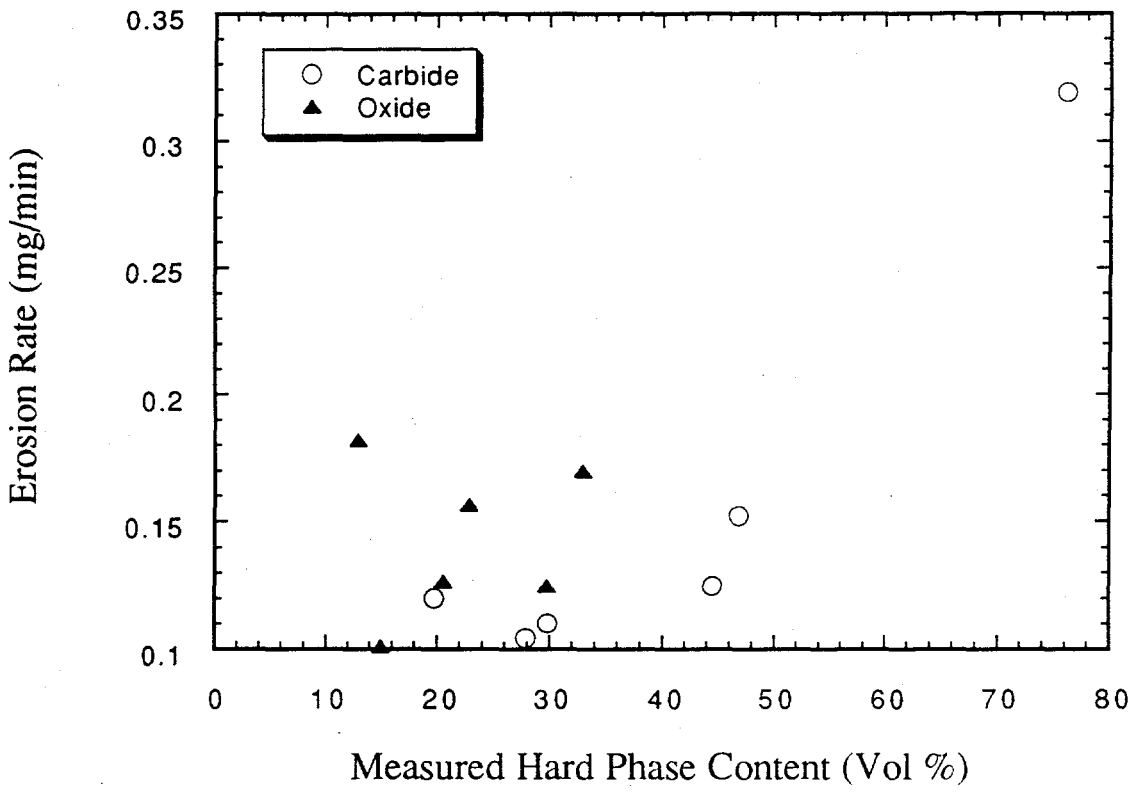

Figure IV.74 Erosion rate versus measured hard phase content (oxides and carbides) for the FeCrAlY-Cr_3C_2 and 100% FeCrAlY HVOF coatings (90°).

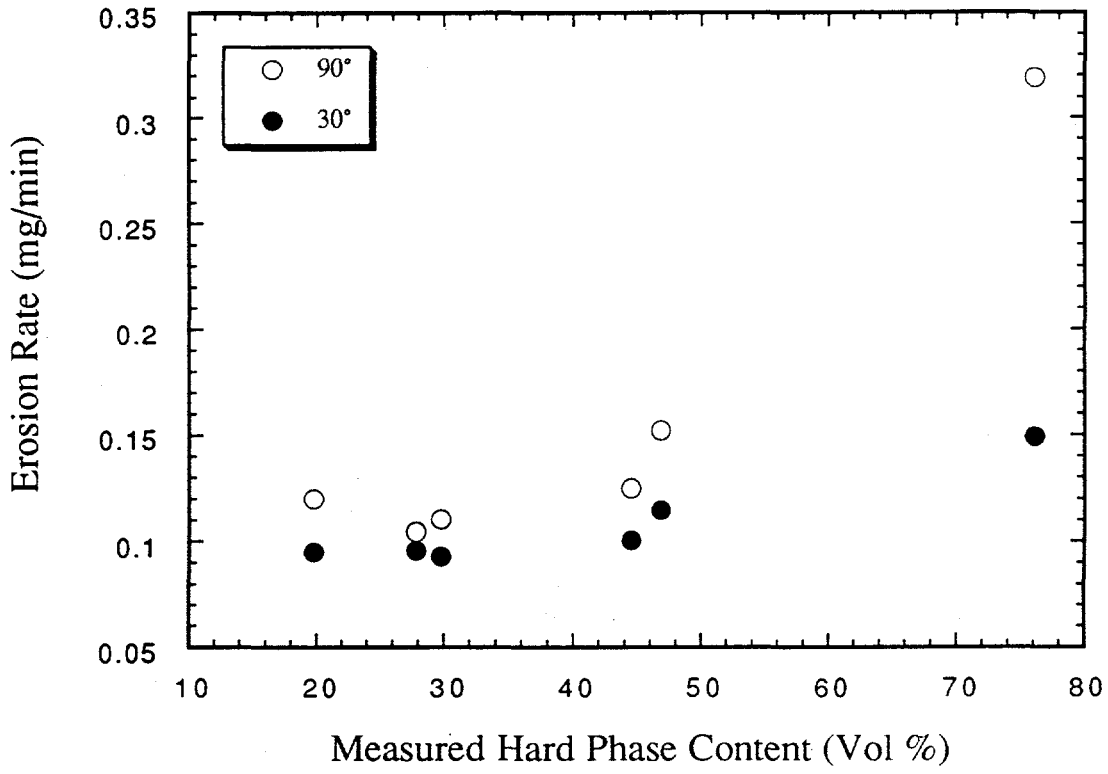

Figure IV.75- Erosion rate versus measured hard phase content (oxides and carbides) for the FeCrAlY-Cr_3C_2 HVOF coatings (30° and 90°).

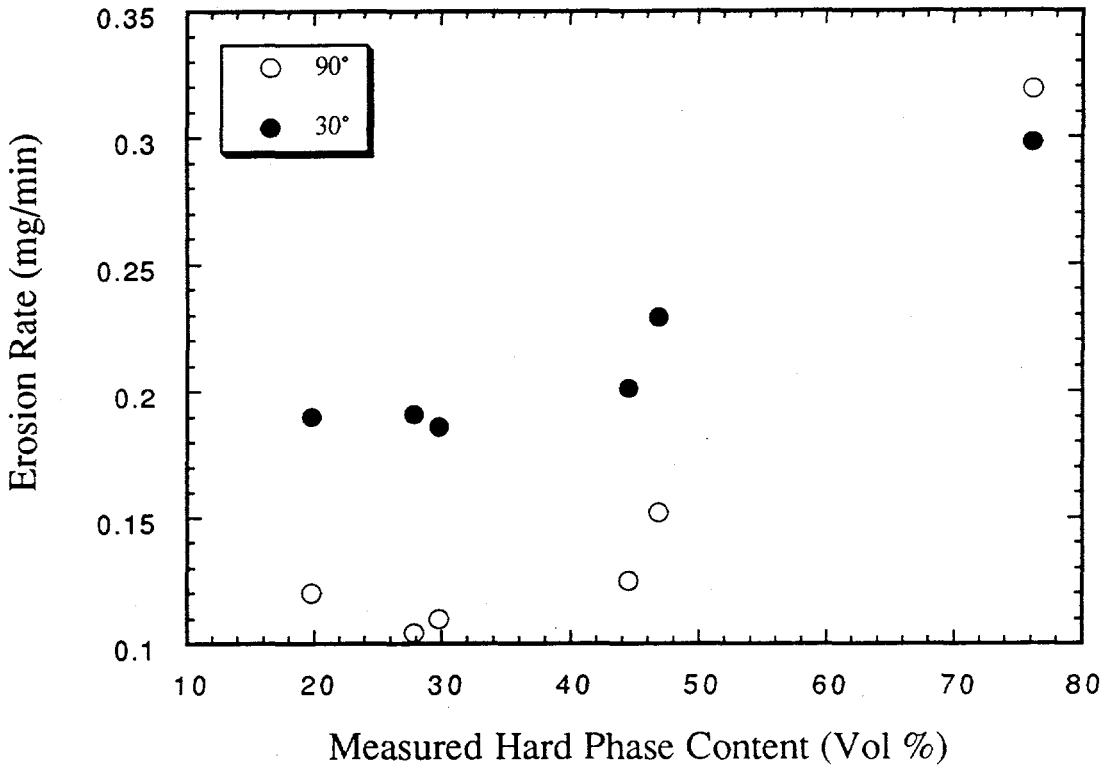

Figure IV.76- Erosion rate versus measured hard phase content (oxides and carbides) for the FeCrAlY-Cr_3C_2 HVOF coatings with corrected 30° data (30°and 90°).

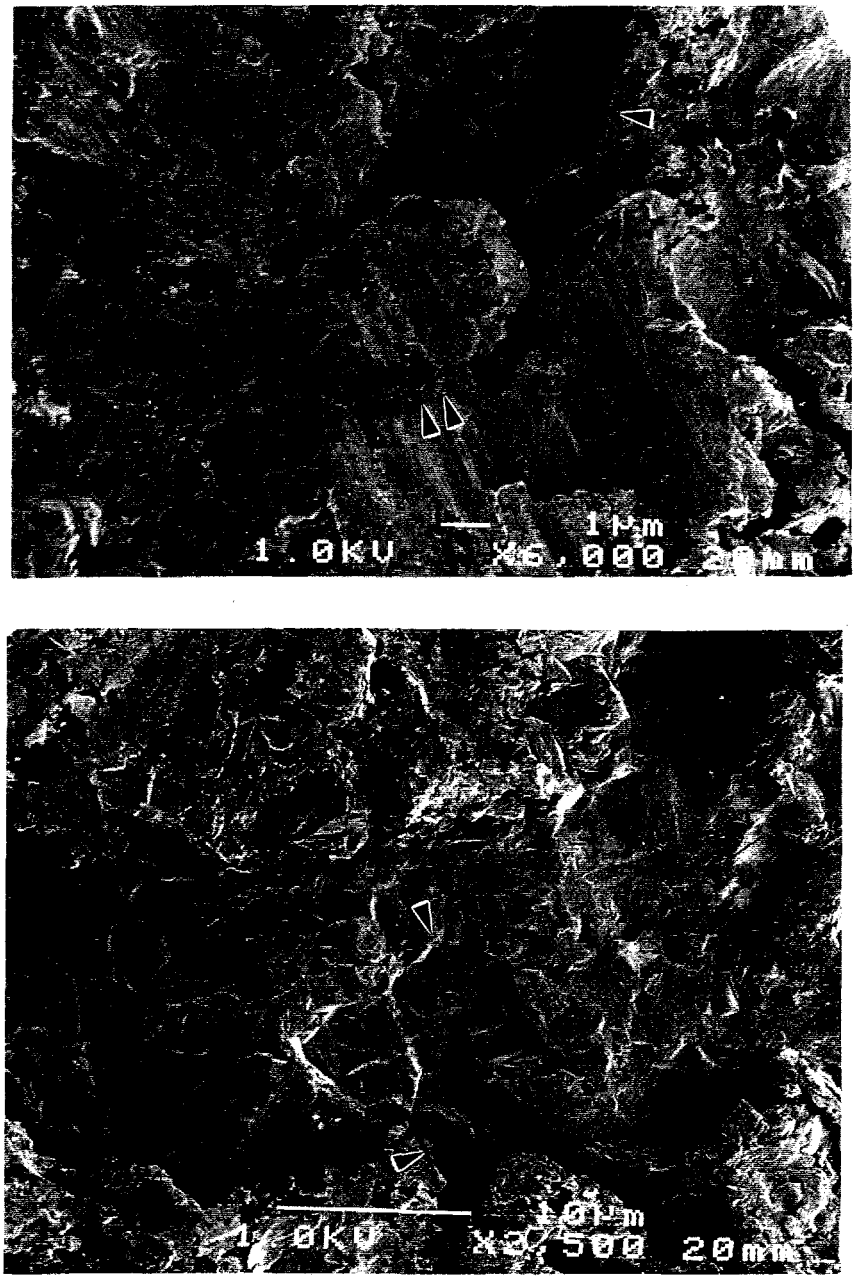

Figure IV.77- Possible carbide pullout (see arrows) in an 60% Cr_3C_2-40% FeCrAlY HVOF coatings (90°), note the crack in the top picture (indicated by the double arrow) may represent a carbide in the early stages of pullout.

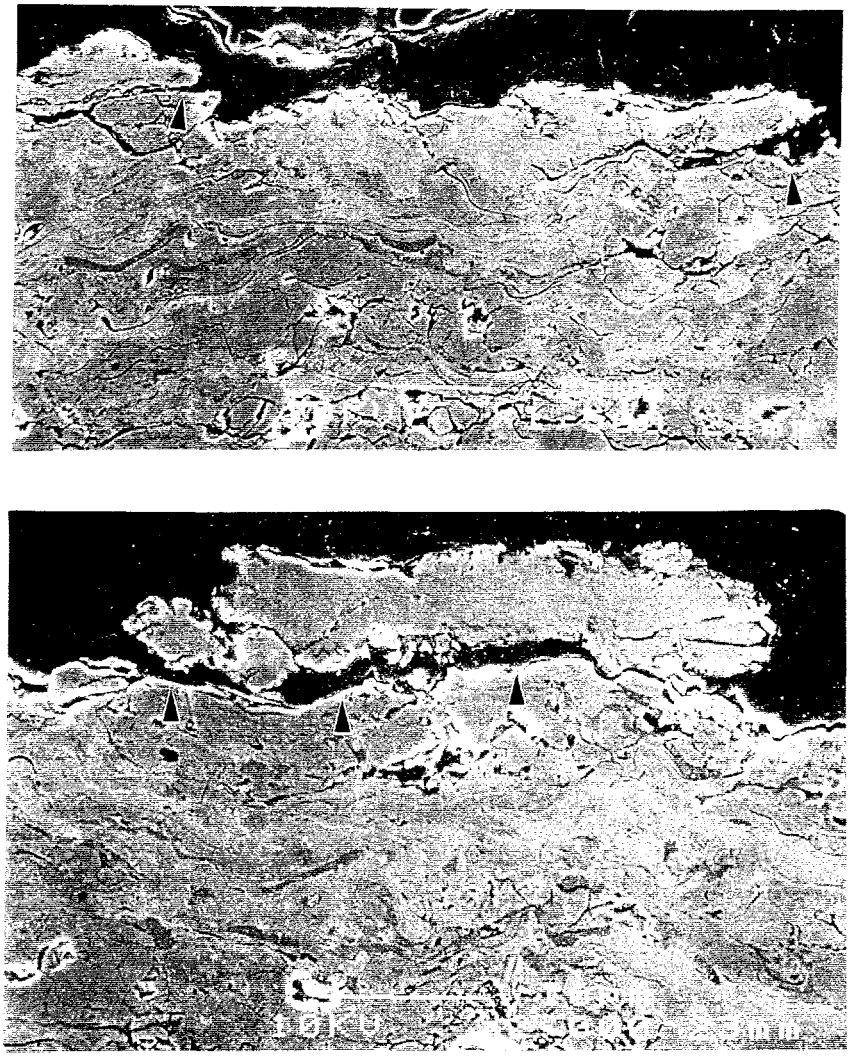

Figure IV.78- Debonding (indicated by arrows) in an 80% Cr_3C_2-20% FeCrAlY HVOF coatings (90°).

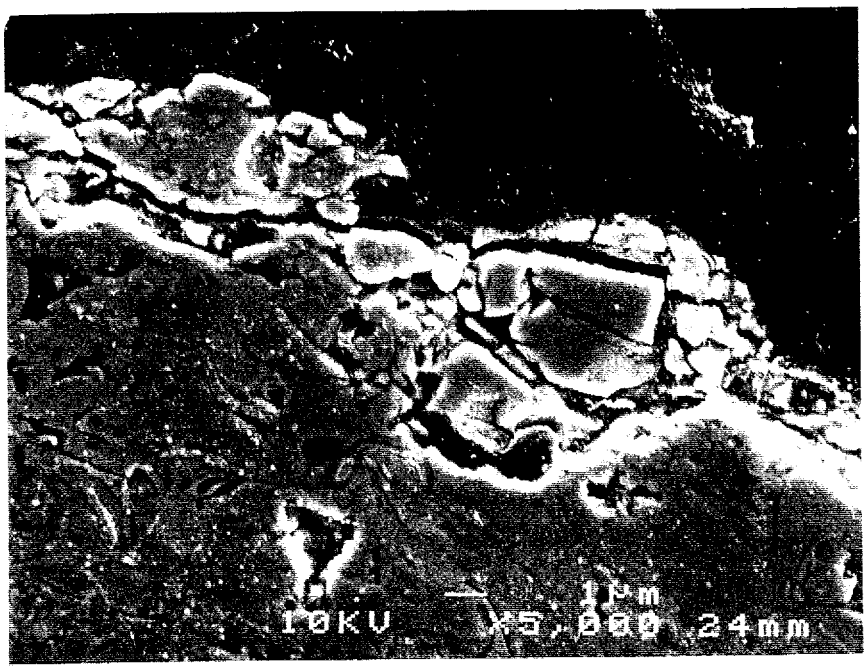

Figure IV.79- Surface cracking in an 80% Cr_3C_2-20% FeCrAlY HVOF coating (90°).

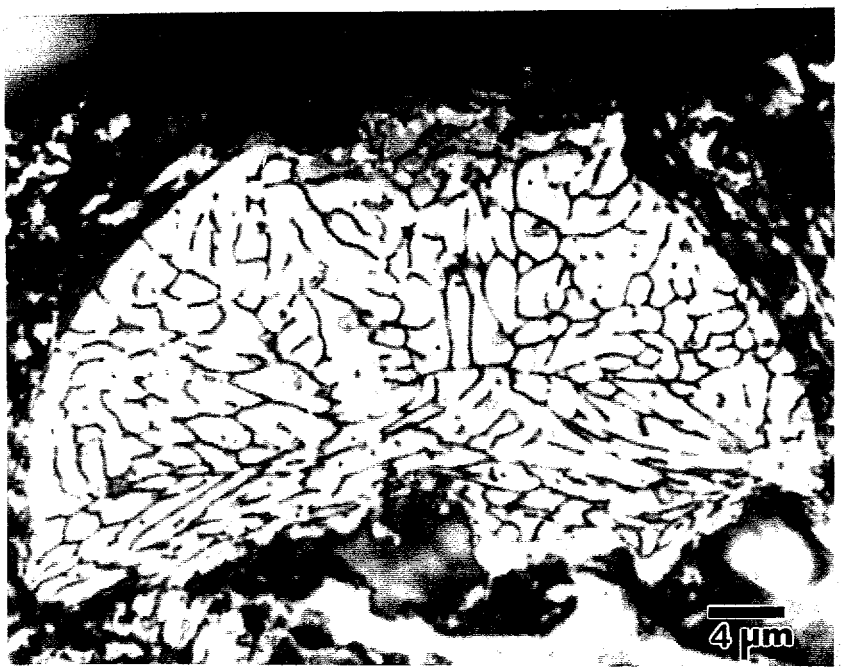

Figure IV.80- Potential dendrite spallation in a 40% Cr_3C_2-60% FeCrAlY HVOF coating (90°).

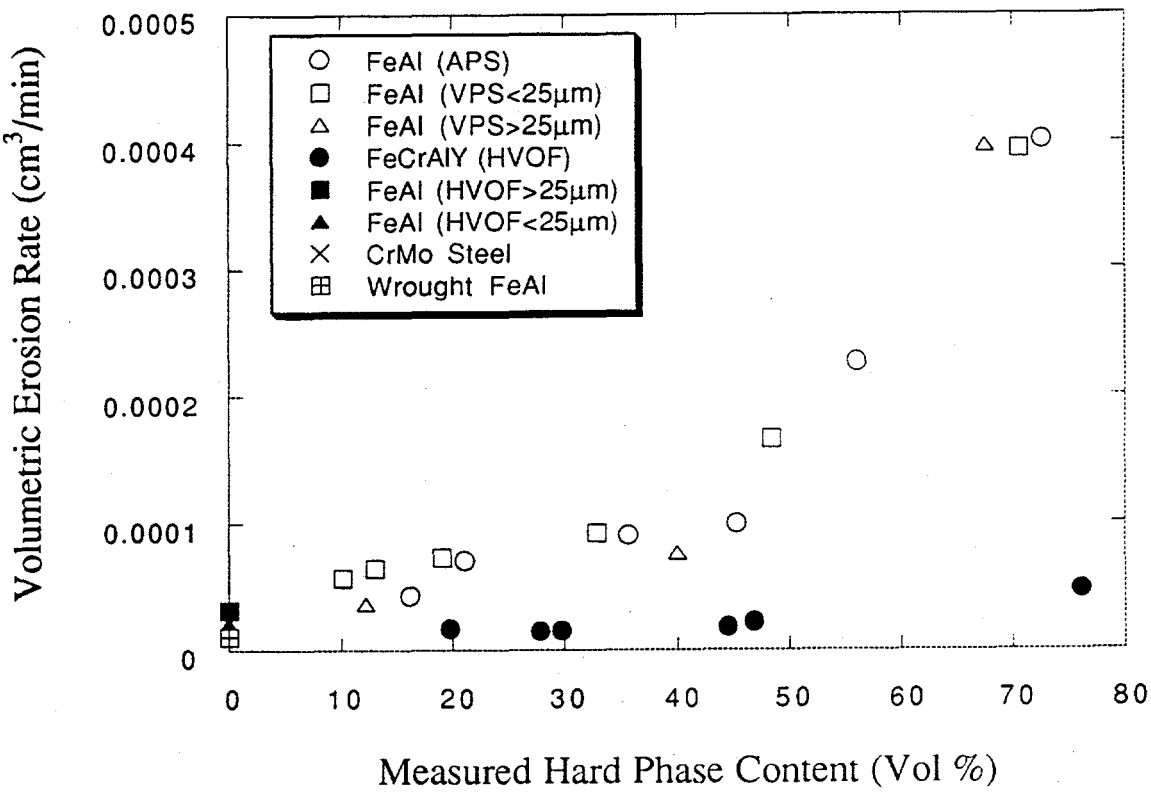

Figure IV.81- Volumetric erosion rate versus measured hard phase content (oxides and carbides) for all of the tested materials (90°).

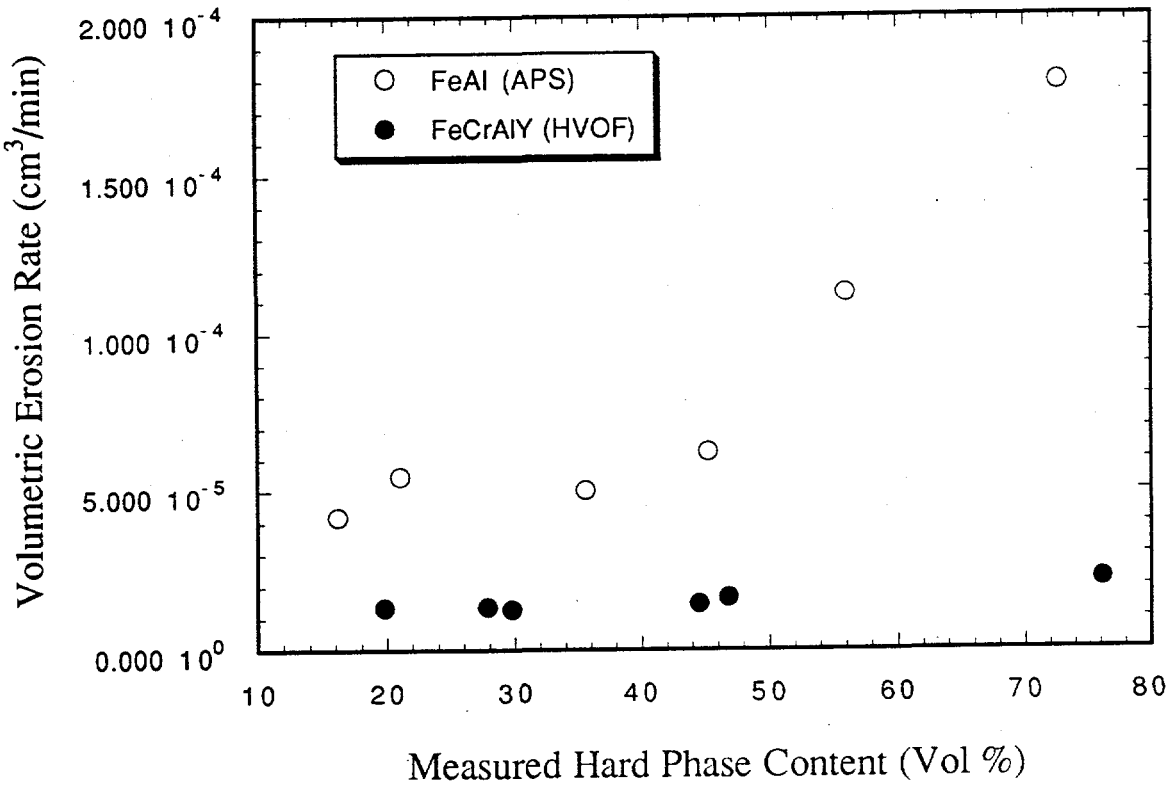

Figure IV.82- Volumetric erosion rate versus measured hard phase content (oxides and carbides) for all of the tested materials (30°).

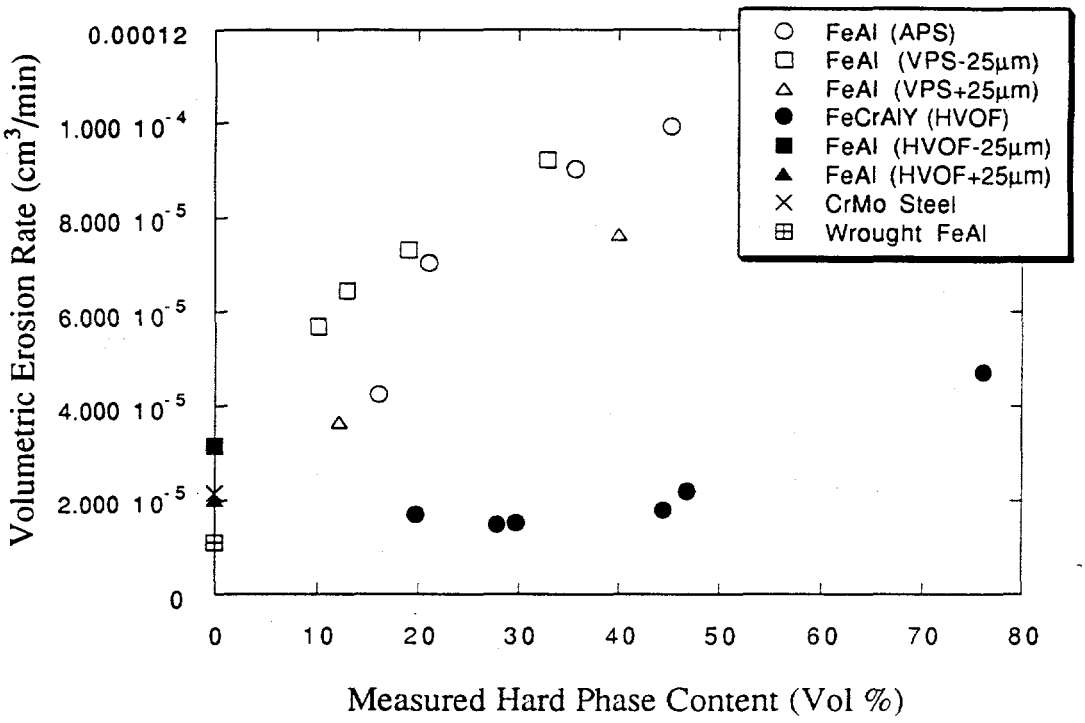

Figure IV.83- Erosion rate versus measured hard phase content (oxides and carbides) for all of the tested materials, focussing on the lower erosion rates from figure IV.81 (90°).